Politechnika Gdańska
Wydział Mechaniczny

Rozprawa doktorska
mgr inż. Karol Centkowski

INVESTIGATION METHOD OF LARGE-VOLUME TIRE WITH MOBILE TEST RIG

Promotor: prof. dr hab. inż. Jerzy Ejsmont, prof. zw. PG

Gdańsk 2015

Acknowledgements

This dissertation was developed during my work as research fellow in Institute of Agricultural Engineering and Renewable Energy at Cologne University of Applied Sciences. I would particularly like to thank to Prof. Dr. –Ing. Alfred Ulrich for motivation, technical and financial support. Our conversations always encouraged me for independent and problem-solving scientific activity and gave me tremendous determination to conduct this research.

I am also very grateful to my doctorate supervisor Prof. Dr. Jerzy Ejsmont from Gdansk University of Technology for his scientific patronage and practical advices through all phases of this research. His edification gave me motivation to accomplish this work.

I want to thank to colleges from Faculty of Facility of Energy, Machinery and Plant Engineering and Institute of Agricultural Engineering and Renewable Energy, especially to Prof. Dr. –Ing. Till Meinel, Arnulf Alexi, Ferdinand Haerst, Thomas Schwan, Friedrich Scholte-Reh, Iris Müser and many others for their openness, understanding, humor and plain support during every day work life.

I am very grateful to all my colleagues from the team of Cologne Lab of Construction Machinery (KLB). Especially grateful I am to Andreas Bogala for sharing with his technical knowledge, for Johannes Grüter for his organizational support and practical attitude and to Holger Winking for his athletic and competition spirit that gave me necessary distance, kept me fit and buoyant.

I want to thank to my family for their patience and enormous support.

Abstract

The goal of this research is to develop the **t**ire **t**est **m**ethod and **m**obile **t**ire **t**est **r**ig. The test rig enables measurement of tire properties as stiffness and viscous damping in vertical direction, and tire–ground characteristics on the asphalt rigid surface. The tire-ground characteristics are measured by force and a torque measurement hub. The design, calibration and the algorithm for calculating the forces in the wheel center are also developed in this work. The mobile tire test rig is based upon the idea of a quarter-vehicle. It is pulled behind the tractor. The whole frame including weights inducing payload, the tested tire and three actuators can freely rotate around lateral pivoting axle.

The vertical stiffness and viscous damping are measured by two methods. The test by free oscillation where the tire rolls over an obstacle and the test of random vibration where the tire is excited by road unevenness are used to measure the tire's properties for large and small excitation amplitudes respectively. The third method surveys tire–ground interactions in lateral direction in a test called step response of lateral force. The test tire is pulled with a certain speed, braked and suddenly turned at a specific angle. The aim of this test is to measure the tire's capability for transmitting suddenly appearing transient lateral forces. During this test the forces are plotted over the wheel slip angle.

The results obtained in this research correspond to findings of other researchers. The three test methods confirmed that it is possible to measure tire parameters and tire-ground characteristics with one mobile tire test rig. The significant achievements of this work are: force measuring hub, excitation ramp instead of beam in test by free oscillation, accuracy definition in the test by random vibration. Further improvements can be done by applying: load cells that can measure forces within three orthogonal directions; a sensor that directly measures the wheel rotation, skid wheel measuring PSD of the test track, a lighter carrying frame and bigger area that would widen the range of tests and enhance accuracy and reproducibility.

This research can contribute in long term to help to: eliminate the gap between TM and TTM; merge various Test Methods into one that can be realized by one TTR delivering inputs for different types of TM; elaborate a standardized tire test rig and benchmarking method.

Keywords: tire, vehicle dynamics, random vibrations, control design, mechatronics, measurement, sensors, statistics.

Zusammenfassung

Das übergeordnete Ziel der Forschung ist die Entwicklung einer Methode zur Reifenuntersuchung und einer mobilen Einzelradmesseinrichtung. Die Messeinrichtung ermöglicht die Untersuchung von Reifeneigenschaften wie ihrer Steifigkeit und viskosen Dämpfung in vertikaler Richtung sowie Reifen/Boden-Charakteristiken auf starrer Fahrbahn. Die Reifen/Boden-Wechselwirkungen werden mittels Messnabe gemessen. Die Konstruktion, Kalibrierung und der Algorithmus zur Berechnung von Kräften und des Moments in Radmittelpunkt sind ebenfalls im Rahmen dieser Arbeit entwickelt worden. Die mobile Einzelradmesseinrichtung basiert auf der Idee eines Viertelfahrzeugs. Sie wird hinter dem Traktor gezogen. Der ganze Rahmen inklusive Gewichten, Testrad und drei Aktoren können um die Querachse frei schwingen.

Die vertikale Steifigkeit und viskose Dämpfung werden mittels zwei Methoden gemessen. Im Ausschwingversuch, in dem der Reifen über ein Hindernis rollt, werden die Reifeneigenschaften bei großer Anregungsamplitude gemessen. Im Test mit stochastischen Schwingungen wird der Reifen durch Fahrbahnunebenheiten angeregt und es werden die Reifeneigenschaften bei geringer Anregungsamplitude gemessen. Die dritte Methode untersucht die Sprungantwort der Reifenseitenkraft. Das Testrad wird mit konstanter Geschwindigkeit gezogen, gebremst und plötzlich in einem bestimmten Winkel eingelenkt. Das Ziel dieses Tests ist die Untersuchung des Reifenseitenkraftaufbaus. Die Seitenkraft wird als Funktion des Schräglaufwinkels ermittelt.

Die in dieser Forschungsarbeit gewonnenen Ergebnisse passen zu Ergebnissen anderer Forscher. Die drei Untersuchungsmethoden bestätigen, dass die Ermittlung der Reifeneigenschaften sowie der Reifen/Boden-Charakteristiken mit nur einer mobilen Reifenmesseinrichtung möglich ist. Die relevanten Leistungen dieser Arbeit sind: die Messnabe, die Verwendung einer Anregungsrampe statt Anregungsbalken im Ausschwingversuch und die Genauigkeitsbestimmung im Test mit stochastischen Schwingungen. In Zukunft können weitere Verbesserungen erzielt werden durch: Implementierung von Messzellen, die in drei orthogonalen Achsen die Kräfte messen können; einen Drehsensor der direkt die Radumdrehung misst; ein Messrad, das die spektrale Leistungsdichte der Fahrbahnunebenheiten messen kann. Ein leichterer Rahmen und eine größere Fahrbahnfläche würden den Messbereich erweitern und die Messgenauigkeit sowie die Wiederholbarkeit erhöhen.

Die Ergebnisse dieser Forschung können in langfristiger Perspektive zu einer Eliminierung der Diskrepanz zwischen Reifenmodellen und Reifentestmethoden beitragen, die Realisierung einer Reifenmesseinrichtung ermöglichen, welche die unterschiedlichen Untersuchungsmethoden für verschiedene Reifenmodelle miteinander verbindet und zur Schaffung von Standardtests und Benchmarkingmethoden beitragen.

Streszczenie

Celem pracy jest opracowanie metody oraz mobilnego urządzenia do badania opon. Urządzenie umożliwia badanie właściwości opon takich jak sztywność i tłumienie w kierunku pionowym oraz charakterystyki odziaływania opony z utwardzonym podłożem. Charakterystyki definiujące oddziaływanie opony z podłożem są wyznaczane za pomocą piasty do mierzenia sił w kole. Konstrukcja, kalibracja oraz algorytm pozwalający na wyliczenie sił w środku koła również zostały opracowane w tej pracy. Myślą przewodnią w rozwoju mobilnego urządzenia do badania opon jest model 'jednej czwartej pojazdu', które to jest ciągnięte za traktorem. Rama nośna wraz z obciążeniem wywołującym nacisk koła na podłoże, trzema siłownikami i badaną oponą mogą swobodnie drgać wokół poprzecznej osi horyzontalnej.

Sztywność oraz tłumienie w kierunku pionowym są wyznaczone za pomocą dwóch metod. Test za pomocą drgań swobodnych polega na tym, że koło przetacza się przez przeszkodę, która wzbudza koło do swobodnych drgań. Ten test służy do identyfikacji właściwości opony dla wymuszeń o dużej amplitudzie. Test poprzez drgania przypadkowe, wywołane poprzez zwyczajne nierówności asfaltu, służy do wyznaczania właściwości opon dla wymuszeń o małej amplitudzie. Trzecia metoda badań opon służy do wyznaczania krzywych sił bocznych w funkcji kąta znoszenia. W tym teście opona badana toczy się z pewną prędkością w ramie nośnej ciągniętej za traktorem, nagle następuje hamowanie i skręcenie koła o pewien kąt. Celem tej metody jest wyznaczenie powstawania sił bocznych w kole w stanach przejściowych.

Wyniki uzyskane w tym badaniu pasują do wyników innych badaczy. Trzy metody badań potwierdzają, że jest możliwe badanie mechanicznych właściwości opon oraz charakterystyk ich oddziaływania z podłożem za pomocą jednego urządzenia. Znaczącymi osiągnięciami tych badań jest budowa piasty mierzącej siły w kole, wprowadzenie rampy wzbudzającej swobodne drgania zamiast belki oraz zastosowanie metody do określenia dokładności parametrów w metodzie drgań przypadkowych. Działanie urządzenia do badania opon mogą zostać ulepszone w przyszłości poprzez zastosowanie czujników zdolnych do mierzenia sił w trzech różnych kierunkach, czujnika mierzącego bezpośrednio kąt położenia koła oraz koła mierzącego gęstość widmową powierzchni testowej. Większa powierzchnia testowa pozwoliłaby zwiększyć zakres badań, dokładność oraz powtarzalność uzyskanych parametrów.

W przyszłości wyniki badań uzyskanych podczas tej pracy mogą przyczynić się do zniwelowania różnicy pomiędzy modelami matematycznymi opon a metodami wyznaczania ich parametrów; ujednolicenia i standaryzacji metod oraz urządzeń do badania opon oraz obiektywizacji pomiarów opon wielkogabarytowych.

Glossary of Symbols

Symbol	Unit	Description
a	$\frac{m}{s^2}$	Acceleration
b	mm	Width of the ring
c	$\frac{N \cdot s}{m}$	Viscous damping coefficient
d	mm	Nominal diameter
e_{Fx}	V	Output voltage
f	Hz	Frequency
f_{max}	Hz	Maximum frequency
f_{samp}	Hz	Sampling frequency
f_0	Hz	Natural frequency
k	$\frac{N}{m}$	Spring constant / stiffness
m	kg	Mass
t	mm	Nominal thickness
v	$\frac{km}{h}$	Velocity
x, y	mm	Load ring axis system
E	GPa	Modulus of elasticity
$G_{xx}(\ )$	$\left(\frac{m}{s^2}\right)^2 / Hz$	Power spectral density for $0 \leq f \leq \infty$
$G_{xy}(\ )$	$\left(\frac{m}{s^2}\right)^2 / Hz$	Cross – power spectral density for $0 \leq f \leq \infty$
$H(\ )$	$-$	Transfer function
L	mm	Half extension
Q	$-$	Quality factor
R	$mm; \ \Omega$	Radius of the ring; resistance
R_m	MPa	Tensile strength
$S_{xx}(\ )$	$\left(\frac{m}{s^2}\right)^2 / Hz$	Power spectral density for $-\infty \leq f \leq \infty$
V_{Exc}	V	Excitation voltage

X, Y, Z	mm	Intermediate axis system
X_C, Y_C, Z_C	mm	Centre axis system
X_E, Y_E, Z_E	mm	Earth – fixed axis system
X_H, Y_H, Z_H	mm	Horizontal axis system
X_V, Y_V, Z_V	mm	Vehicle axis system
X_W, Y_W, Z_W	mm	Wheel axis system
α	°	Wheel slip angle; circular position in the load cell
β	°	Body slip angle
γ	–	Coherence function
δ	$-; °; mm$	Decay rate; steer angle of the test wheel; displacement
ε	–	Strain
$\eta = \Omega / \omega_0$	–	Frequency ratio
θ	$kg \cdot m^2$	Moment of inertia
μ	–	Coefficient of friction
ξ	–	Damping ratio
π	–	3.14159265...
ρ	m	Radius of the bend
σ	MPa	Structural strength
υ	–	Damping ratio
φ	°	Circular position in the load cell
ψ	°	Yaw angle
ω	°	Rotation
ω_0	$\dfrac{rad}{s}$	Circular frequency of undamped oscillator
Δ	mm	Axial extension of the beam
Λ	–	Logarithmic damping decrement
Ω	Hz	Circular frequency of excitation

Glossary of Abbreviations

Abbreviation	Description
CB	Center of Balance
CG	Center of Gravity
CM	Construction Machines
CTC	Centre of Tire Contact
DAQ	Data Acquisition
DOF	Degree of Freedom
DSP	Digital Signal Processing
FSO	Full Scale Output
GF	Gain Factor
LTI	Linear Time Invariant
MTTR	Mobile Tire Test Rig
OEM	Original Equipment Manufactures
PSD	Power Spectral Density
RDL	Reference Datum Line
SF	Safety Factor
SNR	Signal to Noise Ratio
TM	Tire Models
TTM	Tire Test Method
WFTMD	Wheel Force and Torque Measurement Device
BAsT	

Chapter 1

1   Introduction

1.1   Motivation

Manufactures of tractors all over the world make a lot of effort to produce more reliable and productive machines. A few new high horsepower performance categories of tractors have come into being in last two decades. Beside farm industry they are applied in road construction trade, mining, forestry and for urban purposes. The usage pattern of an average tractor has changed significantly in the last twenty years. They claim the term of "multipurpose vehicle". The tractors have obtained new duties. They are used more often for transportation task in wide sense. For that reason, in safety instructions for tractor users there is chapter dedicated to the 'driving' that reminds to the tractors' operators: "...keep your speed down"[1].

Figure 1.1 Riding Tractor with high speed, Cover page of safety instruction "Using tractor safely", Published by Health and Safety Executive from United Kingdom [1]

Under those circumstances the tire reveals as one of the most important element exposed to extremely different requirements. This element provides the contact between ground and the machine during transportation rides. Thus, the agricultural tire is considered as one of the most important element influencing the reliability. The total transportation capacity is defined by amount of material carried per cycle and the total cycle time. The trend of increasing loading capacity and increasing maximal transportation speed lasts for couple of decades. These developments have in fact improved the work cycle.

On the other hand the high maximal speed and high weight causes that vehicle dynamic has to be taken into account in the early stage of design. Obviously it has to be continuously improved. For that reason the suspension systems of chassis, cab and seat have become the state of the art in regular agricultural or construction machines. The European Commission has established in the year 2002 the European Vibration Directive [2]. The technical purpose of these regulations is to limit mechanical vibrations that are harmful for the human body. The social aim of this legislation was to protect millions of workers exposed to mechanical vibrations transmitted to the hands and the whole body. First, the suspension systems in a wide sense cut off the shocks on the machine's body structure [3]. Less mechanical shocks excited by ground, let build more weight light chassis. It causes that more lose material can be carried by the same fuel consumption. Second, the suspension systems let reduce vertical fluctuation of dynamic wheel loads. It causes also significant decrease of tire – ground loads fluctuations in horizontal plane. That means the improvement of vehicle dynamic behaviour. In consequence, better handling, braking and accelerating enables further shortening work cycle. But in many machines as for instance the tractor or wheel loader the suspension relies still on tires. So the field of attention is moved again onto the tires. The tire as an area of uncertainty uncovers weakness of construction machines. On the other hand the new transportation tasks cause that the tractors spend more times in traffic on the asphalt. The potential risk of fatal consequences in case of accident between construction machine and several times lighter passenger car caused that the interactions between tire and the rigid pavement has become very important again.

The tractor is example of both construction and agricultural vehicle that operates on- and off–road. The wide range of application field causes extremely high demands to the tire performance. The tire pressure is varied in according to the operation condition. The mechanical properties changes within the inflate pressure too. In general the subject of interest for this research is the tire of tractor that travels over reasonably long distance at higher speeds on rigid pavement.

The tractor's request to the tire:
- wide spectrum of application (off– and on–road operations);
- optimal traction on the soft ground;
- high soil protection through low pressure in contact area;
- good transport performance (low rolling resistance, good cornering and braking performance);
- long lifetime.

The development of construction machines related to productivity demand has caused that the multi-body simulation tools are commonly used to analyse vehicle dynamic behaviour. There are plenty of mathematical models of the vehicle with a different complexity dedicated to analyse the certain situation. The tire behaviour is still the most bothering issue in the whole model of vehicle. Historically the first tire models were introduced to the passenger cars and after that they were extended for purpose of construction machines (**CM**). More information about tire tests and the mathematical description of tire behaviour called tire models (**TM**) is placed in the second chapter referring the state of the art.

There are several incoherencies referring to the issue of tire that have motivated this research. First of all the models of CM – TM are mainly based either on tests conducted at low velocities and complex loading on real surface [4] or at high velocities under simple loading situation and on artificial surface[1] [5]. Further these tire models are used to simulate complex behaviour that can be described as critical road situations, meaning high velocities, large slips, large wheel slip angles, free oscillations on real rigid pavement. These facts lead to the observation that testing method wanders too far from simulated road situations. In other words, in order to

---

[1] Describes in wide sense the contact body for test tire. In general it varies in surface structure, as in case of steel belt, or shape, as in case of drum test rigs, from the pavement in real world operations.

enhance accuracy of vehicle simulation model the tire testing method and tire model must be further developed, that is coincident with the statement of Mr. Böhler [6].

Secondary, the research centres use different test facilities to gain tire parameters usually applicable only for their description method of tire behaviour. There is lack of parameters of large volume tires and their behaviour on rigid road surface as asphalt [6]. Other research centres or manufactures in this situation must in advance decide which aspect they want to simulate and according to that to build their own test facility to test every tire.

The third fact increasing problem for CM users is that the tire manufactures promote their products by emphasizing specific extraordinary tire performances without revealing any physical parameters and the method of their test. There is no standardized and common test rig non test method of tire enabling objective benchmarking. Under these circumstances the consumers of large–volume tires are left without objective performance rates. Considering that tires with the same dimensions but manufactured by different OEM have measurable different dynamic properties, this incoherence is very meaningful [7].

1.2 The goal and the method of this research

The goal of this research is to develop the **t**ire **t**est **m**ethod (TTM) including tire test rig. The test rig must enable measurement of tire properties as stiffness and viscous damping in vertical direction and tire – ground characteristics in practically relevant operating situations. The fact of measurement of tire – ground interactions implies that the test rig must be mobile in order to incorporate various surfaces of rigid pavements. The tire shall have freedom of oscillation in vertical direction in order to behave as it would in real machine during typical operation. Moreover the tire test rig must enable to expose the tested tire to other loads set by braking moment, steer and camber angle in stationery and transient way. The braking slip and wheel slip angle should reflect as truly as possible real road situations.

The measured parameters should help to rate tire in aspects of handling, riding comfort, traction performance and rolling resistance. The evaluated tire parameters and tire – ground characteristics should provide necessary inputs for different tire

models. In the long time plan this research should help to survey all three incoherencies in tire know–how mentioned in previous section.

The proposed **m**obile **t**ire **t**est **r**ig (MTTR) should enable the tire for free vertical vibrations that will be excited by road unevenness. The payload should be realized by variable weights mounted on the carrying frame. The frame is pulled behind the tractor that provides kinematic energy. The whole frame including weights, tested tire and all actuators shall be able to freely rotate around lateral axle so it provides one additional DOF in reference to the tractor. Because of a relatively big ratio of distance between frame rotation axis and the tire patch to the vertical movement amplitude the vibrations will be analysed as linear. So the vertical vibration model of the tested tire could be represented by single–mass–oscillator with weights as rigid body and tire as spring and damper element. This assumption will be especially useful by evaluation of measurement data. This model is known in vehicle dynamics theory as quarter – vehicle.

Following assumptions have been formulated by author at the beginning of this research. The vertical stiffness and damping will be measured for large and small excitation amplitude separately. It will be conducted respectively in the test by free oscillation where the tire will roll over obstacle and the test of random vibration where the tire will be excited by road unevenness. Those vertical tire parameters will be tested under disturbance in horizontal plane. In longitudinal direction to the tested tire will be applied braking moment. In lateral direction will be induced wheel slip angle. The disturbances will be applied in diverse combination by different speed. The big attention should be paid during result evaluation to elaborate the method to define the accuracy of obtained results. This should enable to define the reproducibility and repeatability that should ensure the reliably comparison of results obtained by these method in different research centers.

The third method will survey tire – ground interactions in lateral direction in test called step response of lateral force. The loaded tire will be pulled with certain speed, braked and suddenly turn on for specific angle. The aim of this test is to measure tire's capability for transmitting transient lateral forces appearing suddenly. In order to measure forces acting on tire, the rim is mounted on self– designed wheel force and torque measurement hub. The force transducers are based

on strain gauges. The mechanical design of load cells and the whole hub including the measurement system, its calibration and signal conditioning belongs to the goal of this research. The algorithm to calculate the forces and moments must be also developed and verified with this device. During this test the forces should be plotted over the wheel slip angle.

1.3 Outline of this thesis

The answer for the question: "why the study was undertaken?" is presented at the beginning of the chapter 1. The general purpose of this research and the method to accomplish it is described in next subsections. The chapter one ends with short outline of this thesis.

The overview about research and current know–how in the field of tire model, tire tests and wheel forces sensor is presented in the chapter 2. The goal of this chapter is to point out different trends at diverse R&D centres.

The chapter 3 is the vastest one. It describes the wheel force and torque measurement device. The chapter alike the whole designing process of wheel force sensor is divided into three sections. The first one refers to *vehicles dynamics* theory where the maximal loads are defined. The second section concerns *structural mechanics*. In this part the geometry and proper dimensions of sensor are calculated and the proper material is chosen. In the third section are undertaken tasks from field of *measurement engineering* as: application of strain gauges, signal processing and calibration.

The chapter 4 describes the requirements and functions of **m**obile **t**ire **t**est **r**ig. The vehicle dynamic analysis of MTTR for vertical and horizontal plane is conducted according to control design methodology and is core of this part. This chapter ends with listing out some technical data of tire test rig.

The chapter 5 describes theory of three methods conducted with the test rig in this research. The first two tests of step response and random vibrations are used for estimation of the vertical tire stiffness and damping. The test of step response of lateral force is used for estimation of tire's capability of transferring steering forces. Here the author presents the setting of measurement device and way of evaluating the measurement data.

In the chapter 6 are discussed results obtained during this research.

The chapter 7 and 8 explains the strong and weak points of the mobile tire test method and sketch possibilities for further research in this area.

After that I will present the bibliography used during elaborating this research and the thesis.

At the end of this thesis are two appendixes. The appendix A contains information relevant regarding the wheel force and torque measurement device. The appendix B contains information significant for evaluation of measurement data.

Chapter 2

2   State of the Art

The overview about research in field of tire model, tire tests and wheel forces sensors is given in this chapter. The term of tire model is explained at the beginning. Further are described the classification, functions and applications of tire models. The elementary types of tire tests including commercial solutions are presented in the next sections. In the third part of this chapter, the current wheel force sensors dedicated to construction machines are presented.

The information presented below should help to set the research question in present technical circumstances and be comprehensive complement for the part about background and research approach.

2.1   Tire models (TM) and tire testing

Short Definition and Classifications

The tire model means mathematical description of real tire's behavior. It is used in multi–body simulation to predict vehicle dynamics. The crucial issue is always right input e.g. tire's parameters that must be obtained for every tire and for particular boundary condition. Generally there are two main types of tire models: the physical and empirical. The physical model refers to the solution where the tire is described by a mechanical substitute model like for instance parallel spring damper (Voigt–Kelvin) element. The tire parameters have usually the real physical units like stiffness, damping ratio. The empirical tire model is also called model of characteristic curve. It describes mechanical dependencies by curves obtained in one specific tire test. Usually the tests curves are described by the family of parameter obtain from regression procedure. These parameters do not have physical units. There are also other rankings of tire model according the directions they refer. According to such a methodology there can be distinguished: the vertical, longitudinal or lateral tire models. Another criterion defining different types of tire

models is the frequency range. In general there are stationary or transient tire models. The very wide spread type of tractor tire model is so called semi–empirical tire model that describes the tire – ground interaction by family of characteristics and the inner mechanic of tire using the purely physical models. Above mentioned mathematical description of tire behavior are used in dynamic simulation therefore they are called real–time tire model.

Another group of tire's behavior descriptions considering the inner structure of tire are the FEM models. There are mainly used during development of new tires and make possible to control structure parameters like, strength, hardness, flexibility, weight or modal deflections. They can be used to obtain parameter for physical or empirical models usually only in stationary states. In the last decade the Discrete – Element – Method (DEM) models became more important. They can model the tire – ground contact area and include the forces and deflections of the soft soil.

Activities at Other Research Centers

At the **Berlin University of Technology** the testing of agricultural (ag) tires has begun in 70s. Sharon and later Kising investigates the ag tires in vertical direction [8–10]. Siefkes investigates the tire dynamic in contact area and its influence on its wear [11]. Pickel in his research compares tire models from Crolla, Pacejka and Siefkes [12]. He focuses in his research on capabilities of tire model within vertical direction. Kaplick compares and verifies tractor simulations model. He measures tires by placing the whole tractor on indoor hydraulic vibration facility. He concerns especially on aspect of roll – off test [13]. Mr. von Holst comperes two mathematical models of tires [14]. The empirical Pacejka tire model [15, 16] with very time consuming parameterizing, that has been developed to the passenger cars tires, is set against more complex Gallrein physical model. The physical model is much easier to parameterize but more time consuming during calculation. Due to the fact that in most tractors the suspension relays still on tires he analyzes only dynamics of the tire in vertical direction which he claims is the most important. He points out that in order to obtain better results and quality of the tire model three aspects must be taken into account: the inner friction of tire, the influence of rough profile and the unroundness of the tire. The parameters for the standard tire model are vertical stiffness and viscous damping ratio obtained in tests in condition similar to that in

application case. The Gallrein model includes the inner friction in substitute model according to nature of elastomer materials and let to define the real form of tire. Because of that it gives much more precise results. Mr. Thomas in his PhD dissertation conducted at Braunschweig University of Technology tests the tire in vertical direction on flat-trac test rig from Berlin University of Technology. He claims that tire of the same dimensions made by different manufacturer have measureable different dynamic properties [7].

The testing of agricultural tires has started at the **Hohenheim University of Technology** in early 80s. Mr. Schrogl has developed indoor flat-track tire test rig that enabled tire testing by different velocities and payloads [17]. He investigates the vertical stiffness and damping. Mr. Langenbeck prepares the test rig for greater payloads and enhances its stiffness [18]. He also adds non-linear range into vertical direction and introduces the longitudinal direction to the tire model. His improvement enhances the calculation accuracy of the riding behavior. He has tested several tractor tires. The new tire parameters obtained mainly in the tests by free oscillation made possible to simulate high speed tractor during transportation rides. Further investigation of agricultural tires in vertical and longitudinal direction has been conducted by Plesser [19]. He analyzes the influence of trade pattern and wheel unroundness on vibration behavior.

Mr. Heine has tested agricultural tires on soft and rigid real surfaces. He investigates stationary and transient behavior of lateral force and self-aligning moment on pulled and turned wheel [20]. In his research Mr. Armbruster has developed single wheel tester [4]. He has equipped the test rig into payload control system. Thanks his development the test wheel can be loaded by braking or driving moment. He investigates the longitudinal and lateral stationary behavior under superimposed wheel slip and slip angle. Barelmeyer improves the single wheel tester so that he can investigate the tires at transient wheel slip angle [21]. He tests longitudinal and lateral tire behavior on soft and rigid ground however only by low speeds. Böhler in his dissertation conducted at the Munich University of Technology uses tire model developed by Plesser. He has obtained the vertical tire parameters on flat track tire test rig from Hohenheim University of Technology. The parameters for longitudinal direction fit to those that he found in literature. He claims that there is lack of

parameters regarding longitudinal tractor tire behavior on asphalt. He points out that in order to enhance precision of tractors' vehicle dynamic simulations the tire model must be further developed [6]. Schlotter has tested the influence of payload fluctuation on horizontal forces [22]. He realizes the payload fluctuation by force excitation and crossing simple obstacles. Brinkmann analyzes the translation of center of tire contact (CTC) for driven wheels [23]. He starts to link tire model to the MBS-model of a tractor [24]. Mr. Ferhadbegović based on prior investigation on agricultural tire, develops the transient, three dimensional model for agricultural tires and conducts several simulations and validations of driving maneuver with tractor [5, 25–30].
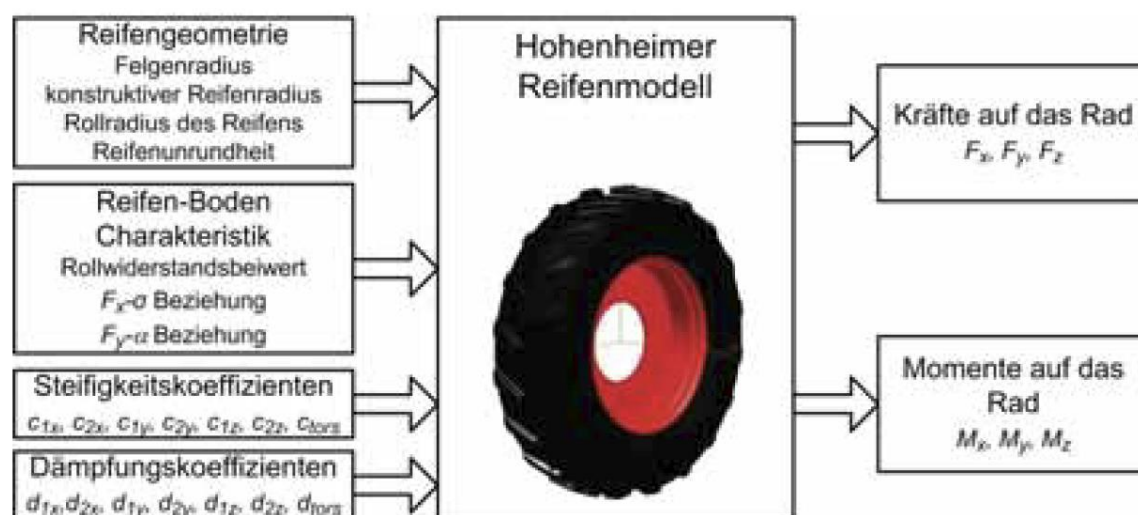

Figure 2.1 Parameters and outputs of Hohenheim Tire Model

At **Darmstadt University of Technology** Betzler elaborates objective method for description of vehicle dynamic of high speed unsuspended vehicle [31]. He uses for his 3D stationary and transient vehicle model the nonlinear, curve characteristic (semi – empirical) tire model. The vertical tire parameters he gains by using an out – door test facility. He measures vertical wheel loads by mounted in the test track surface wheel load device after driving through obstacle. Wermann continues this research. He focuses mainly on lateral dynamic of vehicle and tire [32]. He uses a mobile tire test rig for parameter estimation on rigid surface. The construction of the test rig has not enables free oscillation in vertical direction. He uses this rig for estimation of tire – ground characteristics in horizontal plane.

Crolla in his research conducted in 1989 at the **University of Leeds** improves tractor tire model in such a way that for description of generating forces in the

vertical direction uses linear spring and damper element jointed parallel whereas for longitudinal and lateral direction the same spring and damper element brings together in series. The improvement leads to better predictions of r.m.s. value of acceleration signal in all three orthogonal directions.

Keen form Harper Adams University measures ag tires within mobile quarter-vehicle test rig. He conducts the tests on sine-shaped soil surface. He tests the influence of traction on vertical stiffness and damping. Because of the path shape the excitation frequency is constrained to the velocity.

2.2   Tire tests facilities

In regard to test facilities there are three different methods of tire tests. Probably the most famous are indoor facilities. Second type of tire testing employs mobile tire test rigs. They enable testing on the real surfaces and in condition similar to that in the real application case. All tests conducted with the vehicles belong to the third method of tire testing.
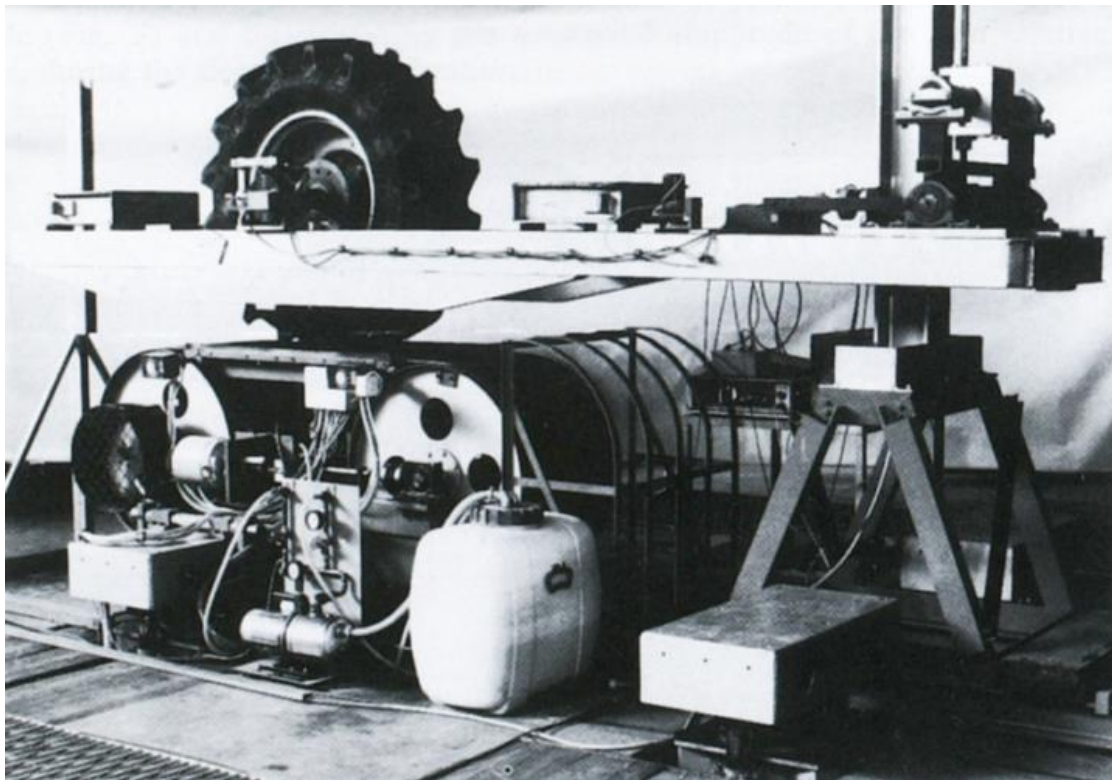

Figure 2.2 The flat tire test rigs at Berlin University of Technology [10]

2.2.1 Indoor tire test facilities

The flat trac tire test rig is one of the most popular indoor facilities. This type of test rigs are manufactured and used at universities [10, 33], research centers at tire manufactures [34] and commercial manufactures delivering such test rigs as one of its product [35]. The steel belt is stretched by two drums and it simulates road surface. The biggest advantage of this test rig is relatively small dimensions, plane contact area, high reproduceability and possibility of free vibrations. The biggest disadvantage is limited capabilities for application of lateral forces and unrealistic road surface. However there are solutions that enables application of lateral forces too [34, 35].

Figure 2.3 The flat belt test stand at Hohenheim University of Technology [22]

The tire test facility from Berlin University of Technology shown in the **Figure 2.2** and the one from Hohenheim University of Technology shown in the **Figure 2.3** were used for test by free oscillations and by random vibrations. In Berlin the test rig was mounted on hydrostatic suspension so that the excitation was induced to the runway. This test facility were used among other by Siefkes [11], Pickel [12], Kaplick [13], von Holst [14], Thomas [7]. The flat belt test stand at Hohenheim University of Technology was introduced by Langenbeck [18]. Later it was rebuild and prepared

to test agricultural large-volume tires with rim size up to *38* inches. At the beginning it was dedicated to investigate the vertical tire stiffness and damping by drop test. Plesser has proofed with this test stand that vertical tire characteristic is strong nonlinear. He determined parameters of vertical stiffness and damping coefficient by measurement maximal tire deflection, deflection speed and shape of the vertical force curve. Later it was improved by Schlotter who added on the top of frame the force exciter [22].

The commercial flat trac test rigs are designed in such a way that payload force is applied by an actuator, as presented in the **Figure 2.4**. They are dedicated to tires for passenger cars, trucks and motorsport applications. Their construction enables wide range of steady-state and dynamic tests. They are suitable to conduct tests for high velocities up to *320 [km/h],* different operating conditions. They are used for test regarding to cornering, traction and rolling resistance. [35].

Figure 2.4 The flat trac tire test rig at Calspan's Tire Research Facility [34]

There are also flat trac rolling roadway facilities where the whole vehicle is mounted on the test rigs. These kind of testing facilities are used for dynamic road handling, ride and comfort and for aerodynamic motorsport testing [35].

Another example of wide spread indoor tire test facility is drum test rig. This kind of tire test rigs are used also by universities, research centers and tire and vehicle manufactures. The biggest advantage is easily application of lateral forces and possibility of inducing discrete obstacles by mounting clutches [36]. To the significant disadvantage belongs falsified contact area. In order to minimize that problem the drum must have big diameter that guarantee big ratio of diameter the wheel and the drum. Von Holst points out that for tractor rear tires the diameter of drum should be greater than *12* meters [14]. Majority of drum test rigs uses the outer runway of drum to lay tire on it [35, 37, 38]. Those drum test rigs are mainly used to conduct rolling resistance and tire/road noise test.
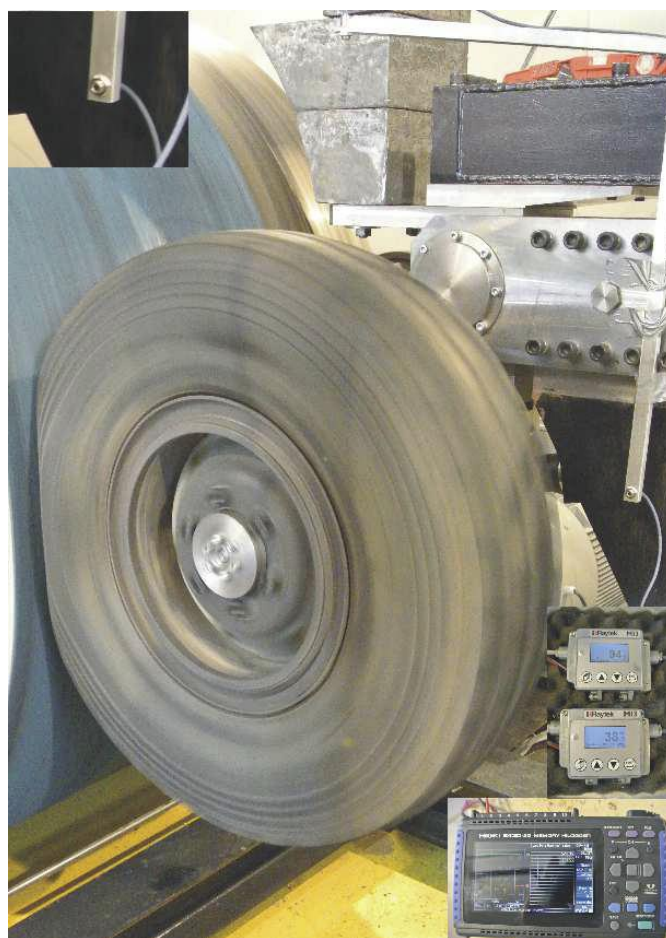

Figure 2.5 Test tire on the roadwheel facility [39]

German Federal Highway Research Institute (BASt) conducts the noise emission and rolling resistance tests on test drum facility where the measured tire is pushed to the inner side of the drum [40]. At the Gdańsk University of Technology there are a roadwheel facilities that are dedicated to conduct rolling resistance test and tire road/noise on drums covered with replica road surfaces. One of the facilities (shown in the **Figure 2.5)** may be used to test truck and military tires.

Probably the simplest tire test rig is that used by von Holst for measuring uniformity and run out of tire [14]. The wheel is mounted in a frame and is driven with constant rotation speed. The test tire does not have contact with any surface. There are measured two signals: wheel angle position and laser distance sensor.

2.2.2   Mobile tire test rigs

The single wheel tester presented in the **Figure 2.6** has been developed and improved by few researchers at the Hohenheim University of Technology [4, 20,22, 24, 33].

Figure 2.6 Hohenheim Single Wheel Tester [33]

The whole measuring machine consists of four wheel trailer and tractor. In the trailer is mounted the test wheel that goes over the real surface in the middle of track width. The test wheel is mounted into the trailer by pivoting suspension that can be lifted up for transport rides and dropped down for measuring operation. The payload force is induced by hydraulic actuator. The vertical tire load can be set for maximum *5.5 tons* and kept constant or varied by control system first developed by Armbruster [4]. The drive or braking moment is applied to the test wheel by

hydraulic gearbox. The test trailer is pulled or braked by tractor. During measuring operation the front wheels of trailer are lifted up and the trailer is blocked so between the tractor and trailer there is no articulation around vertical axis. The steer angle can be applied to the test wheel, front wheels of the tractor and the rear wheels of the trailer. The front and rear axle are steered in such a way to counteract the lateral force generated by test wheel.

The forces acting on the test wheel are measured by six-components piezoelectric sensors. The driving velocity is calculated from the rotational velocity obtained from incremental encoder mounted on the sliding wheel. The rotation velocity of test wheel is measured by incremental encoder. It is multiplied by current tire radius measured by ultrasonic distance sensor and compared with travel velocity in order to calculate wheel slip. The significant disadvantage of this mobile tire test rig is low travel velocity and lack of ability of free oscillation of test wheel. The big advantage is that the mobile test rig can impose the test wheel for transient loads and inputs as traction or braking moment or steering angle [22, 33]. The fact that steer angle can change in the range form *0°* up to *18°* does not injure as long as the camber angle is set for *0* degrees.

Another mobile tire test rig that has been developed at Darmstadt University of Technology and also been used for many tests of agricultural or large-volume tires is test machine called "Berta" [41, 42], see the **Figure 2.7**.

Figure 2.7 Mobile test rig "Berta" [42]

This machine is able to test tires with great loads and braking moments under high velocities on real rigid surface. Because of the absence of ability for free oscillation the vertical parameters especially damping coefficient cannot be determined as it is elaborated by the Hohenheim University of Technology. It is mainly used to determine the tire – ground characteristic in horizontal plane as it did Wermann [32].

Keen form Harper Adams University has measured large-volume tires within mobile quarter-vehicle test rig on sine-shaped soil surface. He tests the influence of traction on vertical stiffness and damping. Because of the path shape the excitation frequency is constrained to the velocity. Additionally the tire cannot be braked or steered. But ability for free oscillation on the real ground is crucial in this research.

Figure 2.8 Tire test trailer at Gerotek [43]

Other related mobile tire test rig is the single axle, unsuspended trailer at Gerotek vehicle testing facilities outside Pretoria in South Africa, shown in the **Figure 2.8.**

The whole trailer can be considered as the rigid body. The lateral slip angle of each wheel hub can be set from minus *-2* degrees to about *12* degrees, in approximate steps of *2* degrees. The high of the hitch can be adjusted in the fixed steps, so the trailer is kept as level as possible for varying tire dimensions. The trailer is equipped in load cells that measure three orthogonal forces acting on one wheel. The trailer is designed to be towed by heavy vehicle. The truck width is greater as the one from towing vehicle so different surfaces as Belgian paving, single obstacles, random uneven track can be tested while the towing vehicle drive on level and plane surface without unnecessary hitch excitations. The relative big disadvantage is the disability for transient adjusting the wheel slip angle and what is evens more distressing the vertical bouncing by slip angle. The vertical force fluctuation have a relatively large influence of lateral forces which may impair lateral force measurements [43].

The author concludes after analysis of the state of the art of test facilities that the mobile tire test shall enable tire test on real rigid surfaces, let imply external loads as wheel slip angles, driving or braking moment under closely vibratory condition as it is in real unsuspended vehicle. In other words it shall be compound of the above mentioned mobile and indoor test rigs.

2.2.3   Tire test on vehicles

The tire tests are quite often conducted by using vehicles. The method of determination of tractor tire's vertical stiffness and damping ratio has been introduced by Ulrich [44]. The total mass of the tractor is distributed in this method in such a way that coupling mass (m_K) which determine the interaction between the front and rear axle payload, equals

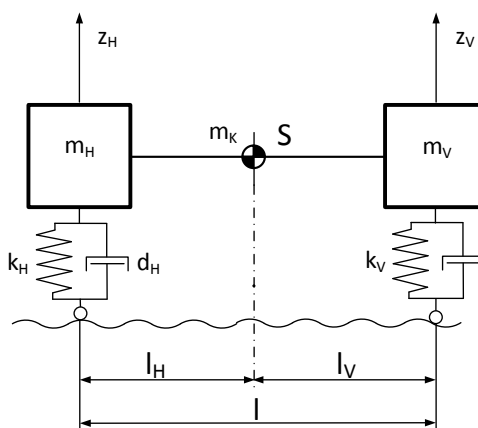**Figure 2.9** Vertical vibration model with discrete mass distribution [44]

around zero, see the **Figure 2.9**. The acceleration signal obtained from transducers mounted under front and rear axle is converted into frequency domain. The resonance peak of each axle is considered as an ideal band pass filter which is compared to the one-mass-oscillator. The half-band-width and natural frequency of

each axle response are used to calculate the vertical tire stiffness and damping ratio for different tire inflate pressure.

There are other investigations procedures that incorporate vehicle to determine tire-ground characteristics [45–47]. They base usually on single-line model of the vehicle. However this attempt is loaded with big practical disadvantage that for this test the real vehicle is necessary. It is simply impossible to have one vehicle to test many different tire models and tire dimensions. Other disadvantage of this method refer to the accuracy of the test and rely on difficulty and high-risk by investigation of tire with in non-linear range. Because of influence of vehicle subsystems as suspension or other sources of vibration as engine the repeatability and accuracy seems to be not reasonable.

2.3   Measurement of wheel forces

There are three global manufactures on the market that offer wheel force sensors for heavy truck applications [48–50]. The common feature for these three OEMs solutions is that the original rim must be rebuild for mounting the wheel force sensors.
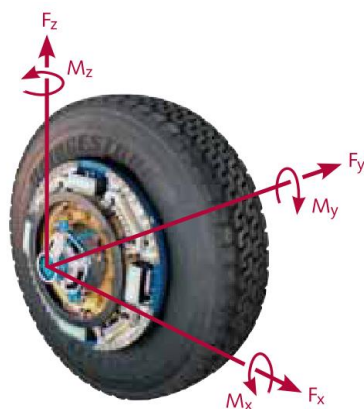
Measuring range		
Fx	kN	±180
Fy	kN	±100
Fz	kN	±180
Mx	$kN \cdot m$	±15
My	$kN \cdot m$	±50
Mz	$kN \cdot m$	±25
Crosstalk	%	≤ 1
Linearity	% FSO	≤ 1
Hysteresis	% FSO	≤ 1

Figure 2.10 RoaDyn S6HT 6-components measuring wheel [48,51]

This incompatibility can be solved by preparing several rims for one wheel sensor but it would be very expensive. Therefore that crosses out one of the most important goal of this research and requirement of test method and test rig that says that one device or test rig should be able to measure different tire dimensions. Kistler's 6-components measuring wheel, RoaDyn S6HT that is shown in the **Figure 2.10** is dedicated for heavy and special vehicles. According to the technical data sheet, it guarantees the best parameters of crosstalk, linearity and hysteresis.

The boundary conditions in this research let the maximal vertical loads to achieve around *75 [kN]*. The maximal vertical load multiplied by awkward friction coefficient around *0.9* permits the horizontal loads up to *67 [kN]*. Taking into account that the dynamic radius of rear tractor wheel equals roughly *0.9 [m]*, the moments around three orthogonal axes requires around *60 [kN·m]*. Those requirements cannot be full field by any commercial solution at this time.

However the most serious barrier of commercial solution is the very high price of the product. The technical and financial motive causes that the wheel force and torque measurement device has been designed in this research.

Chapter 3

3 Wheel forces and torque measurement device

This chapter describes wheel force and torque measurement device designed by the author. The devise is designated in the text with its acronym **WFTMD**. This device is necessary to measure tire-ground characteristics.

3.1   Introduction

The very main reason why the measuring device was designed in the Institute for Agricultural Machinery and Renewable Energy was the high price of commercial solutions. From the vehicle's dynamics point of view the main task of WFTMD is to measure all transient forces and torques that act on the wheel during operations, as:

- braking;
- cornering;
- pulling (traction & rolling resistance);
- damping of vibrations.

The whole designing process of wheel force sensor was divided into three stages. The first one refers to *vehicles dynamics theory* where the maximal loads were defined. The second stage concerns about *structural mechanics.* During this stage the geometry and proper dimensions of sensor were calculated and the proper material was chosen. In the third stage the tasks from field of *measurement engineering* as: application of strain gauges, signal processing and calibration were undertaken. The most important requirement stated that the measuring device must be mountable on the original tractor's front hub. It had to be also possible to screw different sizes of rim on without necessity of rebuilding, cutting or manufacturing.

3.2 Vehicle dynamics theory

3.2.1 Coordinate system

This section presents axis and coordinate systems that is used for description of vehicle and wheel dynamics. This nomenclature is applied in the whole thesis. The four following right-handed axis systems including their notation convention are used to define vehicle's position:

- **E**arth-fixed axis system (X_E, Y_E, Z_E);
- Intermediate axis system (X, Y, Z);
- **V**ehicle axis system (X_V, Y_V, Z_V);
- **T**est **r**ig axis system (X_{TR}, Y_{TR}, Z_{TR}).

The definitions are based on two norms SAE J670e and ISO 8855. Aside from test rig axis system, they are comprehensively described by Sayers [52] in order to create a common language for describing vehicle dynamics models.

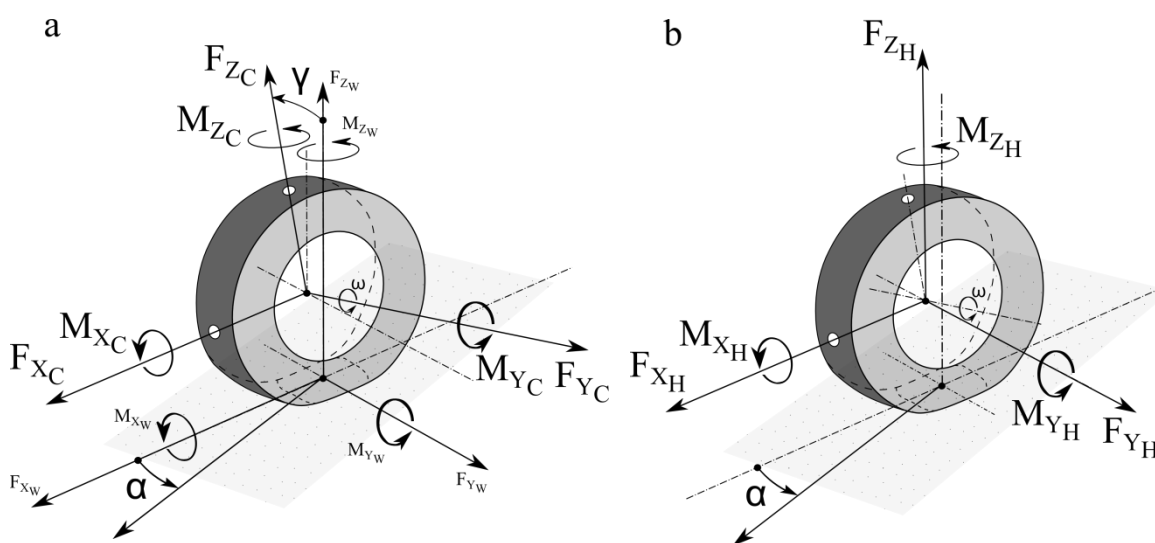
Figure 3.1 Axis system referring to the wheel; **a** – centre and wheel axis system; **b** – horizontal axis system [53]

The **Figure 3.1 a, b** illustrates three right-handed axis systems including their notation convention treating the wheel's position:

- **Centre** axis system (X_C, Y_C, Z_C);
- **W**heel axis system (X_W, Y_W, Z_W);
- **H**orizontal axis system (X_H, Y_H, Z_H).

The definitions are based on following standards: ISO 3911, ISO 8855, DIN 70000, and SAE J2047. This convention is known under Tire Data Exchange Format (TYDEX-Format) [53] which has been developed by international work group consisting of automotive companies and institutes in order to simplify the exchange of tire data.

3.2.2 Defining loads in the center of the wheel

This section relates to *vehicle dynamic theory*. The three forces $(F_{X_W}, F_{Y_W}, F_{Z_W})$ and three torques $(M_{X_W}, M_{Y_W}, M_{Z_W})$ in the **c**enter of **t**ire **c**ontact (CTC) are generated from payload, slip angle and drive or brake torque. They cause three forces $(F_{X_C}, F_{Y_C}, F_{Z_C})$ and three torques $(M_{X_C}, M_{Y_C}, M_{Z_C})$ in the center of the wheel. The force F_{X_W} causes the force F_{X_C} and the moment M_{Y_C} because of acting on the dynamic radius r_D. The force F_{Y_W} causes the force F_{Y_C} and the moment M_{X_C} because of acting on the dynamic radius. The force F_{Z_W} is the normal force to the ground with its origin in the CTC. It causes F_{Z_C} and has significant influence on the M_{Z_C} and the rolling resistance. In general the moment M_{Z_C} depends from many other factors like area of the patch, kind of surface, environmental conditions like temperature and humidity, thread shapes and tire's material prosperities. The relation between longitudinal F_{X_W} and lateral force F_{Y_W} is calculated with respect of maximal vertical force in the patch, F_{Z_W}, according to "kammsche circle" theory. The maximal vertical loads on the single tire were defined on the basis of a maximal permissible payload of any tire that can be used with tractor John Deere 6920S. The maximal payload equals *6190 [kg]* for the rear wheel with the tire XM 108 650/65 R32, OEM: Michelin, by the inflated pressure *1.7 [bars]* and was treated as the reference value. The maximal static payload was limited to *5000 [kg]*. However the whole vertical force contains static and dynamic part. The ratio of the dynamic vertical force to the vertical static force is called wheel load impact factor. According to Ulrich [44] by the level of *0.33* the wheels loses contact with the ground. The bouncing of the wheel may be excited by road unevenness. Therefore it was assumed with great confidence that the impact factor will not exceed *0.5*.

$$\frac{F_{Z_{W,dyn}}}{F_{Z_{W,stat}}} \leq 0.5 \qquad\qquad [3.1]$$

So the whole wheel normal force equals $F_{Z_W} = 73.5 \, [kN]$. Knowing the maximal vertical force, the principle of "kammsche circle" and the maximal static radius $R_{stat} = 0.9 \, [m]$, the loads in the center of the wheel was easily estimated. However there three situations which have to be taken into account during structural analysis were observed.

First case: the wheel slip angle equals zero, the longitudinal force is maximal (the wheel is driven or braked under maximal vertical load); the lateral force equals zero.

Second case: the wheel slip angle equals *45 [°]*, the longitudinal and lateral force are equal and maximal. The wheel is driven or braked under maximal vertical load.

Third case: the slip angle equals *90 [°]*, the longitudinal force equals zero, the lateral force has maximal value.

Table 3.1 Loads in the center of the wheel

Component	Symbols	Units	1st case	2nd case	3rd case
Longitudinal force	F_{XC}	N	66220	46825	0
Lateral force	F_{YC}	N	0	46825	66220
Vertical force	F_{ZC}	N	73575	73575	73575
Torque about long. axis	M_{XC}	Nm	0	42145	59600
Traction torque	M_{YC}	Nm	59600	42145	0
Self-aligning torque	M_{ZC}	Nm	0	4214	5960

The third case can happen when lateral translation is much quicker than the longitudinal or the slip angle equals *90* degrees. A situation like that might occur during the drift. When the vehicle is yawn about the vertical Z_V axis.

The coefficient of friction in every case equals $\mu = 1.0$. That is the most dangerous value for calculation of maximal loads. The self-aligning torque is caused by the wheel lateral force, F_{Y_W}, the longitudinal force, F_{X_W}, and due to the steering geometry and payload. Its magnitude was assumed as *10%* of vertical force time *1 [m]* long arm. Magnitudes of loads in the center of the wheel for each one, out

of three, different driving situations are presented in the **Table 3.1**. The maximal values of each component cannot occur at the same time.

3.2.3 The concept of measuring hub

The concept of the measuring hub was created after analysis of hub's design of Ulrich that is presented in the **Figure 3.2**, and Just [54].
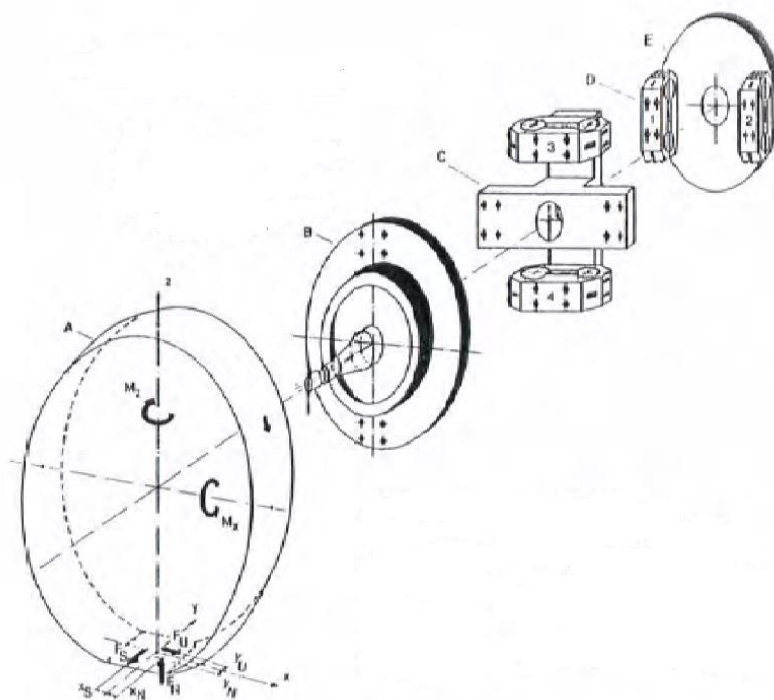
Figure 3.2 The 5-components measuring hub developed by Ulrich [44]

As soon as the loads in the center of the wheel were defined, the concept of WFTMD had to be discussed before the structural analysis began. The crucial sensing elements of measuring hub are six extended load rings that are mounted between two carrying plates. The load cells will be detailed presented in the section 3.3.1. The inner carrying plate is mounted to an offset ring which surrounds the planet gear. Those parts all together create the WFTMD. It was predicted to mount this device to the original tractor's hub. The outer plate has two different bolt circles with female thread ready for mounting a *32* and *38* inches rim size that are respectively front and rear standard tractor's rim. The solution of WFTMD in general, its geometry and also mounting way has significant influence on the loads in the single load cell. As the **Figure 3.3** shows the measuring hub rotates with the wheel. With this solution it is able to measure six components of wheel load, three forces $\left(F_{X_C}, F_{Y_C}, F_{Z_C}\right)$ and

three torque $\left(M_{X_C}, M_{Y_C}, M_{Z_C}\right)$. The design is very rigid, simple and reliable from mechanical point of view. On the other hand the signals flow and acquisition method needs more advanced and sophisticated solutions. Nowadays the costs and effort to transfer the signals from rotating devices to a fixed coordinate system is relatively low. The final solution is presented by the end of this chapter.
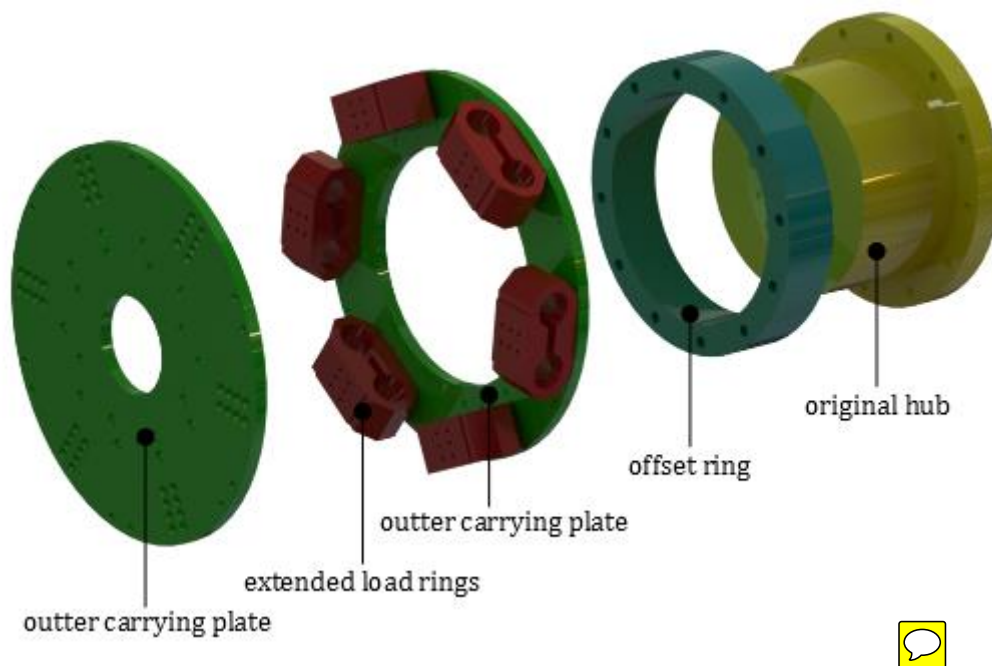
Figure 3.3 The concept of measuring hub

3.3 Structural mechanics

Introduction

The force transducers use technology of strain gauge (SG). The strain gauges are glued on the element in very specific location and orientation. Shape of load cell changes lightly under influence of external forces. So the surface under strain gauge is slightly stretched or compressed. This positive or negative elongation leads to change of strain gauge resistance. There are plenty of generally accepted geometries of load cells. The theory describing stress distribution in the fatigue body is well known from many books on the theory of elasticity. The topic of strength analysis of specific load cell was covered in many journal papers in 70s. Mr. Hoag and Mr. Yoerger describe mathematical development of single and extended ring for specific loads [55, 56]. They discuss the Castigliano's theory which they use to calculate: vertical and horizontal displacement, rotations, bending moments, shears and axial forces. They present as well equations for those calculations. In the paper [55] from

1974 they describe the way of connecting strain gauges into conventional Wheatstone bridge circuit to assign vertical and horizontal force and one torque too. They also mention the restrains which have to be kept during design of extended load ring. Mr. Rüdiger Just widely describes in his work diploma [54] in 1980 the process of designing six-component measuring hub with extended load rings as sensing elements for rear driven tractor's axis. However, an approach of determining the dynamic loads in the center of wheel and an algorithm for signal flow has been significant simplified during this research.

Current calculating power of computers and CAE software caused that the strength and pure structural analysis of transducer's fatigue body of this shape is not an aim of engineering research anymore and so will not be covered in this chapter. The actual focus is on improvement of dynamic properties, range of operating temperature, accuracy and convenience in data analysis.

Having defined the loads and the general concept of the WFTMD the structural analysis was conducted. It was divided into two different analytical methods:

Strain Energy Method	Finite Element Analysis
There was created a mathematical model based on physical principles, such as: Newton's law, linear elasticity (Hook's low), Castigliano's energy method.	In this method analysis bases on the three dimensional geometry. The biggest convenience is that all loads acting in the centre of the measuring hub can be applied at once to all six load rings.
Advantages:	Advantages:
• better to understand the influence of dimensions; • once created mathematical model is easier to carry out any changes; • shorter calculation time; • obtained results respond to the whole revolution.	• very convenient way to carry out quick analysis for one wheel's position; • possible to consider and analyze influence of fixed surface; • clear results shown in very realistic way; • powerful tool to optimize form (if necessary); • all stresses are taken into account (e.g. pure tension and compression, pure torsion, direct
Disadvantages:	
• mathematical model is very time consuming, • some of stresses are neglected	

(e.g.: pure shear and torsion).	shear, strain energy in bending); • easy to obtain other significant results, for instance reacting force – helpful for calculating bolts. Disadvantages: • very sensible for amount of number of elements and quality of meshing, • finally, time consuming to carry out analysis for the whole revolution.

The whole design analysis of load ring and WFTMD was iterative and highly comprehensive process. Therefore one procedure was created in order to structure all calculations. The pattern was taken from control design theory. The graphical interpretation of this approach is presented in the **Figure 3.4.**

Input	**System**	**Output**
loads $\longrightarrow$ geometry parameters $\longrightarrow$ material properties $\longrightarrow$	**Structural Process**	structural strength σ $\longrightarrow$ the sensitivity $\left(\frac{F_x}{\varepsilon x}, \frac{F_y}{\varepsilon y}, \frac{M_0}{\varepsilon(\omega)}\right)$ $\longrightarrow$ deflections $(\delta x, \delta y)$ $\longrightarrow$ rotations (ω) $\longrightarrow$
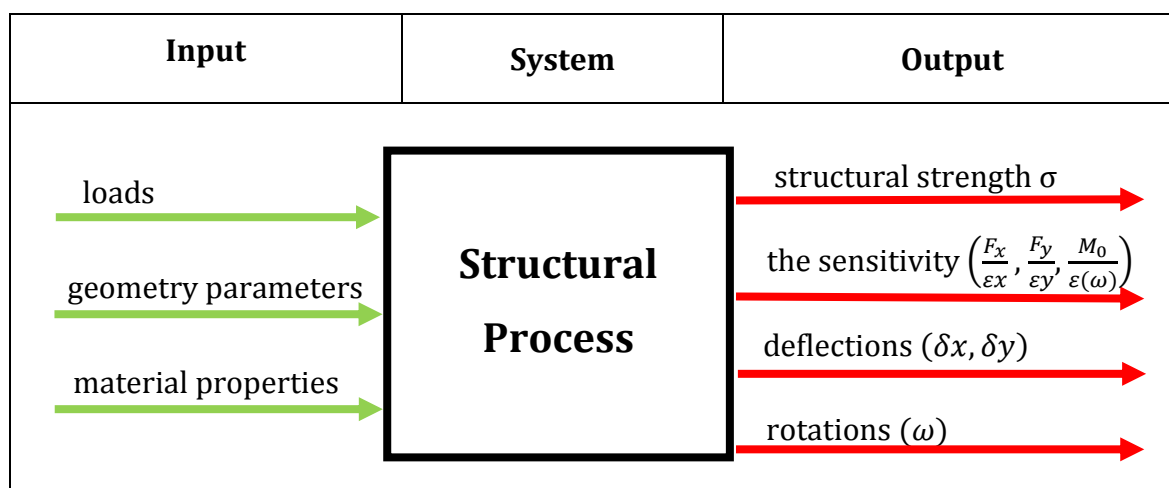
Figure 3.4 Design process of load ring

The whole designing process was divided into three stages: **input** that is group of parameters that fully define the load ring or WFTMD; **system** e.g. equations describing strength and structural phenomes by strain energy method or by finite element analysis; **outputs** e.g. all interpretable results with specific physical sense that enable to decide whether the design is appropriate or not. The analysis according to strain energy theory was conducted in Maple. The FE analysis was conducted in Solid Works Simulation environment. Both methods completed and validated each other.
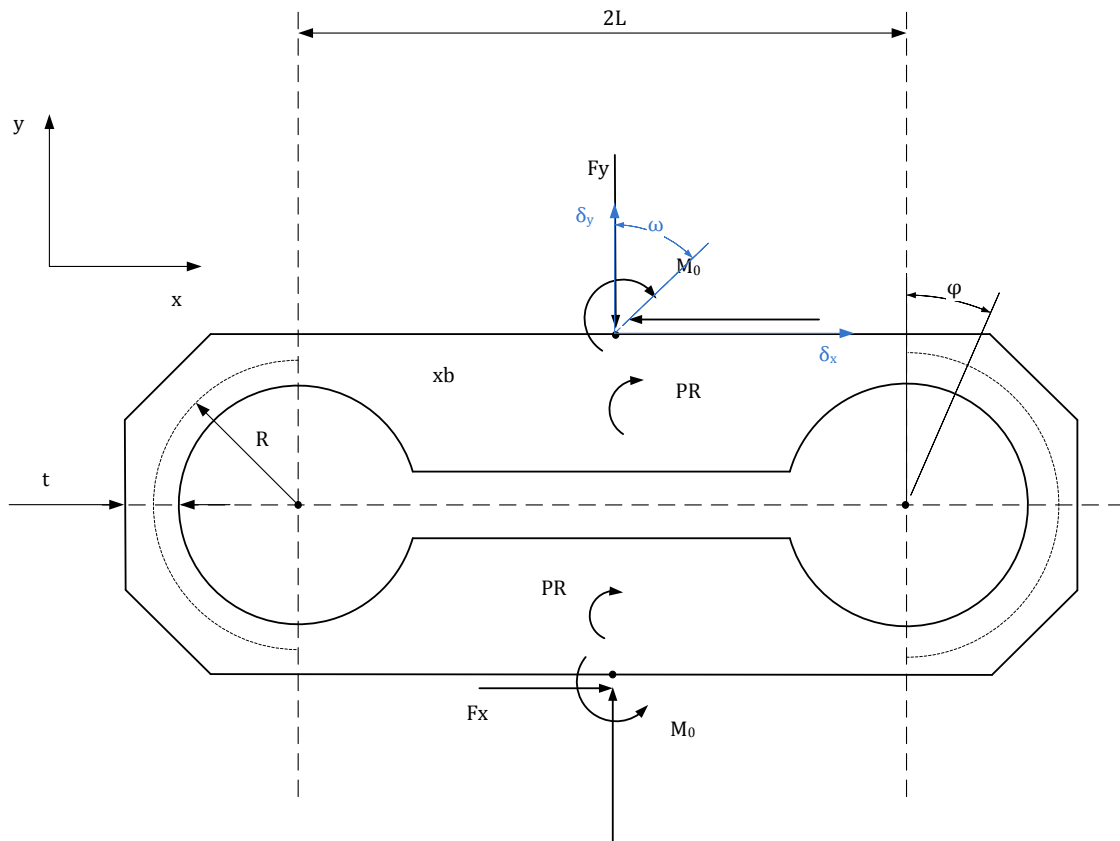
Figure 3.5 Single extended load ring

3.3.1 Model of single load ring

The single load ring is a fatigue body as shown in **Figure 3.5**. Unlike as the axis in the all coordinate systems mentioned in the section 3.2.1 the axis of six load rings are marked with the small letters *x* and *y*. Loaded by vertical F_y and horizontal F_x force and the moment M_0 goes under strains mainly in circular ring portions. By applying the strain gages measuring the deflections (elongations) it is possible to measure separate all acting components and turning the load cell into a force transducer. That means that one load ring contain two force sensors with perpendicular axis of direction. Comparison of results obtained by finite element and strain energy method for one specific input's set shown that the difference equals up to few percent. Under these circumstances and because of a convenience the strain energy method was used for structural analysis of the single load ring.

Input

- Loads

The loads acting on the single load rings changes with rotation angle of the wheel and number of single load rings. They depend also on the load case (see Table 3.1) and the way of mounting them into the rim. Because the system was statically indeterminate, the defining the loads acting on the single load cell was assumed with the rule of the worst case.

- Material properties

The large ratios of *0.2% proof strength* and *modulus of elasticity* $\frac{R_{p0.2}}{E}$ allows large deflections within proportional range. That ensures better accuracy. The Young's Modulus is more or less constant for steels and alloys. Therefore the fatigue body of transducer is made of alloy spring steel *51CrV4*. This material is usually used in production of heavily loaded springs, shocks, shafts and is especially recommended for load cells transducer.

Table 3.2 Properties of alloy spring steel 51CrV4

Property	Symbol	Unit	Value
Nominal diameter	d	*mm*	*> 16*
Nominal thickness	t	*mm*	*> 8*
0.2 % proof strength	$R_{p0.2}$	*MPa*	*min 900*
Tensile strength	R_m	*MPa*	*1100 - 1300*
Min elongation at fracture	*A5*	*%*	*min 9*
Modulus of elasticity	E	*GPa*	*210*

- Geometry parameters

Only four dimensions *R, b*, *t* and *L*, see , are used to design single load ring. The first three dimensions (*R*, *b* and *t*) mainly affect the maximum stress and obviously sensitivity, deflections and rotations. Usually two of them may be chosen by the designer and the third is then fixed by allowable stress. In case of WFTMD the dimensions *R*, *b* were more or less determined by the rim and tractor's front hub with planet gear. The equation drawn from elasticity theory are valid for *R > 2t* [55]. The influence of *L* is so small that it is usually neglected by structural analysis and it is determined usually by free space in the device. Convenience in fabrication and in

mounting strain gages was also kept in mind when selecting ring dimensions. The chamfer is made with a *45 [°]* angle in order to keep the thickness *t* unchanged in crucial locations. One of the main advantages of load rings over the more simple strain gage transducer is the ability to obtain high sensitivity (or obtain high maximum strain) without obtaining large deflections. From the assumption that central plane of rings should lie possibly in the central plane of the rim in order not to provide an arm for normal force of payload, the dimension *2(R + t)* can equal about *100 [mm]*. The exactly dimensions were calculated within equations putted into Maple worksheet.

Structural Process

The analysis of a ring is based on Castigliano's theorem which states: "if external force act on a structure which is subjected to small and linear deflection in its direction than the deflection of the point of application of the force is equal to the partial derivative with respect to the force of the total internal strain energy in this structure [55]". Castigliano's Theorem can be extended to include rotations at the point caused by applied moments. The strain energy, *U*, due to bending moment is expressed as

$$U = \frac{1}{2} \cdot \int \frac{M^2}{E \cdot I} \cdot dx \qquad [3.2]$$

M represents the moment at location *x*, *E* is the modulus of elasticity, *I* is the moment of inertia about neutral axis, and *x* is the coordinate describing the position along the length of the beam. If the beam is curved, and has a radius of curvature *R*, then *dx* may be replaced by $R \cdot d\varphi$, where φ is the angular coordinate.

$$U = \frac{1}{2} \cdot \int \frac{M^2 \cdot R}{E \cdot I} \cdot d\varphi \qquad [3.3]$$

Equation **[3.3]** will result in very small errors if *R > 2t*, where *t* is the thickness of the ring. Calculation of the vertical displacement, δy, the horizontal displacement, δx, and the rotation, ω, of the top of the ring, relative to the bottom can be accomplished by application of Castigliano's theorem and are described in Hoag and Yoerger paper [55, 56]. The theorem is applied to both the left half and right half of the ring. The coordinate directions for the displacement and rotations are shown in **Figure 3.6**,

and the subscripts *l* and *r* are used to denote the left hand and right hand halves of the ring, respectively.

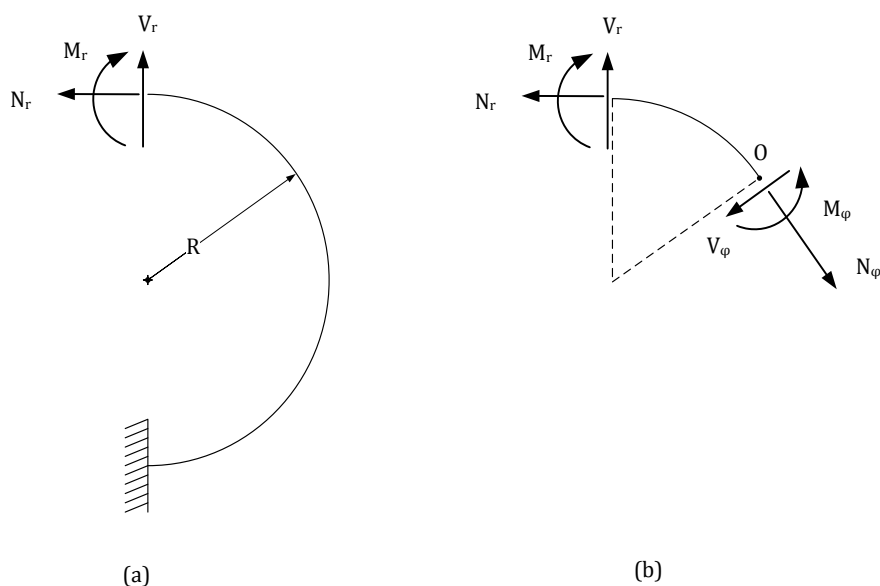(a)   (b)

Figure 3.6 Bending moment in the circular portion of load ring

The right hand portion of the ring is shown in **Figure 3.6 a** with the bottom fixed. N_r, V_r, and M_r indicate the normal force, shear force, and bending moment at the top right of the ring, respectively. A portion of the right half of the ring, with the indicated moments and forces, is shown in **Figure 3.6 b**. The moment at an arbitrary point of the ring, φ, may be determined by equating the summation of moments about point O to zero.

$$M_\varphi = M_r + V_r \cdot R \cdot \sin(\varphi) - N_r \cdot R \cdot (1 - \cos(\varphi)) \qquad [3.4]$$

and the strain energy can be determined thanks to equation **[3.3]**

$$U = \frac{1}{2} \int \frac{M_\varphi^2 \cdot R}{E \cdot I} d\varphi \qquad [3.5]$$

Using the equation **[3.4]** and **[3.5]** it is possible to calculate following deformations:

- vertical deflection

$$\delta_{yr} = \frac{\partial U}{\partial V_r} = \frac{\partial U}{\partial M_\varphi} \cdot \frac{\partial M_\varphi}{\partial V_r} \qquad [3.6]$$

$$\delta_{yr} = \frac{R^2}{E \cdot I} \cdot [2 \cdot M_r + \frac{V_r \cdot R \cdot \pi}{2} - 2 \cdot N_r \cdot R] \qquad [3.7]$$

- horizontal deflection

$$\delta_{xr} = -\frac{\partial U}{\partial N_r} = -\frac{\partial U}{\partial M_\varphi}\frac{\partial M_\varphi}{\partial N_r} \qquad\qquad [3.8]$$

$$\delta_{xr} = \frac{R^2}{E \cdot I} \cdot \left[M_r \cdot \pi + 2 \cdot V_r \cdot R - \frac{3}{2} \cdot N_r \cdot R \cdot \pi \right] \qquad\qquad [3.9]$$

- rotation

$$\omega_r = \frac{\partial U}{\partial M_r} = \frac{\partial U}{\partial M_\varphi}\frac{\partial M_\varphi}{\partial M_r} \qquad\qquad [3.10]$$

$$\omega_r = \frac{R}{E \cdot I} \cdot [M_r \cdot \pi + 2 \cdot V_r \cdot R - N_r \cdot R \cdot \pi] \qquad\qquad [3.11]$$

For left hand side portions of the ring the equation **[3.4]** must be replaced by following one

$$M_\alpha = M_l - V_l \cdot R \cdot \sin(\alpha) - N_l \cdot R \cdot (1 - \cos(\alpha)) \qquad\qquad [3.12]$$

and instead of equation **[3.5]** is

$$U = \frac{1}{2} \int \frac{M_\alpha{}^2 \cdot R}{E \cdot I} d\alpha \qquad\qquad [3.13]$$

- vertical deflection

$$\delta_{yl} = -\frac{\partial U}{\partial V_l} = -\frac{\partial U}{\partial M_\varphi}\frac{\partial M_\varphi}{\partial V_l} \qquad\qquad [3.14]$$

$$\delta_{yl} = \frac{R^2}{E \cdot I} \cdot \left[2 \cdot M_l + \frac{V_l \cdot R \cdot \pi}{2} - 2 \cdot N_l \cdot R \right] \qquad\qquad [3.15]$$

- horizontal deflection

$$\delta_{xl} = \frac{\partial U}{\partial N_l} = \frac{\partial U}{\partial M_\varphi}\frac{\partial M_\varphi}{\partial N_l} \qquad\qquad [3.16]$$

$$\delta_{xl} = \frac{R^2}{E \cdot I} \cdot \left[2 \cdot V_l \cdot R + \frac{3}{2} \cdot N_l \cdot R \cdot \pi - M_l \cdot \pi \right] \qquad\qquad [3.17]$$

- rotation

$$\omega_l = -\frac{\partial U}{\partial M_l} = -\frac{\partial U}{\partial M_\varphi}\frac{\partial M_\varphi}{\partial M_l} \qquad\qquad [3.18]$$

$$\omega_l = \frac{R}{E \cdot I} \cdot [N_l \cdot R \cdot \pi - M_l \cdot \pi + 2 \cdot V_l \cdot R] \qquad\qquad [3.19]$$

The vertical deflections, the horizontal deflections, and the rotations on the top left and right hand portion of the ring are not necessarily the same. The relations one to

another may be expressed in terms of the elongations of the beam portions, and the vertical deflections and slopes at the ends of the beam portions.
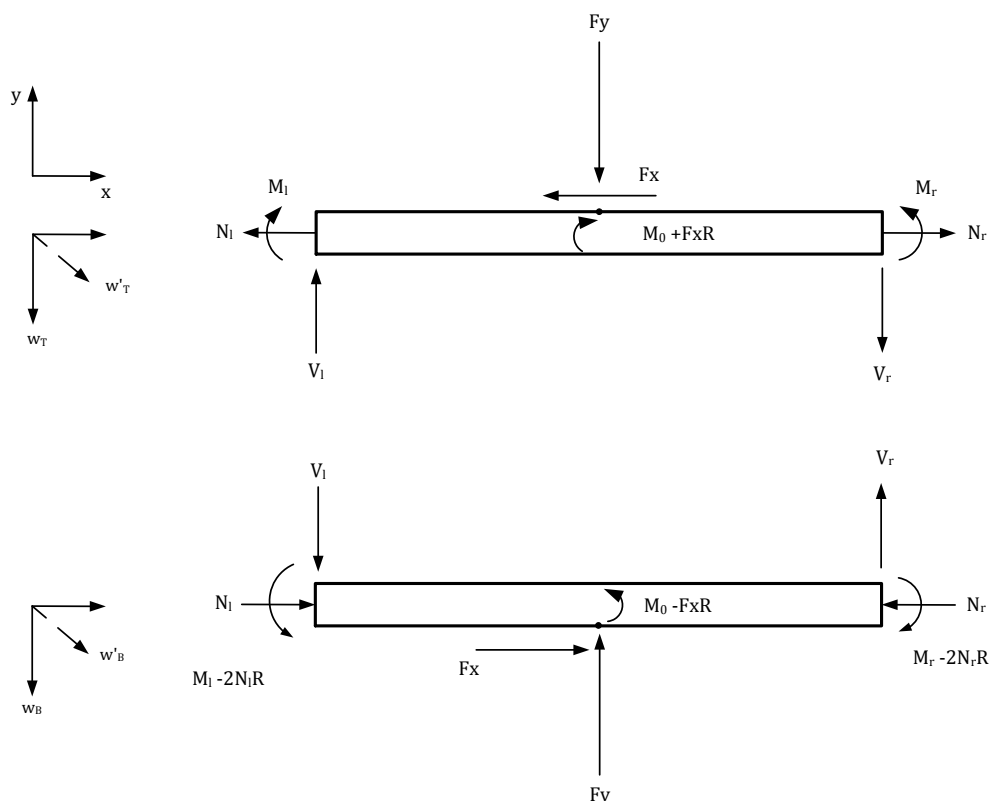
Figure 3.7 Center extended portions of load ring

The top and the bottom beam sections are shown on . The deflections, w, measured downward, and the slopes, w', measured clockwise, are subscripted by T and B, respectively.

$$\delta_{yl} = w_{B(0)} - w_{T(0)} \qquad [3.20]$$

$$\delta_{yr} = w_{B(2L)} - w_{T(2L)} \qquad [3.21]$$

$$\delta_{xr} - \delta_{xl} = \Delta \qquad [3.22]$$

$$\omega_l = w'_{T(0)} - w'_{B(0)} \qquad [3.23]$$

$$\omega_r = w'_{T(2L)} - w'_{B(2L)} \qquad [3.24]$$

The symbol Δ represents the axial extension of the beam. The denotation *(0)* and *(2L)* mean evaluation of w and w' at *x = 0* for left hand side and *x = 2L* for right hand side of the ring. The stiffness of the beam portions of the extended ring is usually very large in comparison to the stiffness of the ring portions (in the order of *100:1*). Therefore an analysis of the extended ring can be approximated very well by considering the beam portions to infinitely rigid.

An infinitely rigid beam will not experience any change in curvature due to applied loads. Thus

$$w_{T(2L)} = w_{T(0)} + 2 \cdot w'_{T(0)} \qquad\qquad [3.25]$$

$$w_{B(2L)} = w_{B(0)} + 2 \cdot L \cdot w'_{B(0)} \qquad\qquad [3.26]$$

$$w'_{T(2L)} = w'_{T(0)} \qquad\qquad [3.27]$$

and

$$w'_{B(2L)} = w'_{B(0)} \qquad\qquad [3.28]$$

The relative axial extension would be zero due to large cross sectional area of the beams. Using this conditions there are following equation describing rotation and deflection between left and right side of the ring.

$$\omega_r = \omega_l \qquad\qquad [3.29]$$

$$\delta_{xr} = \delta_{xl} \qquad\qquad [3.30]$$

$$\delta_{yr} = \delta_{yl} - 2 \cdot L \cdot \omega_r \qquad\qquad [3.31]$$

The major difference between the simple ring and the extended ring is that the upper points of the two semi-circular ends on the extended ring tend to be constrained from rotation due to a horizontal load, *Fx*, while being free to rotate due to an externally applied moment. The difference is due to the fact that rotation cannot take place at the tops of the semi-circular sections without rotation of the center of extension portions, and a horizontal force will not tend to rotate the center portion while an externally applied moment will cause them to rotate. This may be analyzed by considering the horizontal load, *Fx,* to have an accompanying constrained moment of *Fx·R* on the top and bottom beam portion.

Output

The six equations of vertical, horizontal deflections and rotations for both left and right hand portions **([3.7],[3.9],[3.11],[3.15],[3.17],[3.19])** and three equations for relation between left and right portions **([3.29] – [3.31])** represent nine equations and twelve unknowns. The remaining three equations may be determined from the three conditions of either the top or bottom beam. The equilibrium equations may be determined from**:**

$$V_l = Fy + V_r \tag{3.32}$$

$$N_l = N_r - Fx \tag{3.33}$$

$$M_l = M_r - Fy \cdot L - Fx \cdot R - M_0 - 2 \cdot L \cdot V_r \tag{3.34}$$

The final equations that are needed to calculate all outputs are listed in the appendix A.1. The crucial output is **structural strength** because it defines if one designed load ring will hold out the external loads $\sigma < \sigma_{allow}$. The equations of bending moment are responsible for stress distribution and it was obtained after substituting already calculated unknowns. The maximum absolute value of the bending moment may be determined from the moment equation. If the maximum absolute lies within one of the two given regions, then its position may be found by setting the derivative of the moment, with the respect to φ. The maximum is where derivative equals zero. The moment equation may be then evaluated at that position. The maximum absolute value of the moment may not occur within the region, but rather at the boundary, and thus the moment should be also evaluated at the two boundaries of each region. By designing for the strength, the maximum stress occurs always on inside surface of the ring. Because of non-linear stress distribution across the cross section sometimes is used for calculations its distributions the curved beam stress formula.

$$\sigma = E\varepsilon = \left| \frac{6\,K M_{max}}{b\,t^2} \right| \tag{3.35}$$

The proper K factor (curved beam correction factor) for the inside of a ring with a rectangular cross section depends on the ratio R/t. The K factor may be neglected only if $R/t > 5$. In this particularly case this requirement wasn't fulfilled but the K factor was neglected because a large safety factor. The reason was uncertainty in the magnitudes of the applied loads onto single load ring.

The next parameter is **sensitivity** which is actually the ratio of force and strain $\left(\frac{F_x}{\varepsilon x} \right.$, $\left. \frac{F_y}{\varepsilon y} \right)$. This must be so designed that for one given smallest entity of load cause strain that can be detected by the strain gage.

The **stiffness** has also big influence for the whole measuring hub. Using the Castigliano's theory the deflections can be calculated in dependence on the loads. So

the plain stiffness is the acting force divided by deflection δ or external acting moment divided by rotation ω.

Separation

Other feature that can be easy calculated with an analytical way is separation. In general eight strain gauges can be switched into three Wheatstone's full-bridges so the bridge outputs will essentially be proportional to force *Fx, Fy*, and moment *M₀*. Each output will be almost independent of the other two loads. However this separation is not ideal and it depends on particularly dimensions. The zero point means that the signal generated through force *Fx* is independent from the force *Fy* and it is located at

$$\sin(\varphi) = \frac{2}{\pi}$$ [3.36]

which is constant and equals $sin(\varphi) = \frac{2}{\pi} = 39.54°$. Second zero point where signal generated through force *Fx* is independent from the external moment *M₀* is located at

$$\varphi = arcsin \frac{2 + \dfrac{R \cdot \pi}{2 \cdot L}}{\dfrac{2 \cdot R}{L} + \pi}$$ [3.37]

In this case the angle depends on from R and L dimension. Because of the fact that the signal of external moment is not necessary to calculate to forces acting in the center of the wheel this ability has been not used in this solution. It saves the necessity of making a compromise between separation of *Fx* direction from influence of the moment *M₀*. However the separation of forces acting along *x* and *y* axis is still important. The solid mechanically separation enables to decrease so called cross-over feature between these two signals. This is the significant improvement in relation to the way proposed by Just [54]. The way described above let to build the mathematical model for single extended load ring.

During FE analysis of single load ring all stresses were usually lightly higher than in strain energy method. As a result of finite element analysis the foot of the extended load ring was introduced. This change has relieved the deformable circular portions of the ring from its physical restrain. By this method the screw joint were also validated.

3.3.2   Model of the WFTMD

Having the equation calculating strength, sensitivity and stiffness for the single load ring and as well defined loads in the center of the rim and also defined the material of transducers the analysis of the whole measuring hub was carried out. The stiffness of the WFTMD was calculated first. A big issue played amount of single load rings. The concept lied down that all deformable frames were fixed between two carrier plates so that the stiffness of the whole measuring device was the sum of singular transducer's stiffness. The most important issue was that stiffness of the whole measuring hub must be possible invariable in whole range of revolution. This fact is particularly important for prevention of any excitation in consequence of rotation.

The procedure of calculating the stiffness of WFTMD by strain energy method looked as follows. First, the stiffness of load ring in the *xz* plane for every rotational position was calculated. Then the stiffness of the whole measuring hub in function of rotation was calculated. Every two load rings lying against each other in the revolution created always one pair. This fact was used for simplification. In case of six load rings, the WFTMD was imagined as three springs with different stiffness value. Going further, for six transducers the common stiffness varied within *60°* ranges. For one position of WFTMD by certain load the whole plate moved in certain direction and certain magnitude. Those deflections were fed back into the stiffness of single load ring and so the force acting on every single extended load ring was calculated. The stress and strain were calculated in the same manner. The mathematical model of WFTMD, with different number of load rings, was derived in this way. It was valid through the whole rotation. The mathematical model was done for measuring hub with 4, 6 or 8 sensor bodies in circumference. Because of the fact that there was a risk of mistake in the equations and the fact that some stresses were neglected, the structural FE analysis of WFTMD was conducted in parallel. During this approach many studies were carried out, but only few of them are described in this work.

In the final solution the six load rings were restrained (see fixed, green arrows in **Figure 3.8**) from one side and from other side they were subjected to six loads. The point of application of the external forces was placed in the origin of center axis

coordinate system *(XC, YC, ZC)*. The stiffness difference of the measuring hub was checked as the first value within FE analysis. The maximal radial force equaled *73.6 [kN]*. It was applied as the static force caused by payload and impact load factor. In case the force acts along the axis, *OX*, the maximal deflection equaled, *UX = 0.135 [mm]*. In the same hub rotation but in case the force acts along the axis, *OZ*, the maximal deflection equaled, *UZ = 0.138 [mm]*. The difference of *3 [µm]* was so minimal that excitation by rotational speed were neglected.
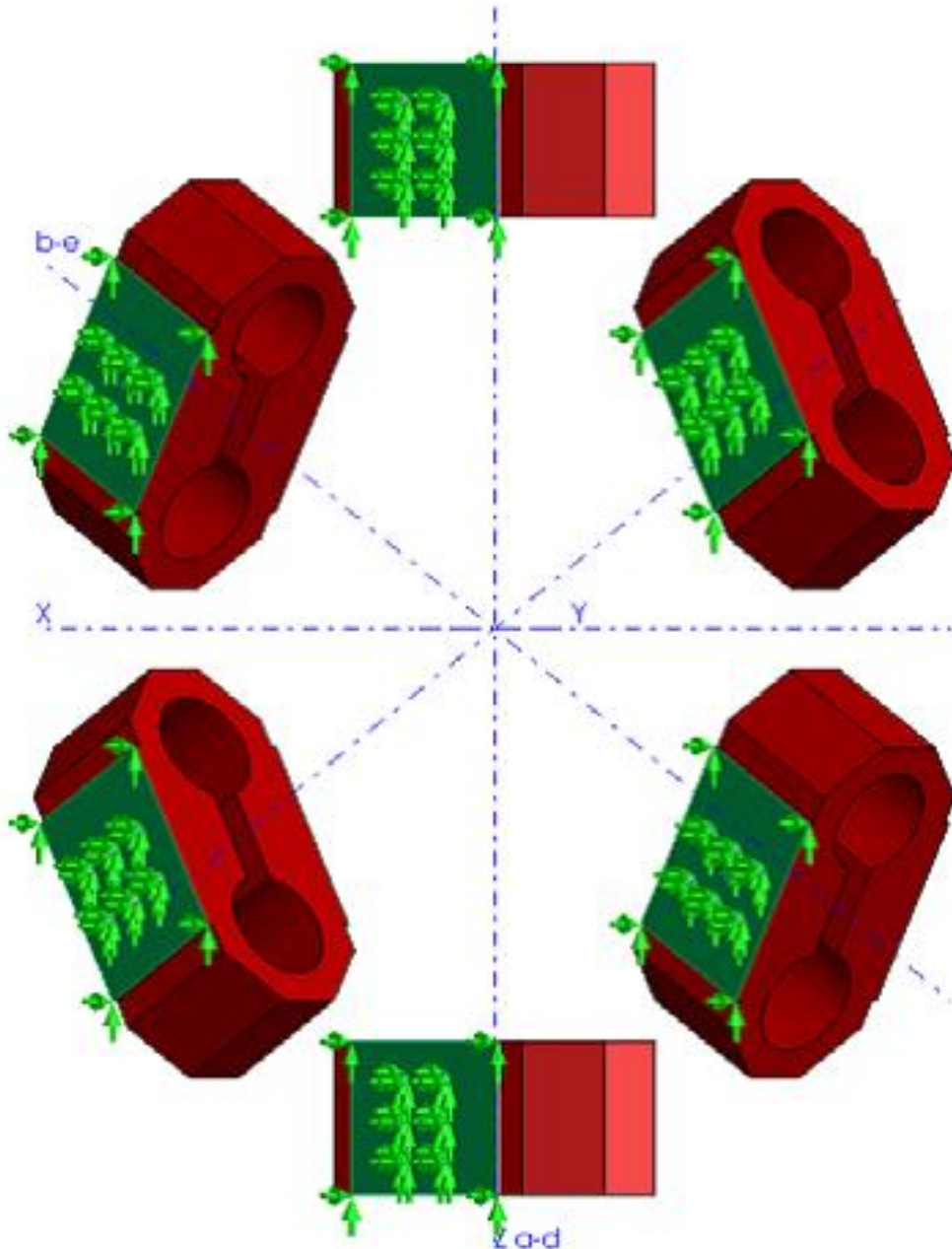

Figure 3.8 Isometric view of final FE-model of the WFTMD

The difference in deflection in case of four load rings was about *2 [mm]*. Taking into account that the shape tolerance of *38 inches* rear tractor tire is *2 [mm]* too and

those two values may add at certain mounting configuration, the risk for uncontrolled excitation was too big. The deflection difference for eight load rings was insignificantly less than for six transducers but the complexity of measuring hub, especially in aspect of signal flow would be unnecessarily. Finally, six load rings revealed the optimum solution. Six load rings are located in the real device, as shown in **Figure 3.8**.

The FE-Analysis and results

The whole measuring device must be strong enough to measure critical loads and as well sensitive enough to measure values of load for smallest weights and smallest slip angles. For that purpose the FE analysis was carried out for seven load cases defined by wheel slip angle and the payload.

Table 3.3 Load cases and their maximal stresses

				case no.						
				1	*2*	*3*	*4*	*5*	*6*	*7*
Conditions:	wheel slip angle	α	°	*0*	*45*	*90*	*15*	*5*	*5*	*5*
	payload	F_{Z_C}	*t*	*7.5*	*7.5*	*7.5*	*7.5*	*7.5*	*1.5*	*0.8*
Results:	maximal stress	σ	*MPa*	*396*	*577*	*480*	*419*	*420*	*83*	*44*

The conditions and maximal stresses for every load case are presented in the Table 3.**3**. The biggest stresses occurred for second case. The high stress concentration on the corners where neglected as the consequence of insufficient meshing quality. These three-dimensional stresses were summarized by using the von Misses hypothesis. This approach is meant only for linear deflections, which also served as the basis for this undertaking.

The resolution of the AD converter defines the smallest perceptible step of resistance change within the transducers using strain gauges technology. But in practice of sensor design there is a lower limit of strain set to *10^{-6} [m/m]* that must be full field by the transducers body. The upper limit of strain for transducers body is set to *0.1%*. It must be present in the position of the strain gauges by nominal load. This limit is directly related to the yield strength of sensor body material and the safety factor. The range of strains for every load case, see the Table 3.3, is presented in the **Figure 3.9**. The highest strain appeared for case 2 that confirms the maximal

value of stress in the same case. Even for that case the maximum strain remains much less than the strain reflecting the safety factor of *2*.

This analysis enabled to find the right geometry of the single load cell and the whole WFTMD. The transducers were designed in such a way that the strains were distributed within the desired range of *<0,0001%; 0,1%>*. Moreover the strain oscillated around *0,1%.* Only the values of strain for case 6 and 7 are relatively low but still higher than the lower limit of 10^{-6} *[m/m].*
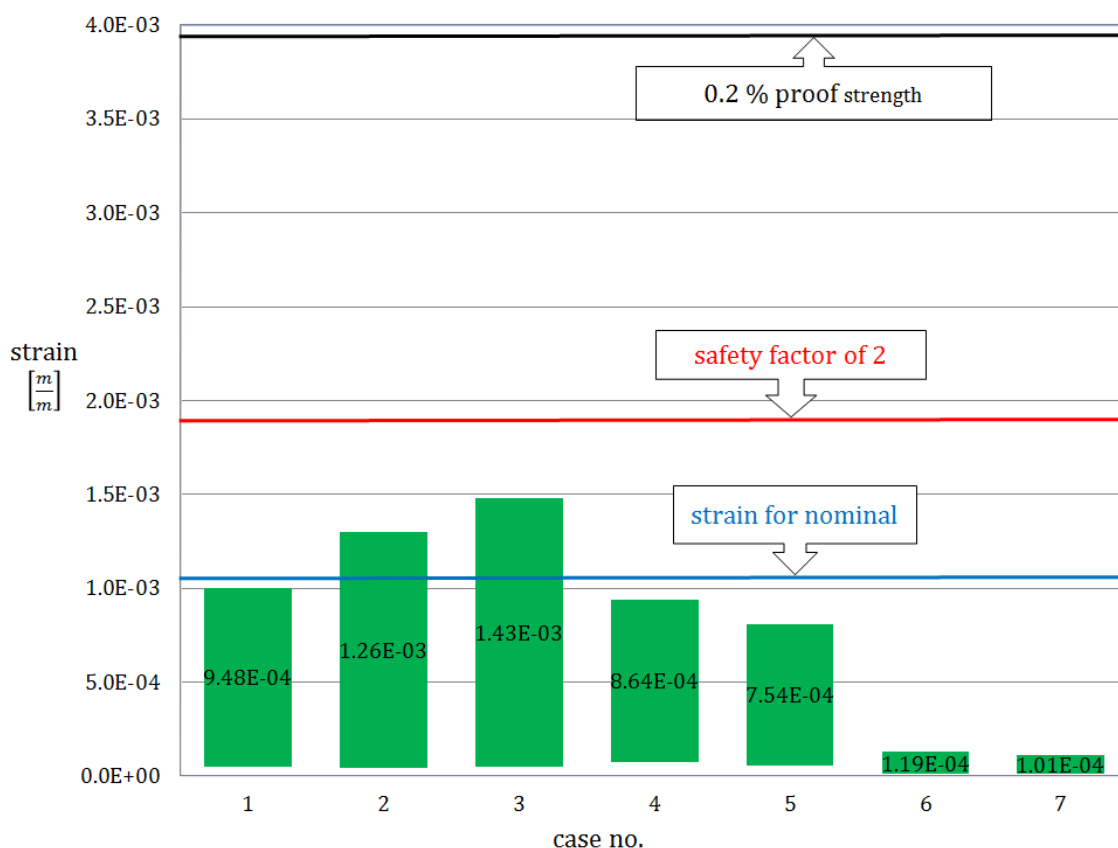
Figure 3.9 Ranges of strain in the position of strain gauges for every case

The final dimensions of WFTMD and the extended load ring are presented in the Table 3.4. Some dimensions as radius of the ring *R* for instance is not directly to read off from the drawing. However, the technical drawing of load ring is shown in appendix A.2. The condition of *R > 2t,* which is necessary for using the strain energy method, is full field [55, 56].

Table 3.4 Geometry of single load ring and the WFTMD

Name	Symbol	Unit	Valve
Half extension	L	mm	50
Radius of the ring	R	mm	45
Radius of the hole	rr	mm	27.5
Thickness of the ring	t	mm	17.5
Width of the ring	b	mm	75
Ratio R/t	R/t	-	2.6
Radius of the fixing circle	r_{MD}	mm	257

3.4 Measurement engineering

Five among six sensors bodies were subjected to electroless nickel plating. It was applied in order to release the stress from surface after tooling and prevent corrosion. The transducers are made of alloy spring steel 50CrV4. The strain gages are made of highly elastic alloy "constantan" that can strain up to *2%*.

3.4.1 Signal in extended load ring

Eight active sensing elements are mounted on the single extended load ring as shown in **Figure 3.10**. Their nominal resistance equals *350 [Ω]*. Some technical data of strain gages series G manufactured by HBM is presented in appendix A.3 [57]. If the forces *Fx* and *Fy* act as it is indicated in the **Figure 3.10** the SGs highlighted in red measure tensile strain. The SGs highlighted in blue measure compressive strain. Unlike as suggestion of Just [54] the ability of measuring the moment is not used. The output voltage, e_{Fx}, is related to the input voltage, V_{Exc}, by the following equation:

$$\frac{e_{Fx}}{V_{Exc}} = \frac{\frac{R1}{R2}}{\left(\frac{R1}{R2} + 1\right)} - \frac{\frac{R4}{R3}}{\left(\frac{R4}{R3} + 1\right)} \qquad [3.38]$$
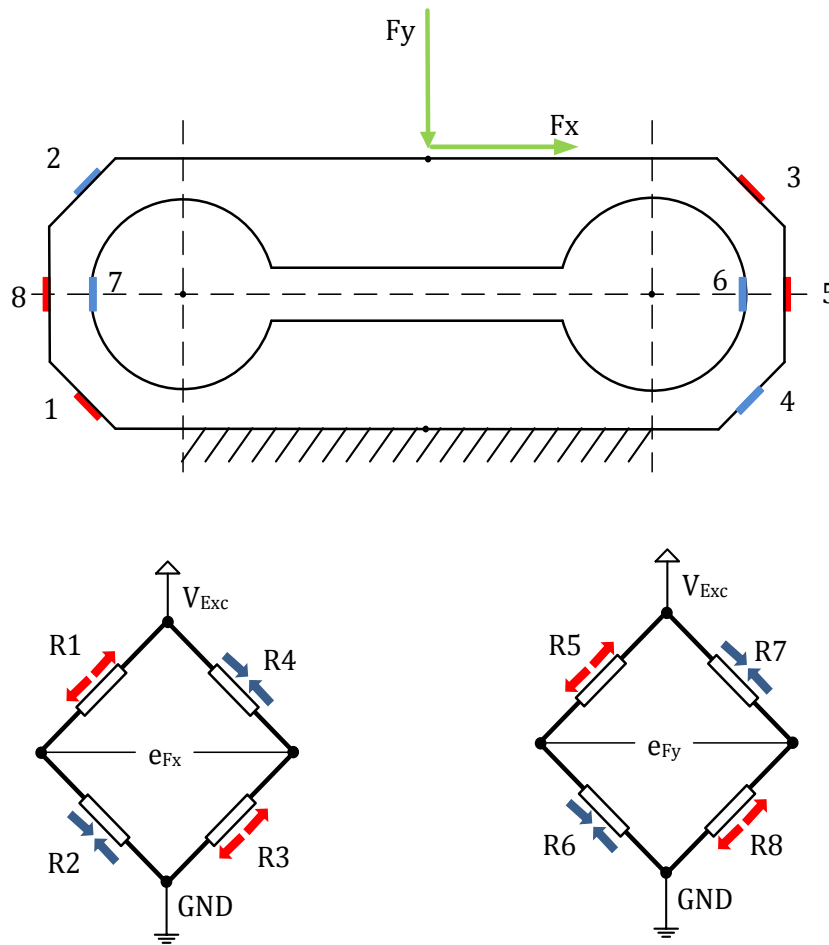
Figure 3.10 Location of strain gages and circuits for particular signals
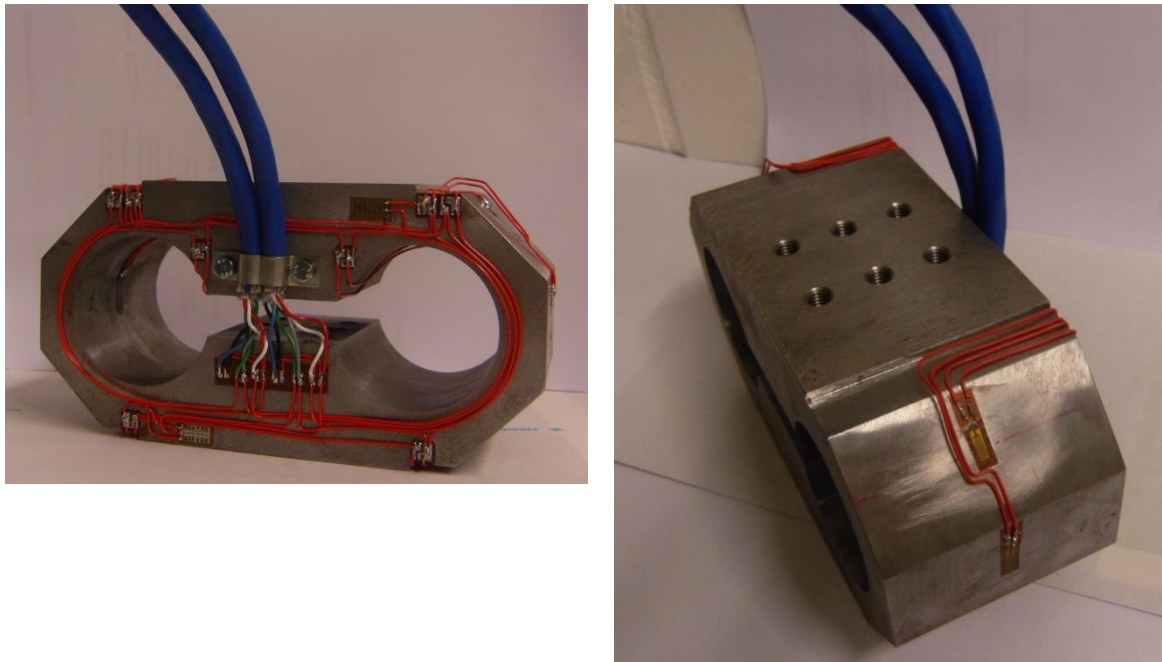

Figure 3.11 The single load ring f with glued on eight strain gauges before nitriding

The output is zero if all strain gauges have the same nominal resistance and are unloaded. A minute change in resistance caused by acting forces, results in measurable output voltage. The small offset in gage resistance by unloaded transducers, so called apparent strain, was balanced to zero by resistance foil. The minimal strains are usually caused by gluing. Changes in temperature can affect the nominal resistance of the strain-sensing material and induce strain on the strain gauge due to differences in thermal expansion coefficients between the alloy steel and constantan. However the full bridge circuit automatically compensates for temperature. Ignoring the geometry of transducer that defines stiffness and sensitivity but taking into account only material properties, maximal strains can be calculated from the Hook's equation:

$$\sigma = \varepsilon \cdot E \qquad [3.39]$$

Considering that stress is replaced by *0.2% proof strength* and *safety factor* $\sigma = R_{p0.2}/SF$ the maximal strain can be calculated as follows:

$$\varepsilon \leq \frac{R_{p0.2}}{SF \cdot E} = \frac{900\ MPa}{2 \cdot 210000\ MPa} = 0.0021 \qquad [3.40]$$

It equals $\varepsilon \leq 0.21\%$. Taking into account that according to know – how from measuring engineering the strains for nominal load should equal *0.1%* it responds of *safety factor* about *4*. The dependency between change of resistance and strain is defined by following equation:

$$\frac{\Delta R}{R} = GF \cdot \varepsilon \qquad [3.41]$$

where *gain factor* for the particular strain gauges equals GF $\cong$ 2.07. Therefore the change of resistance for nominal strain equals

$$\Delta R = R \cdot GF \cdot \varepsilon = 350\Omega \cdot 2 \cdot 0.001 = 0.7\Omega \qquad [3.42]$$

The resistance of strain gauge stretched by nominal loads equals *350.7 [Ω]*. Keeping in mind the strain resolution, the smallest resistance increase step equals $\Delta R_{min} = 0.0007[\Omega]$. The voltage output by nominal loads for full bridge equals

$$U_{out} = GF \cdot \varepsilon \cdot U_{Exc} \qquad [3.43]$$

In this particularly case by excitation voltage of *1 [V]* the output signal equals *2 [mV]*.

3.4.2   Signal in the WFTMD

Six deformable fatigue bodies are mounted in the WFTMD as shown in the **Figure 3.12**. They rotate in the wheel center plane $X_C Z_C$. The load rings are noted with small letters *a* to *f*. The notation *ax* means the signal of load ring *a* in the direction *x*. The formal assumption says that the physical value that is proportional to the measured force is the voltage.
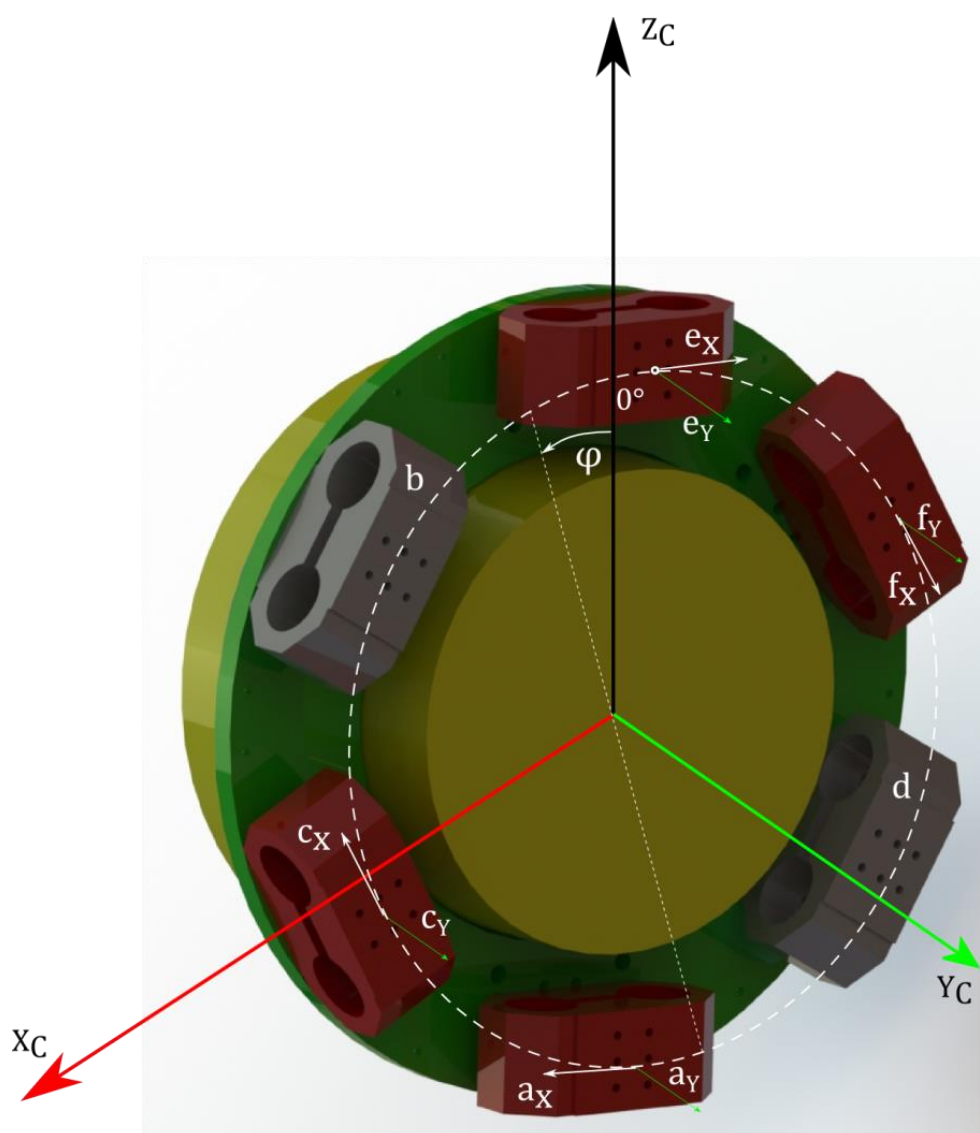
Figure 3.12 Location single load rings in the center axis system

The positive voltage signals are generated when the force acts in direction of axis *x* or *y*. The wheel rotation angle φ is measured counter-clockwise. The zero degrees position is when the load ring *f* is located at the 12 o'clock. In this position the axis *fx* is parallel to the axis X_C and points out in the opposite direction. The axis *y* of every load ring is parallel to the axis Y_C and they point

out in the same direction. The notations in the sketch are the same as on real force hub, therefore it may be used as the technical documentation. Each load ring has the same mechanical stiffness. But only on four load rings *a*, c, e and *f* are applied strain gauges so that every load cell is turned into two force transducers. It means that the WFTMD contains two pairs of load rings lying in front of each other. All together transducers are able to measure four forces in *x* and four in *y* directions. Thus to assign all six loading components in C-axis system (three forces $F_{X_C}, F_{Y_C}, F_{Z_C}$ and three torques $M_{X_C}, M_{Y_C}, M_{Z_C}$) are used eight force signals and one signal defining actually angle of rotation φ of the WFTMD.
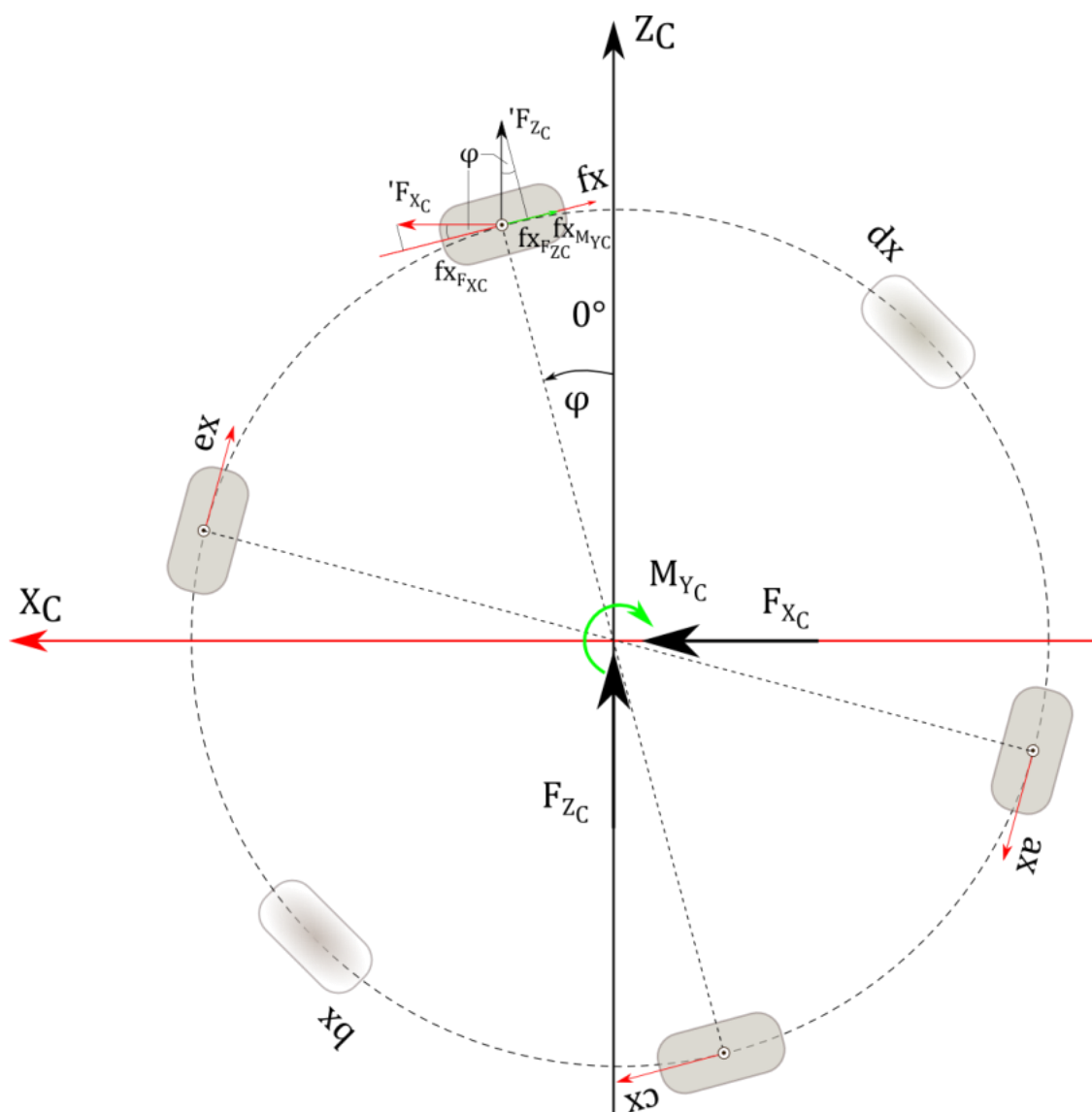

Figure 3.13 The forces in the $X_C Z_C$ plane

The mathematical algorithm to assign the force F_{X_C}, F_{Z_C} and moment M_{Y_C}

In the **Figure 3.13** are shown load rings *a* to *f*. The signals of transducer *f* for axis *x* contains components of longitudinal and vertical force F_{X_C}, F_{Z_C} and braking moment M_{Y_C} in the following proportions:

$$fx_{FXC} = 'F_{X_C} \cdot \cos(\varphi) \qquad\qquad [3.44]$$

$$fx_{FZC} = 'F_{Z_C} \cdot \sin(\varphi) \qquad\qquad [3.45]$$

$$fx_{MYC} = M_{Y_C}/6 \qquad\qquad [3.46]$$

After projection on the axis *fx* the overall fx signal contains

$$fx = -fx_{FXC} + fx_{FZC} + fx_{MYC} \qquad\qquad [3.47]$$

The equation **[3.47]** describes the influence of external loads in dependence on the location of single load ring. Deriving the equation **[3.44]** to **[3.47]** for the rest of load ring we become:

Load ring *e*

$$ex_{FXC} = 'F_{X_C} \cdot \cos(\varphi + 60°) \qquad\qquad [3.48]$$

$$ex_{FZC} = 'F_{Z_C} \cdot \sin(\varphi + 60°) \qquad\qquad [3.49]$$

$$ex_{MYC} = M_{Y_C}/6 \qquad\qquad [3.50]$$

$$ex = -ex_{FXC} + ex_{FZC} + ex_{MYC} \qquad\qquad [3.51]$$

Load ring *c*

$$cx_{FXC} = 'F_{X_C} \cdot \cos(\varphi) \qquad\qquad [3.52]$$

$$cx_{FZC} = 'F_{Z_C} \cdot \sin(\varphi) \qquad\qquad [3.53]$$

$$cx_{MYC} = M_{Y_C}/6 \qquad\qquad [3.54]$$

$$cx = cx_{FXC} - cx_{FZC} + cx_{MYC} \qquad\qquad [3.55]$$

Load ring *a*

$$ax_{FXC} = 'F_{X_C} \cdot \cos(\varphi + 60°) \qquad\qquad [3.56]$$

$$ax_{FZC} = 'F_{Z_C} \cdot \sin(\varphi + 60°) \qquad\qquad [3.57]$$

$$ax_{MYC} = M_{Y_C}/6 \qquad\qquad [3.58]$$

$$ax = ax_{FXC} - ax_{FZC} + ax_{MYC} \qquad\qquad [3.59]$$

Taking into account that every load ring has the same stiffness and the same distance to the wheel rotation axis *YC,* the signal portion induced by the braking moment is the same in every load ring:

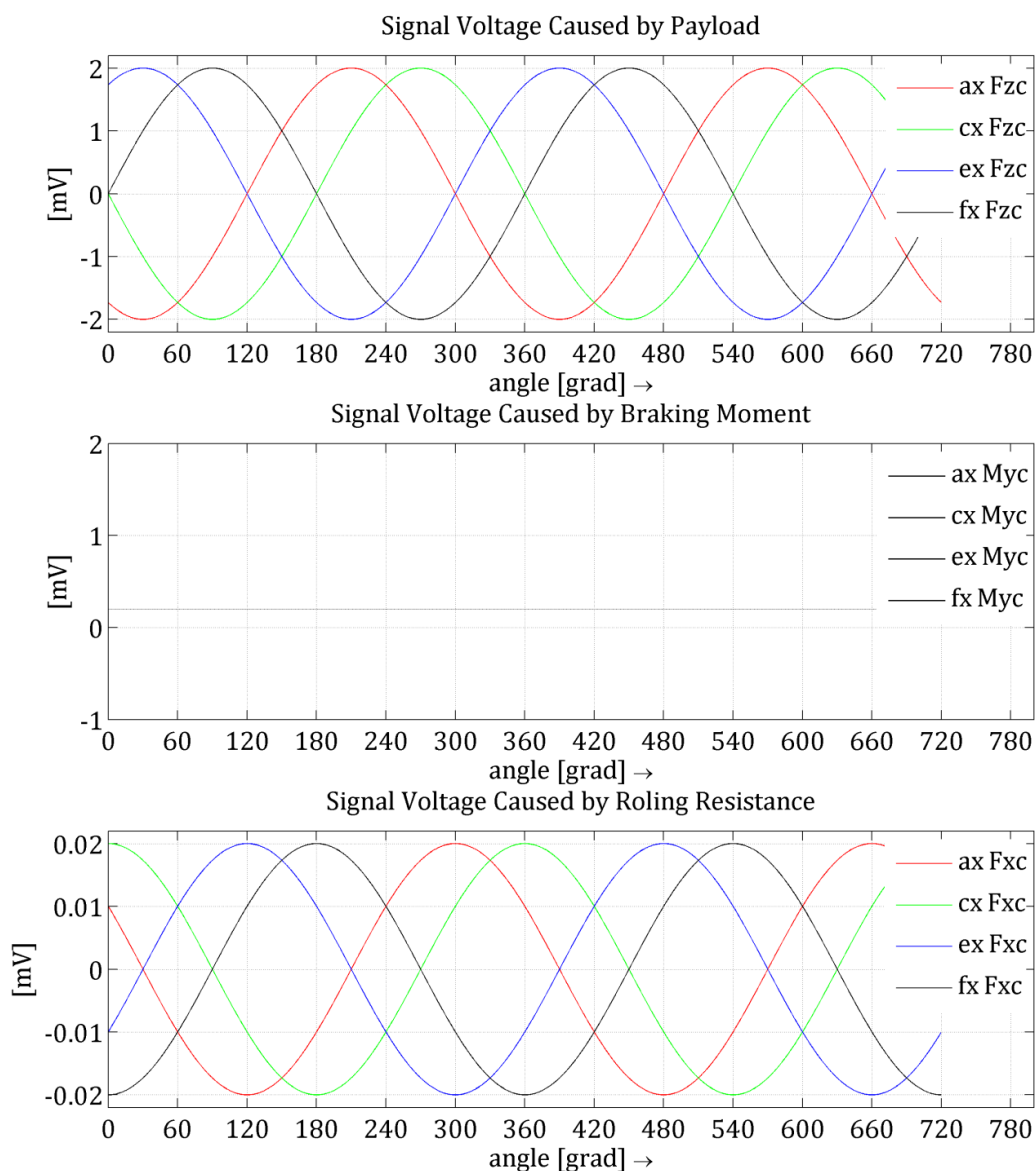$$ax_{M_{YC}} = cx_{M_{YC}} = ex_{M_{YC}} = fx_{M_{YC}} \qquad\qquad [3.60]$$

Figure 3.14 Signals in every load ring in the X_CZ_C plane caused by external loads

Therefore by subtracting the signals form two load rings lying in front of each other we can cross out the portion of braking moment:

$$fx - cx = -fx_{F_{XC}} + fx_{F_{ZC}} + cx_{F_{XC}} - cx_{F_{ZC}} \qquad\qquad [3.61]$$

If we substitute the term **[3.44]**,**[3.45]** and **[3.52]**,**[3.53]** into the equation **[3.61]** we obtain:

$$sig2 = signal_{fx-cx} = -2 \cdot 'F_{X_C} \cdot \cos(\varphi) + 2 \cdot 'F_{Z_C} \cdot \sin(\varphi) \quad \text{[3.62]}$$

After applying the same operation to the *e* and *a* load ring, it yields:

$$sig1 = signal_{ex-ax} = -2 \cdot 'F_{X_C} \cdot \cos(\varphi + 60°) + 2 \cdot 'F_{Z_C} \cdot \sin(\varphi + 60°) \quad \text{[3.63]}$$

In this way the equations **[3.62]** and **[3.63]** deliver system of two equations with two unknowns.

The solution is:

$$F_{X_C} = \frac{sig1 - sig2 \cdot \frac{\sin(\varphi+60°)}{\sin(\varphi)}}{2 \cdot \cos(\varphi + 60°) 2 \cdot \cos(\varphi) \cdot \frac{\sin(\varphi+60°)}{\sin(\varphi)}} \quad \text{[3.64]}$$

$$F_{Z_C} = \frac{sig2 + 2 \cdot F_{X_C} \cdot \cos(\varphi)}{2 \cdot \sin(\varphi)} \quad \text{[3.65]}$$

The trigonometric function appears in both formulas **[3.63]** and **[3.64]** in the denominator. Every sinus and cosines function goes two times through zero within one rotation. Additionally the shift about *60 [°]* causes that the poles are translated. Thus causes significant signals' fluctuations. This mathematical solution does not work properly therefore another approach was applied.

The algorithm for calculating the forces F_{X_C}, F_{Z_C} and moment M_{Y_C} in the $X_C Z_C$ plane works inversely to the way how the forces are induced in the center of the wheel. In the **Figure 3.14** are presented top to the bottom mathematically produced signals caused by payload $F_{Z_C} = 200[kN]$, braking moment $M_{Y_C} = 2\ [kNm]$ and longitudinal force $F_{X_C} = 2\ [kN]$. Just to make the algorithm more clearly the values were divided by amplification coefficient, roughly *10*. It lets to present the signals in the range of *[mV]* instead of *[kN]*. The external loads acts as presented in the **Figure 3.13** through the two whole rotations.

Next all individual signals caused by payload, braking moment and longitudinal force for each load ring were added to create summary signals. Their superpositions are presented in the **Figure 3.15**. The top plot presents signals from every load rings in function of time in order to make them as they are acquainted into DAQ device. It is easy to see that the amplitude in comparison to the top diagram in the **Figure**

3.14 stayes roughly unchaged. It is shifted lightly to the top because of the influence of the braking moment. On bottom plot in **Figure 3.15** the signals are presented as function of rotation angle φ. It is easy to see the influence of the longitudinal force. Because of it the peaks of resultand signals are lightly shifted towards higher angles.
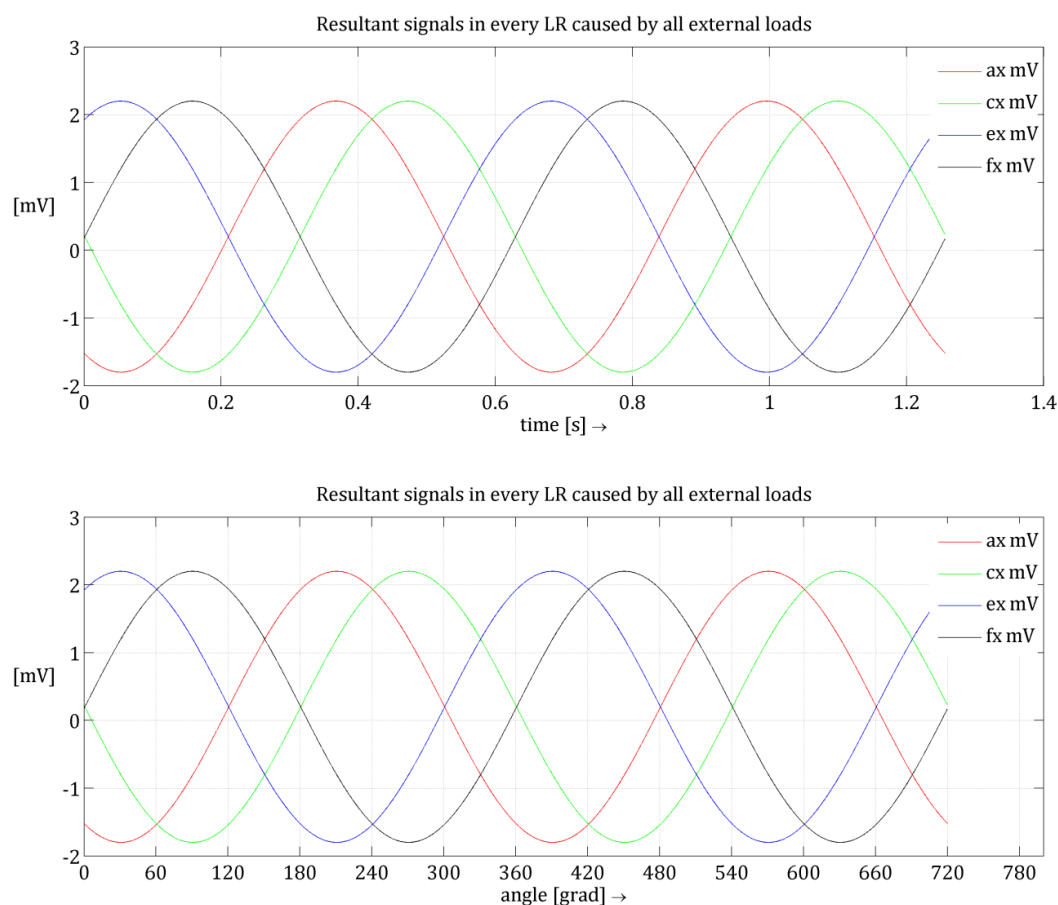
Figure 3.15 Signals in load rings in the X_CZ_C plane caused by all external loads

They are used to establish and check the algorithm for calculating the components: F_{X_C}, F_{Z_C} and $\boldsymbol{M_{Y_C}}$. The basic assumption in this algorithm is that there is no external force applied direct along the axis XC. In other words the real longitudinal force appears as a result of braking, traction moment or rolling resistance. In all those situations occurring separately the moment around rotation axis M_{Y_C} reflects the longitudinal force. Therefore the longitudinal force is calculated from moment about wheel center rotation axis YC.

In order to calculate the vertical force, first the signals from two load rings lying in front of each other are subtracted to get rid of the moment about the wheel center

rotation axis *YC*. The signals *sig1* and *sig2* are expressed by equation **[3.62]** and **[3.63]** and are shown in the **Figure 3.16**.

The signals *sig1* and *sig2* are further divided by $\sin(\varphi)$ and $\sin(\varphi + 60°)$. The resulting signal is shown in the **Figure 3.16** too. Every time when the trigonometric from denominator function goes through zero, that is two times per one rotation, the referencing function reaches very high values, here cut off out of the plot. Therefore the vertical force F_{Z_C} is calculated in dependence to rotation angle once from $sig1/(2 \cdot \sin(\varphi + 60°))$ and for other angle range from $sig2/(2 \cdot \sin(\varphi))$.

$$F_{Z_C} = f(\varphi, \frac{sig2}{2 \cdot \sin(\varphi)}, \frac{sig1}{2 \cdot \sin(\varphi + 60°)})$$
[3.66]
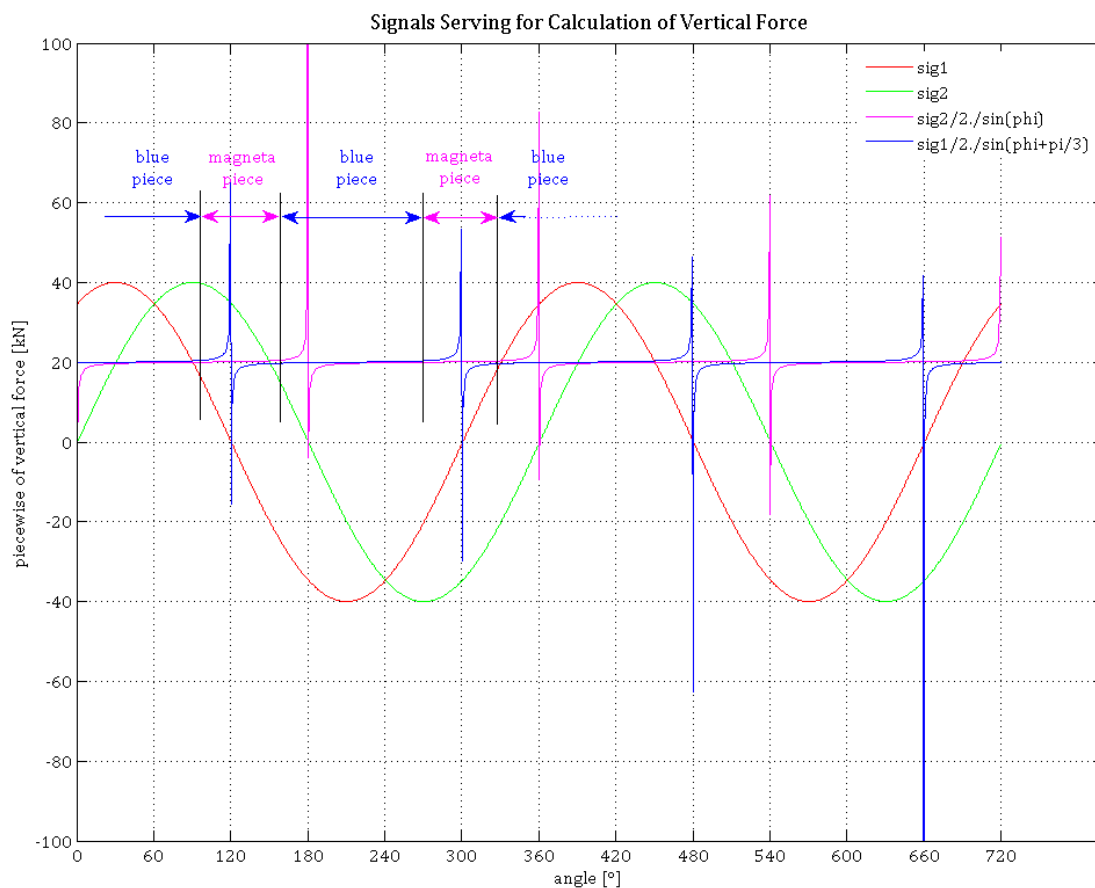
Figure 3.16 Signals in load rings in the *XCZC* plane caused by all external loads plotted in function of angle

This method of calculation the longitudinal force presented by equation **[3.66]** provide good results for artificially created longitudinal forces that is smaller than *10%* of vertical force $F_{X_C} \leq 10\% \cdot F_{Z_C}$.

For calculation of the moment about the wheel center rotation axis Y_C two signals from pair of load rings that lay in front of each other must be added in order to get rid of the components from the force F_{X_C} and the force F_{Z_C} that have the same value but opposite direction, see the **Figure 3.13** and equations **[3.44]** - **[3.60]**. Therefore, to assign the moment M_{Y_C} it is enough to add signals along axis x of any load rings lying in front of each other without taking into account the rotation angle. In this case the force in single load ring induced by braking or driving moment equals:

$$F_{\text{LR } M_{YC}} = \frac{F_{ax} + F_{ex}}{2}$$

[3.67]

Because the moment is distributed on six load rings and acts on the radius r_{MD}, the M_{Y_C} equals:

$$M_{Y_C} = 6 \cdot F_{\text{LR } M_{YC}} \cdot r_{MD}$$

[3.68]

Figure 3.17 The forces in the yφ plane

The mathematical algorithm to assign the moment M_{X_C}, M_{Z_C} and force F_{Y_C}

In the **Figure 3.17** only load rings a to f are shown. The signals of transducer f in the direction of y axis contains components of three external loads M_{X_C}, M_{Z_C} and F_{Y_C} in the following proportions:

$$fy = fy_{M_{ZC}} \cdot \sin(\varphi) \cdot r_{MD} - fy_{M_{XC}} \cdot \cos(\varphi) \cdot r_{MD} + fy_{F_{YC}} \quad [3.69]$$
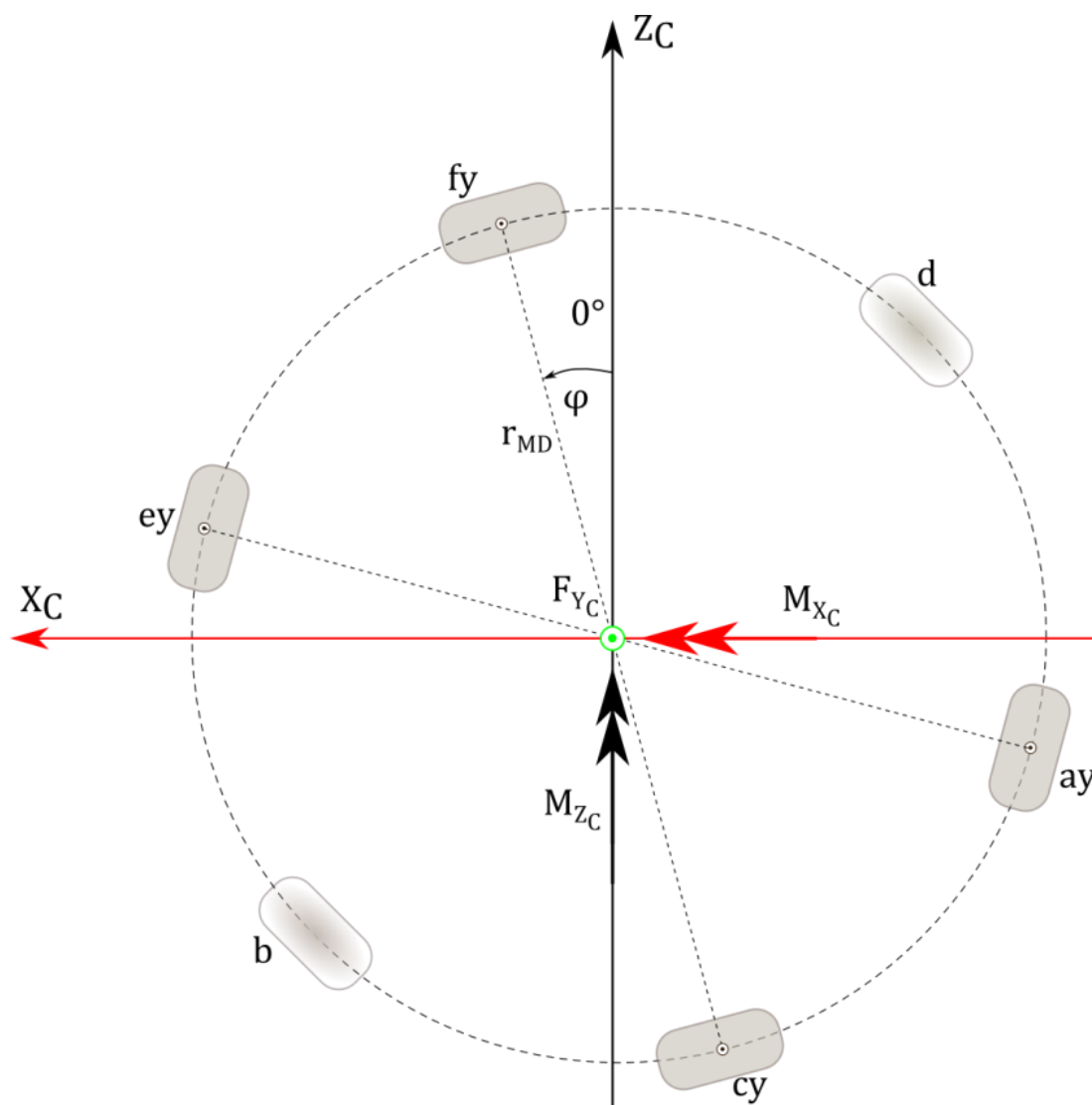
The influence of external loads changes in relationship from the location of single load ring as follows:

$$ey = ey_{M_{ZC}} \cdot \sin(\varphi + 60°) \cdot r_{MD} - ey_{M_{XC}} \cdot \cos(\varphi + 60°) \cdot r_{MD} + ey_{F_{YC}} \quad [3.70]$$

$$cy = -ey_{M_{ZC}} \cdot \sin(\varphi) \cdot r_{MD} + ey_{M_{XC}} \cdot \cos(\varphi) \cdot r_{MD} + cy_{F_{YC}} \quad [3.71]$$

$$ay = -F_{M_{ZC}} \cdot \sin(\varphi + 60°) \cdot r_{MD} + F_{M_{XC}} \cdot \cos(\varphi + 60°) \cdot r_{MD} + ay_{F_{YC}} \quad [3.72]$$

The algorithm to assign the lateral force F_{Y_C} is quite simple. For every pair of load rings that lay in front of each other, the components from the moment M_{X_C} and M_{Z_C} have the same value but opposite direction. Therefore, to assign the lateral force F_{Y_C} is enough to add signals along axis y of any load rings lying in front of each other without taking into account the rotation angle. In this case the force in single load ring induced by lateral force equals:

$$\mathrm{F}_{\mathrm{LR}\, F_{YC}} = \frac{\mathrm{ay} + \mathrm{ey}}{2} \quad [3.73]$$

Because the moment is distributed to six load rings the F_{Y_C} equals:

$$\mathrm{F}_{Y_C} = 6 \cdot \mathrm{F}_{\mathrm{LR}\, F_{YC}} \quad [3.74]$$

==In case when the acting point for longitudinal and vertical force does not lay in the symmetry plane of WFTMD their influence must be reduced.==

The algorithm to assign the moments M_{X_C} and M_{Z_C} is a more complicated. For that purpose two pairs of load rings are needed. That is four signals in plane $y\varphi$ and one signal defining angle of rotation φ. In this way there is created system of two equations with two unknown magnitudes. Every equation is built by subtracting voltage outputs proportional to the force acting on the transducers along axis y that lies in front of each other.

$$fy - cy = 2 \cdot \sin(\varphi) \cdot r_{MD} \cdot {}'F_{M_{ZC}} - 2 \cdot \cos(\varphi) \cdot r_{MD} \cdot {}'F_{M_{XC}} \quad [3.75]$$

and

$$ey - ay = 2 \cdot \sin(\varphi + 60°) \cdot r_{MD} \cdot {'F_{M_{ZC}}} - 2 \cdot \cos(\varphi + 60°) \cdot r_{MD} \cdot {'F_{M_{XC}}} \qquad [3.76]$$

so the force from moment about axis OZ equals

$$F_{M_{ZC}}' = \frac{signal_{fy-fy} - \dfrac{\cos(\varphi + 60°)}{\cos(\varphi)} \cdot signal_{ey-ay}}{\dfrac{\cos(\varphi + 60°)}{\cos(\varphi)} \cdot 2 \cdot \sin(\varphi) \cdot r_{MD} - 2 \cdot \sin(\varphi + 60°) \cdot r_{MD}} \qquad [3.77]$$

and the force from moment about axis OX equals

$$F_{M_{XC}}' = \frac{-signal_{ey-ay}}{2 \cdot \cos(\varphi) \cdot r_{MD}} - \frac{\sin(\varphi) \cdot F_{M_{ZC}}'}{\cos(\varphi)} \qquad [3.78]$$

In order to calculate those moments both forces must mu multiplied by the radius r_{MD}:

$$M_{X_C} = F_{M_{XC}}' \cdot r_{MD} \qquad [3.79]$$
$$M_{Z_C} = F_{M_{ZC}}' \cdot r_{MD} \qquad [3.80]$$

Alike as in formulas **[3.63]** and **[3.64]** also in the formulas **[3.77]** and **[3.78]** appears trigonometric functions in the denominator. Every sinus and cosines function goes two times through zero within one rotation. Because of the significant signals' fluctuations the moments M_{X_C} and M_{Z_C} are not calculated. This measuring hub enables to measure four components: $F_{X_C}, F_{Y_C}, F_{Z_C}, M_{Y_C}$. The application of load rings that can measure forces along three orthogonal axes instead of only two would enable to measure al six components with sufficient accuracy.

3.4.3 Calibration

Every single load ring was calibrated in the facility presented in the **Figure 3.18** on the left hand side. The forces in direction x and y were induced by hydraulic cylinder. The hydraulic circuit of the calibration facility is presented on the right hand side in the **Figure 3.18**. The direction of acting force and its magnitude was adjusted by putting the 4/3 valve in the right position and seting the pressure reducing valve. The direction and exactly value of each force was sensed and acquisited by force sensors.

Simple calibration

The load ring with two full bridges can be presentat as grey box with two inputs and two outputs as presented in the **Figure 3.19 a**. In the first order the load ring was

subjected to the force only in one direction while other hydraulic cylinder was in that time uncoupled. The calibration was caried out with stepwise proceedure without unloading between every step as presented in the **Figure 3.19 b**.
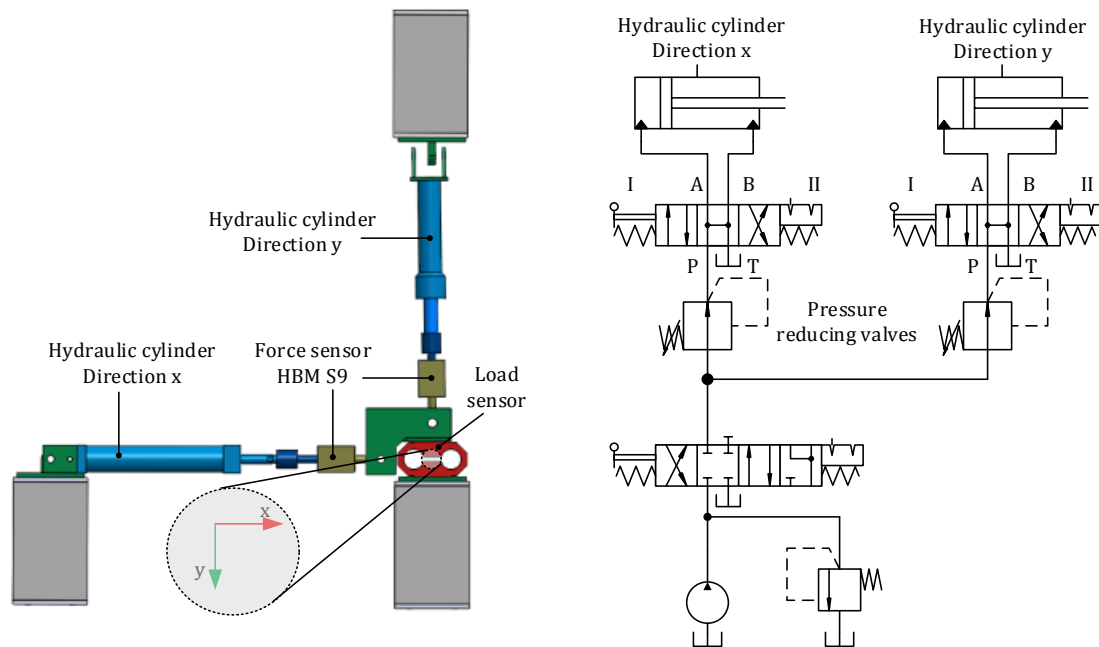

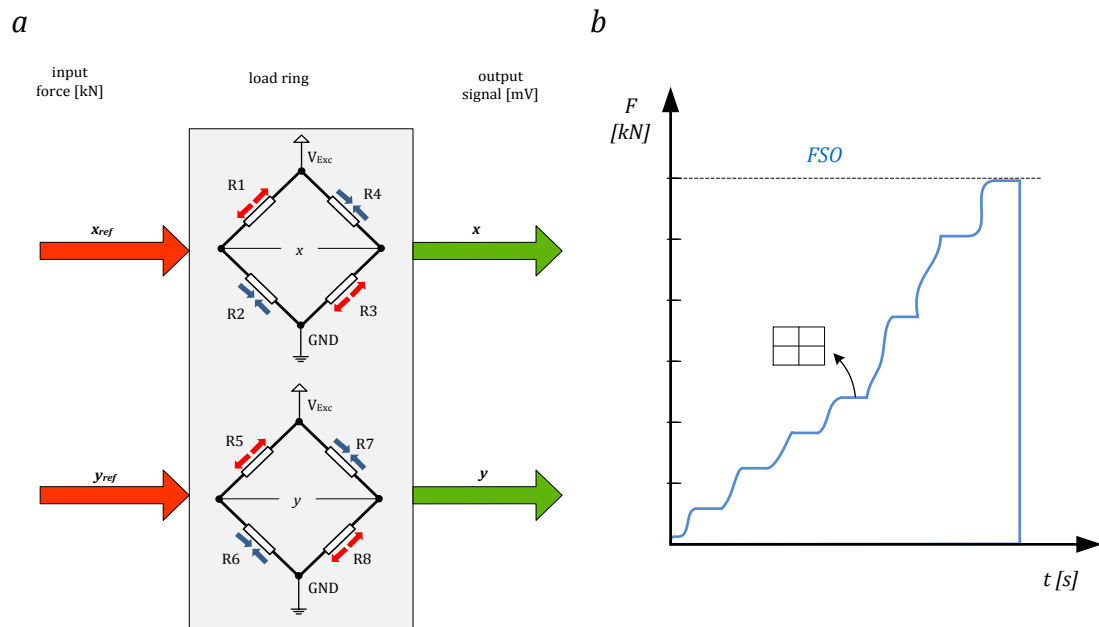**Figure 3.18** Calibration facility of single load ring and its hydraulic circuit

Figure 3.19 The calibration of single load ring; a – inputs and outputs, b – stepwise calibration procedure

During this calibration the three measurement series were always saved by HBM DAQ device and for the certain steps the values were noticed in the table. The input value defining the direction and magnitude of acting force and both outputs that is signal voltage for *x* and *y* direction are presented in the column one to three in the Table 3.5. Up to *10 [kN]* the force was increased in steps of about *1 [kN]* and from magnitude of *10 [kN]* in steps of *2 [kN]* up to *20 [kN]* in positive and negative direction. This author called this procedure 'simple calibration'. It was carried out for both directions.

Table 3.5 Calibration data of transducer *ax*

1	2	3	4	5	6	7
input ax_{ref} [kN]	**output** **ax** **[mV]**	output *ay* [mV]	cross-over talk [%]	*ax* $y = 10.383 \cdot x$ [kN]	difference [kg]	linearity [%]
-20,0	**-1,93**	-0,18	9,3%	-20,0	0,2	0,0%
-18,1	**-1,74**	-0,17	9,8%	-18,1	-0,9	0,0%
-16,1	**-1,55**	-0,16	10,3%	-16,1	0,6	0,0%
-14,1	**-1,35**	-0,15	11,2%	-14,0	1,0	0,1%
-12,0	**-1,16**	-0,14	12,1%	-12,0	3,7	0,3%
-10,6	**-0,97**	-0,12	12,7%	-10,0	57,0	5,6%
-9,1	**-0,87**	-0,12	13,3%	-9,0	0,7	0,1%
-8,1	**-0,78**	-0,11	13,5%	-8,1	0,2	0,0%
-7,0	**-0,68**	-0,09	13,6%	-7,0	1,2	0,2%
-6,0	**-0,58**	-0,08	13,4%	-6,0	-0,3	0,0%
-5,0	**-0,49**	-0,06	12,8%	-5,0	-0,6	-0,1%
-4,0	**-0,39**	-0,05	11,9%	-4,0	0,2	0,1%
-3,0	**-0,29**	-0,03	10,9%	-3,0	0,2	0,1%
-2,0	**-0,20**	-0,02	9,2%	-2,0	0,5	0,3%
-1,0	**-0,10**	-0,01	5,0%	-1,0	-0,9	-0,8%
0,0	**0,00**	0,00	-100,0%	0,0	-1,1	-
1,0	**0,10**	-0,01	-9,4%	1,0	-0,3	0,3%
2,0	**0,19**	-0,01	-7,3%	2,0	-0,7	0,3%
3,0	**0,29**	-0,02	-8,0%	3,0	0,0	0,0%
4,0	**0,39**	-0,04	-9,3%	4,0	1,4	-0,3%
5,1	**0,49**	-0,05	-9,6%	5,1	1,7	-0,3%
6,0	**0,59**	-0,06	-9,9%	6,1	3,5	-0,6%
7,0	**0,68**	-0,07	-10,0%	7,0	3,0	-0,4%
8,0	**0,78**	-0,08	-10,1%	8,0	4,8	-0,6%
9,0	**0,87**	-0,09	-10,0%	9,0	4,4	-0,5%
10,0	**0,97**	-0,10	-9,9%	10,1	5,3	-0,5%
12,0	**1,16**	-0,12	-9,9%	12,1	4,6	-0,4%
14,1	**1,37**	-0,13	-9,8%	14,2	7,5	-0,5%
16,1	**1,56**	-0,15	-9,7%	16,2	8,9	-0,5%
18,1	**1,75**	-0,17	-9,7%	18,1	8,6	-0,5%
20,1	**1,94**	-0,19	-9,63%	20,2	9,5	-0,5%

The measurement data and certain calculations obtained from calibration of transducer *ax* are presented in the Table 3.5. The input denoted with *ax$_{ref}$* relates to the force acting along axis *x* on the load ring *a*. The force is measured by HBM load cell S90 50. The second and third column present transducers' voltage outputs, denoted *ax* and *ay* respectively. Their physical units are *[mV]*. The forth column presents *cross over talk* between direction *ax* and *ay.* It is described by percentage of the direct output. In the calibration range the cross over talk is distributed between *8%* and *14%* which is quite high values and has decreasing tendency for higher absolute values of forces. The fifth column presents the formula of linear trend line going through zero. It was obtained by mathematical regression of two measurement series *ax$_{ref}$* and *ax*. The equation $y = 10.383 \cdot x$ describes the relation between signal voltage output *[mV]* and input acting force *[kN]*. If the value *x* from the formula presented in the fifth column is substituted by full bridge voltage output measured in *[mV]*, the force with *[kN]* units will be obtained. The coefficient of determination $R^2 = 0.9999$ provides a measure of how well outcomes are likely to be predicted by the equation.
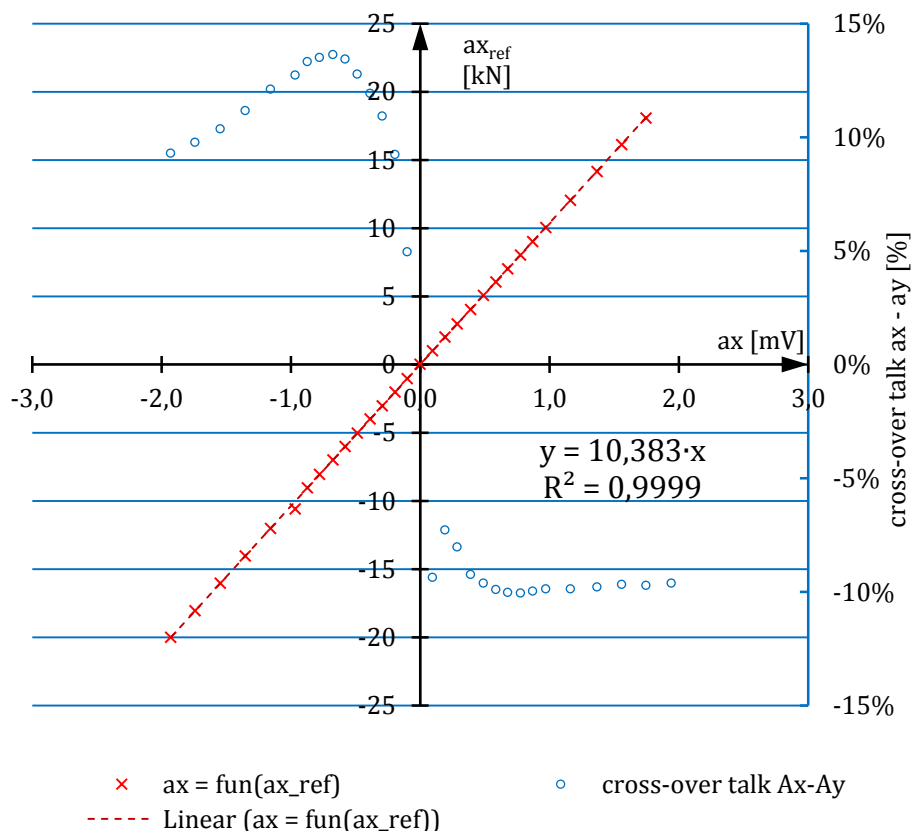
Figure 3.20 The graphical presentation the calibration data of transducer *ax*

The resulting value of R^2 equal to *0.9999* is very good. The sixth column presents the absolute difference in *[kg]* between input measured in *[kN]* and calculated output using the trend line equation. The seventh column presents the linearity values. It is proportional difference between input measured in *[kN]* and calculated output using the trend line equation compared to the full-scale output (FSO) expressed in percent. In the **Figure 3.20** are presented all the information from the Table 3.5. This is graphical representation of results as relation between input and output, the trend line and the cross-over talk.
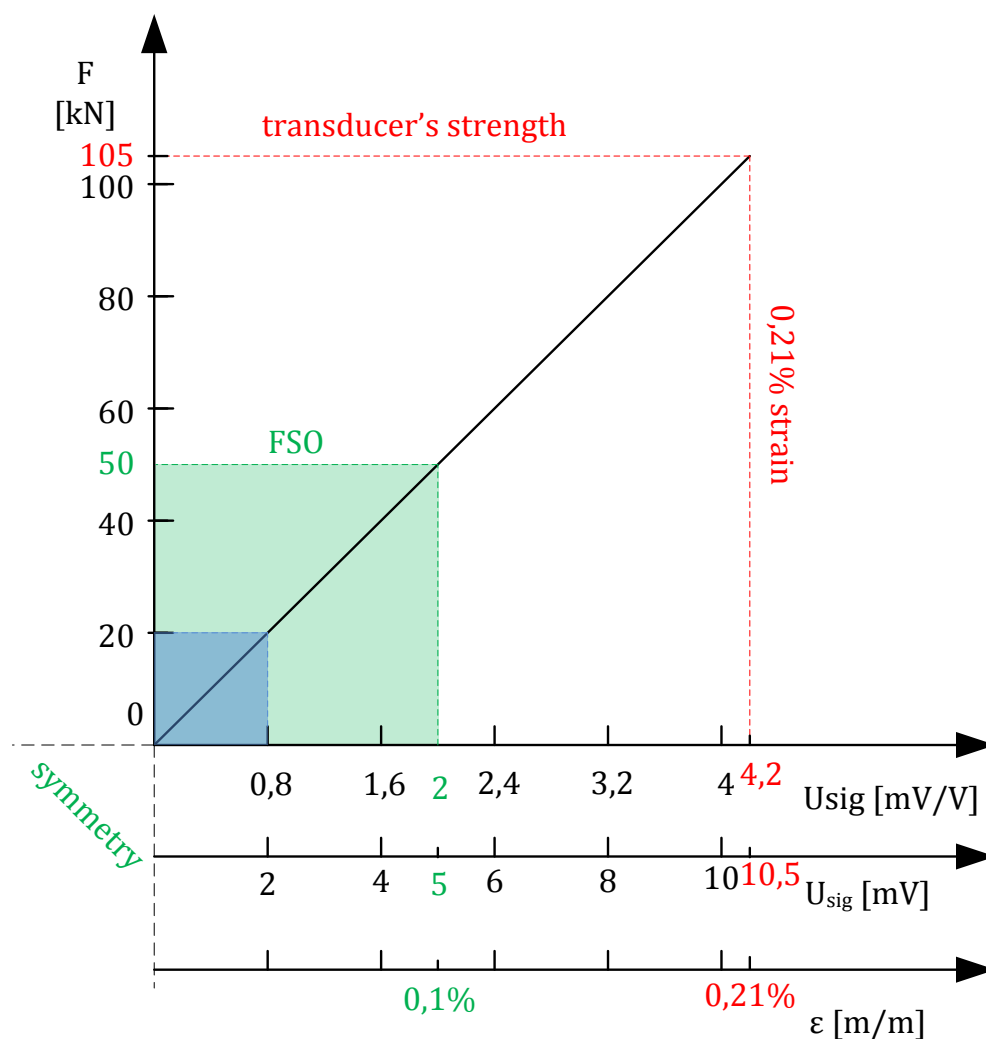
Figure 3.21 The sensitivity of single load ring

According to recommendation from sensor manufacturing industry the strain in the place of strain gauge equals *0.1%* for nominal loads. The electrical sensitivity calculated with equation **[3.43]** equals *2 [mV/V]*. That means that by supplying the full bridges with *2.5 DC [V]* excitation voltages the output should be about *5 [mV]*.

In this case the nominal load that is called as well *full scale output (**FSO**)* for transducer *ax* equals around *50 [kN]*. The graphical presentation of above values is shown in **Figure 3.21**. The range of simple calibration has blue tone. The range of nominal loads has green tone. The strain of *0.21 %* equals to transducer's *0.2% proof strength* divided by *safety factor* of 2. It is marked with the red dashed line.
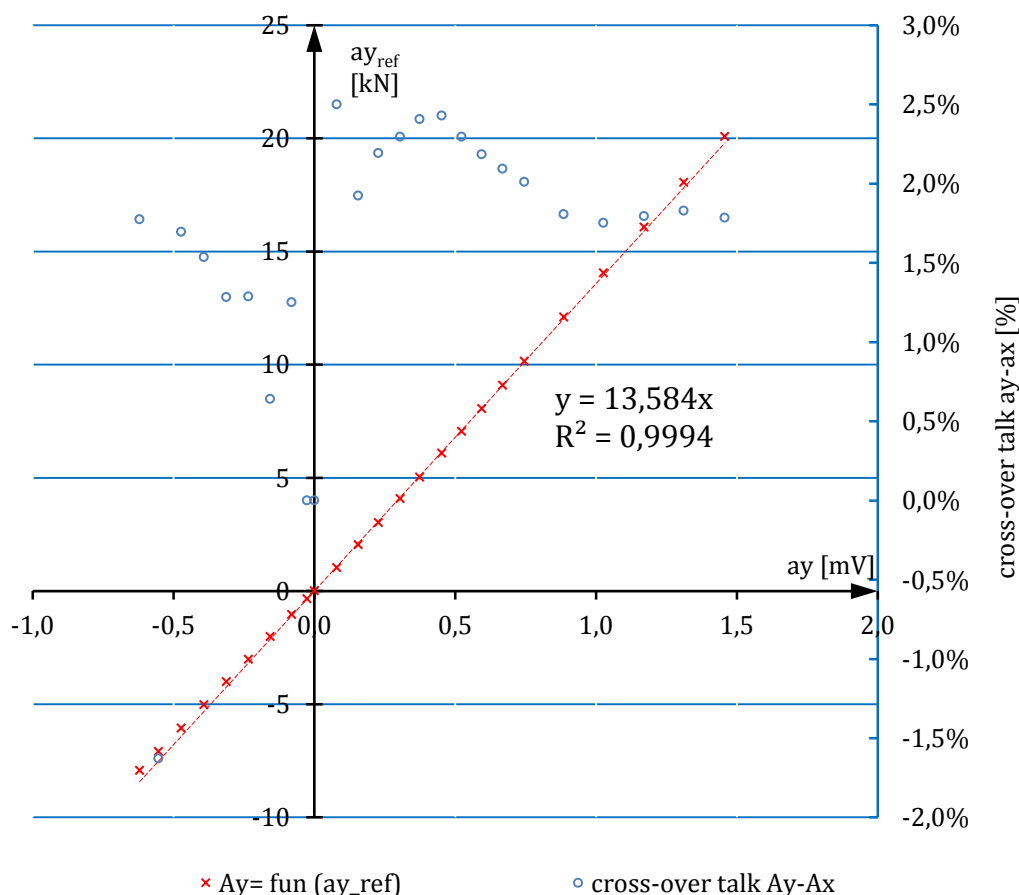
**Figure 3.22** The graphical presentation the calibration data of transducer *ay*

The data of calibration transducer *ay* are presented in the **Figure 3.22**. Because the rod side of hydraulic piston acting in the direction *y* had significantly smaller area the maximal negative force approximates *10 [kN]*. The load ling for direction *y* is a bit stiffer. The nominal load for transducer *ay* equals about *65 [kN]*. The coefficient of determination is worse than for transducer *ax* so the linearity is also worse in this direction. The cross-over talk *ay-ax* is much lower than cross-over talk *ax-ay*. The values lay in the positive range and oscillate around *2%*. Other words the load in *y* direction is almost imperceptible in *x* direction.

The coefficients of trend line of all transducers and the coefficients of determination are listed in the Table 3.6.

Table 3.6 Calibration data of all transducer

transducer	trend line factor	the coefficient of determination
ax	y = 10.383 · x	0.9999
ay	y = 13.584 · x	0.9994
cx	y = 10.646 · x	0.999
cy	y = 13.256 · x	0.9961
ex	y = 10.516 · x	0.9982
ey	y = 13.653 · x	0.9997
fx	y = 10.506 · x	1.0
fy	y = 13.742 · x	0.9995

The tables including calibration data of all other transducer and their graphical presentations are attached in the appendix A.4.
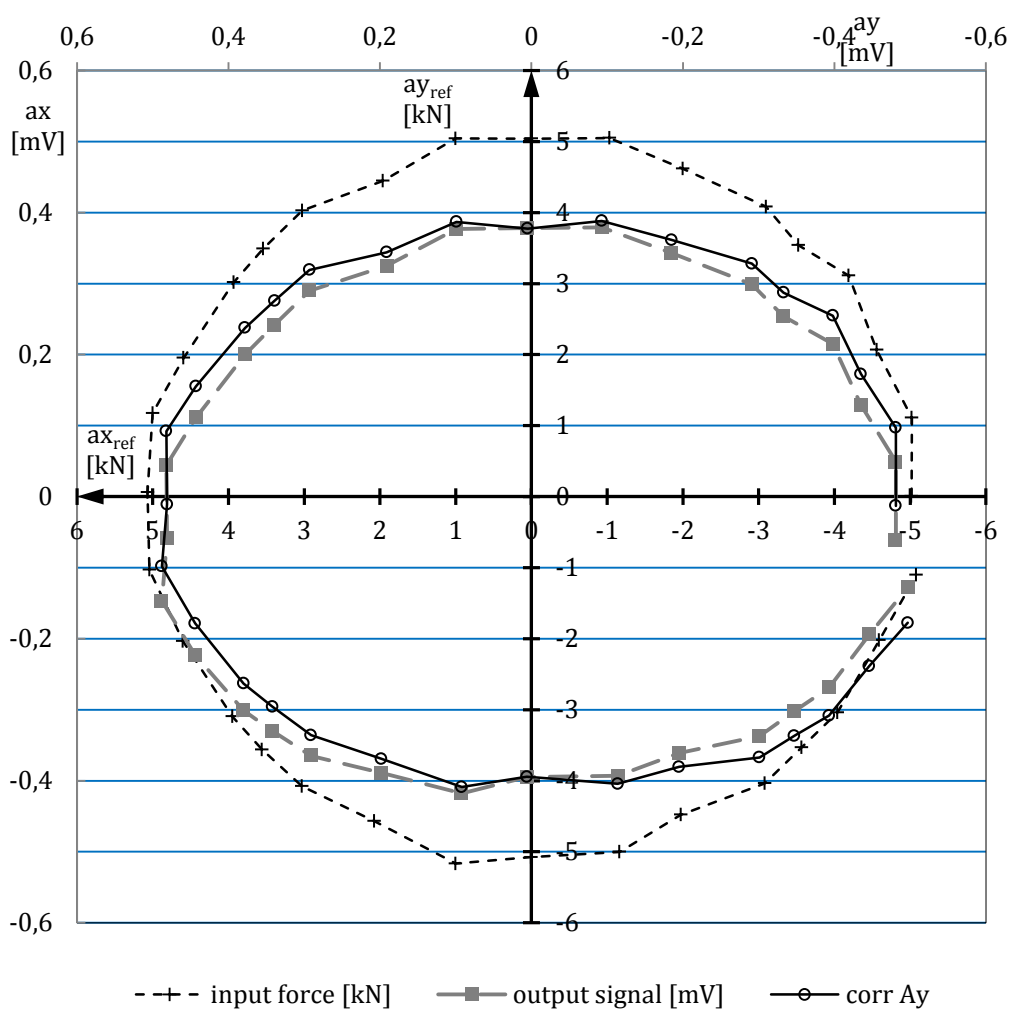
Figure 3.23 The graphical presentation of the calibration in the circle

Calibration in the circle [58, 59]

In another calibration procedure the load ring was loaded with force vector of *500 [N]* that was applied to the same point of application. By changing the proportion between the force induced by two cylinders the peak of the vector rolled the circle.

On the plot presented in the **Figure 3.23** there are three series:

- points of input forces,
- output forces,
- corrected output about cross-over talk ax-ay.
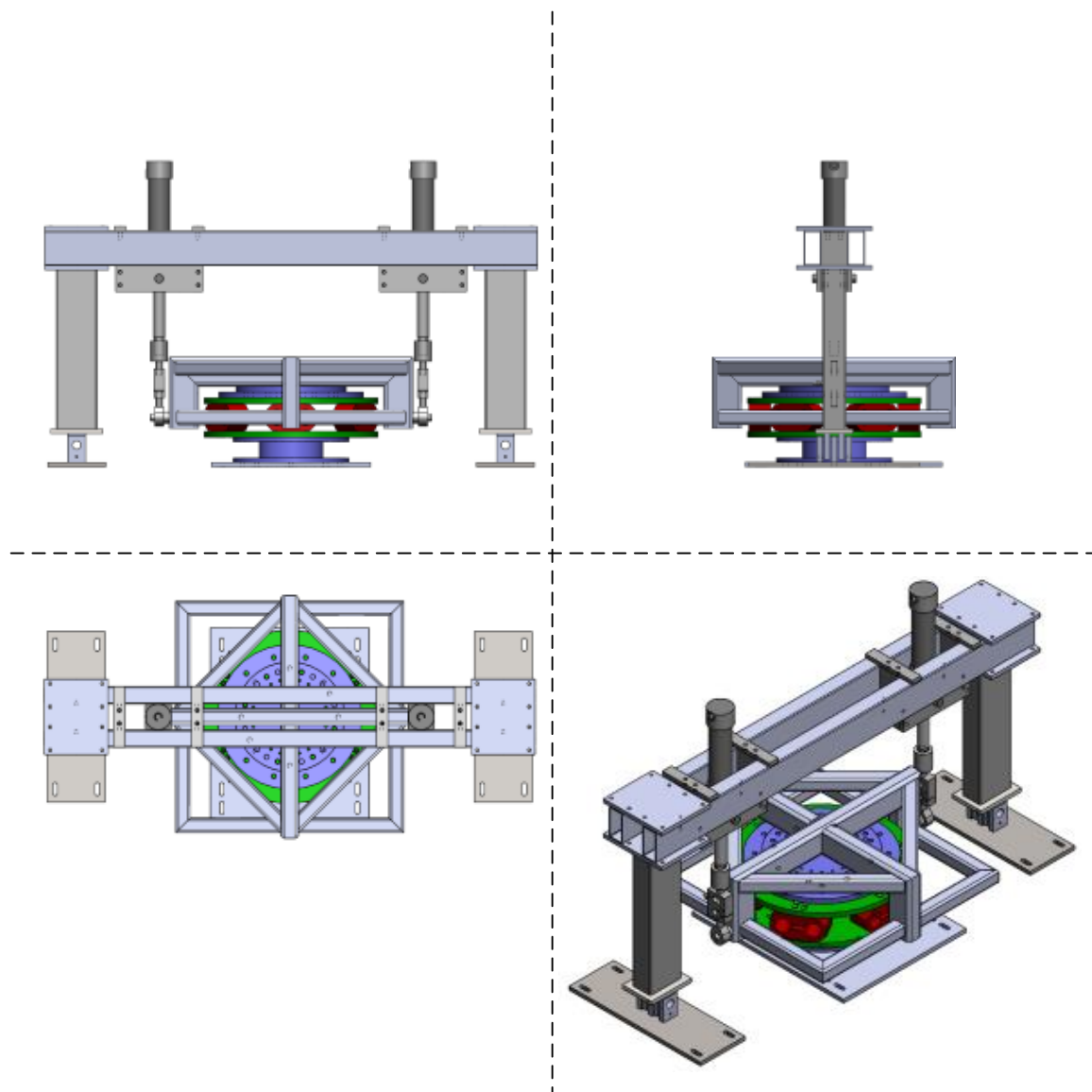
Figure 3.24 The facility for calibration of the whole wheel force sensor

The axis for the input are located in the center of the plot area and are designated by ax_{ref} or ay_{ref} and units *[kN].* The axes referring to the output signal are located on the top and at the left hand side of the plot area. The shape of inputs values creates more or less the circle while the shape created by points of output signal is similar to the ellipse. This is caused by the different stiffness of fatigue body in the direction *x* and *y*. The correction of output signal was calculated by subtracting *10%* of signal *ax* from the output *ay*. For the positive range of *ay* output this mathematical operation improved the location of resultant output points. Whereas for negative range of *ay* output the distance between the real input points and corrected output points is greater as the distance without subtracting the cross-over talk influence.

While the distance between the input and output points for the small value of ax_{ref} input is caused by the greater stiffness of ay transducer, so the distance between those point for small values of ay_{ref} is caused by the cross-over talk. The negative influence of cross-over talk by such a great disproportion could be significantly reduced but it would be necessary more precise and time consuming calibration and data analysis. Because the influence of the correction of output signal was so minimal the correction was not applied in further calculations of resultant wheel forces. The cross-over talk *ax-ay* will cause the fluctuation of forces in the plane *yφ*.

The wheel force sensor was designed to be mounted on the front hub from the test tractor JD 6920S. Its planetary gear box has the shape of cylinder with *280 [mm]* diameter and *150 [mm]* height. The whole wheel force sensor has been at this time already designed. The load rings were mounted in the circle with diameter of *475 [mm]*. So there was enough space inside of measuring hub for electrical wires and the load cells had enough clearance outside too. The facility for calibration of the whole wheel force sensor that is presented in the **Figure 3.24** were manufactured for this particular design. Later on it turned out that the front suspension dedicated to this research came from the tractor JD 7820. The big advantage was that multiple-disc brake were implemented in planetary drive. However the big disadvantage was the fact that the planetary gearbox had *360 [mm]* in diameter and *190 [mm]* of height. The huge difference caused that load rings had to be relocated on greater diameter of *515 [mm]* in order to make a place inside the load cell for planetary drive. At the same the clearance between the outer side of load cells and the inner

diameter of front wheel rim decreased significantly. Under those circumstances the load rings were located on *40 [mm]* greater bolt circle diameter. The carrying plates were reused. Because from inner and outer side were much less space, the load rings were exposed for mechanical damage during mounting and calibration operation. Because inside the calibration frame were too less space for convenient operation and the risk of damage the electrical circuit on the load cells was too high the whole WFTMD were calibrated only in YC direction. The signal of single load ring was equal to one sixth of the applied force. The calculation of all wheel center forces and moments bases on the calibration of every single load ring.
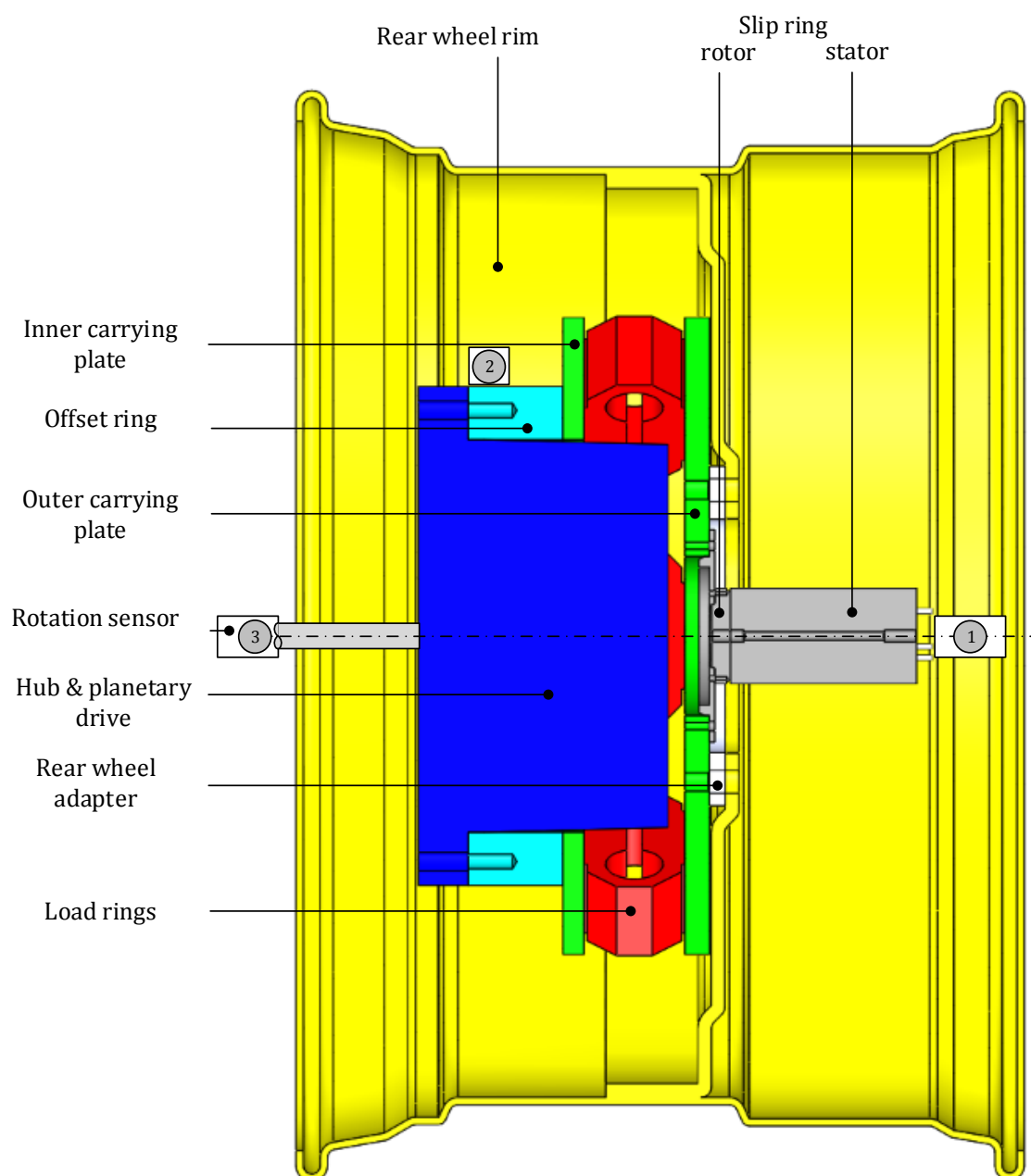

Figure 3.25 The design of Wheel Force & Torque Measurement Device

3.5   Construction of WFTMD

The **Figure 3.25** presents the wheel force and torque measurement device mounted to rear wheel rim. The outer carrying plate has two different bolt circle diameters. In case of mounting the front wheel only the wheel adapter must be changed.

All loads from center tire contact are transferred to the wheel rim and further through outer carrying plate to the force transducers. Four out of six load rings are transformed to the force sensors, see the **Figure 3.12**. All load rings are fixed to the inner carrying plate and further through offset ring to the wheel hub. All electric wires coming out of eight force sensors used for power supply and transferring signals are connected to the rotor of the slip ring G200. The slip ring is mounted from the outer side of the wheel. The electric wires coming out of the stator lead directly to the data acquisition device.

Rotation sensor

In the first solution the magnetic angle sensor was mounted in the position number one, see the **Figure 3.25**. It was able to measure directly the angular wheel position. The pin fixed to the outer carrying plate stacked out of *8 [mm]* diameter hole in the slip ring. The small diameter, relatively long distance and the extensive holder that has to encircle the wheel outside form the fender mounting plate to the center of the wheel plus riding vibration caused that this solution was not stiff enough. The potential risk that this way of mounting the angle sensor will damage the slip rings during the test caused that another solution for measuring angular wheel position were absolutely needed. The inconvenience in mounting this sensor was also a big disadvantage of this solution.

In the second solution the wheel position was measured by incremental encoder together with magnetic band glued to the offset ring. The linear position was calculated to the rotation angle. The fact that the magnetic band was pressed on springy steel band caused that was very difficult to glue the ends of the band to the steel cylindrical surface of the offset ring. Another reason of failure of this solution was quite small range of distance between the sensor head and the magnetic band. The allowed distance from *0.1 [mm]* up to *2 [mm]* turned out far too small in relation to the backlash of the hub carrier and planetary drive in heavy duty application. As a result the sensor head once touched the magnetic band or frequently loosed signal

because the upper limit was exceeded. The magnetic ring with runway and reel would provide the reliably solution eliminating all these failures. However this would increase some additional costs and some rebuilding and manufacturing works would be necessary. This solution has the best practical feature and should be eventually continued.

The third and successfully solution was achieved by mounting the magnetic angle sensor in the place of differential gear, see the **Figure 3.25**. The sensor measured the wheel position multiplied by ratio of planetary gear. This economical solution was resistant for vibration and did not required time consuming redesigning and manufacturing. It was not necessary to demount the sensor during wheel exchange. Some additional work was necessary in order to assign the ratio of planetary drive. The additional work in post-processing and test data evaluation was needed necessary to develop the algorithm that modified the acquainted rotation signal into the signal of real wheel angular position.

Electronic circuit

Because of the need of transferring the signals from rotating into the non-rotary coordinate system the wiring were greatly simplified. Every single full bridge strain gages was connected during calibration by six strands with DAQ device. Two strands were used for supply, two for signal acquisition and two strands for voltage sensing purpose. When the load rings were mounted in the WFTMD four transducers were connected together, so they used ten wires in the slip ring. Two strands were used for supplies that were connected to the voltage sensing wires too. Eight strands were used for transforming signal voltage out of four transducers.

In this way instead of 48 strands only 20 strands were used for acquisition of signals from eight force sensors. Because of upper limit of supply power the excitation voltage were decreased to *1 [V]* and the carrier frequency changed for *4800 [Hz]*. Taking into account that the full scale output equals *50 [kN]* and AD converter works with *24 bits* specification, the system resolution (e.g. the smallest step of force that can be measured) equals *0.6 [g]*. The exact scheme of signal transmission is presented in the appendix A.5.

transducer   slip ring

ax

ay

cx

cy

+   +

-          -

DAQ

ex

ey

fx

fy

+   +

-          -

rotary position
transducer
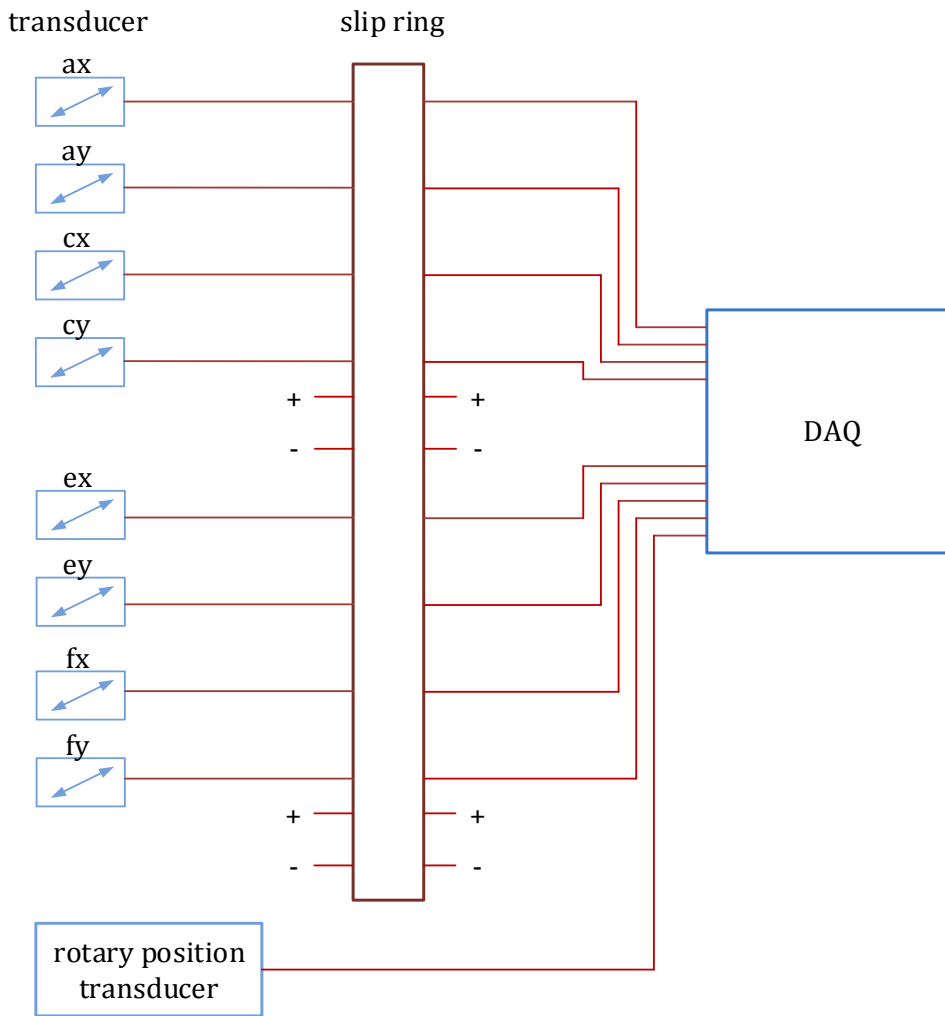
Figure 3.26 Schema of the electric circuit of the WFTMD

WFTMD

Data Acquisition Device
HBM QuantumX XM840a

Measurement notebook
Getac V200

HBM SG   8 full-bridge SGs

D-Sub 15 HD
plug

10 ... 30 V
DC

Ethernet
TCP/IP

Amplifire

ASM POSIROT   Rotary position
transducer

24 bits A/D converter

Sampling rate 200 Hz

AAF   Bessel 20 Hz

Software:
QuantumX Assistant
Catman AP
Matlab
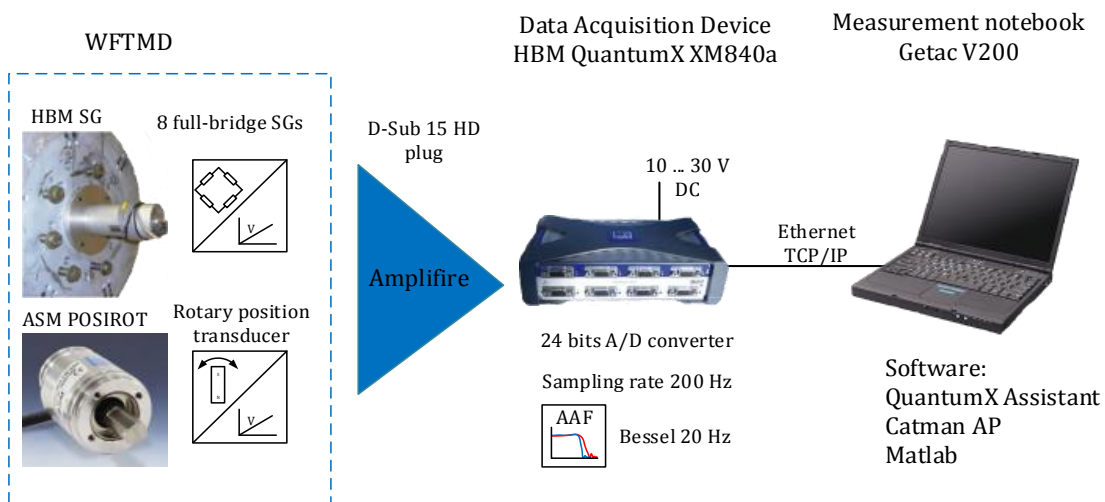
Figure 3.27 The signal flow form sensors to the data analysis software

Processing the test data

The voltage signals coming from force and rotation sensors are acquainted by the QuantumX hardware, see the **Figure 3.27**. The 24 bit A/D converters assure high resolution. The software QuantumX Assistant and Catman AP are dedicated to the setup measurement hardware and prepare test procedure. All digital test data are converted into *.mat file so that the signals can be processed within Matlab software. All operation with signals in the time and frequency domain, application calculation algorithms and graphical presentation of force history are conducted using Matlab.

Chapter 4

4   Analysis and structure of mobile tire test rig

The **m**obile **t**ire **t**est **r**ig enables investigation of mechanical properties of tire and tire-ground characteristics [60]. Further in the text it is designated with its acronym **MTTR**. In general the MTTR enables collecting tire data on various tire sizes, various road surfaces (like: asphalt, concrete, gravel, grass and soil), speeds, pressures, payloads, and slip and camber angles. In order to full fill the goals of this work, detailed described in chapter one, the MTTR guarantees that the tire behaves during test as it would be in real machine during common operation. The functionality is provided by exact kinematic motion of the test wheel.

Figure 4.1 Functionality of Mobile Tire Test Rig

4.1   Functionality

In details the MTTR has six main functions in reference to the test wheel. They are presented graphically in the **Figure 4.1**. The first function defines the way of inducing the payload. The measured tire can be loaded with the certain payload by putting weights on the frame, see the **Figure 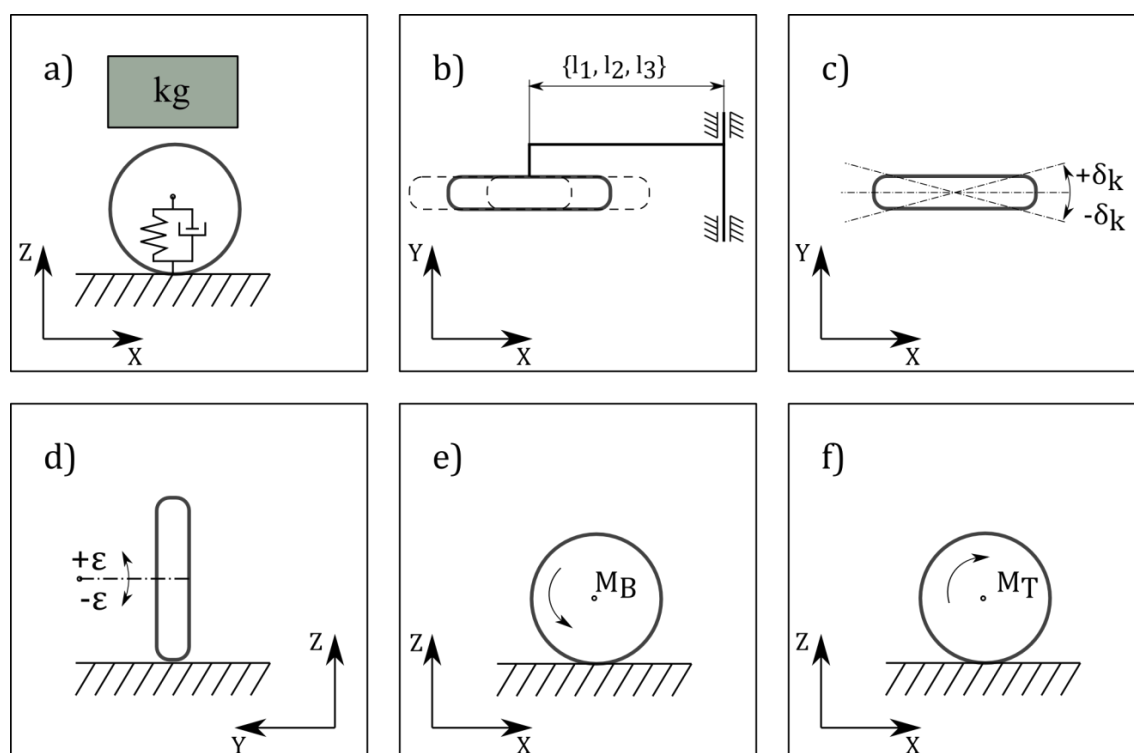4.1, a**. The minimal load is defined by the weight of the MTTR and the wheel itself and equals about *20 000 [N]*. The maximal weight equals 5*0 000 [N]* static load. The second function refers to the free oscillation of the test wheel. The distance between the rotation axis of the test wheel and the rotating axis of the MTTR's frame can be changed in three steps as it is presented in the **Figure 4.1, b** $l_{fr} = \{1520, 1650, 1780\}$. It must be done before mounting the test wheel. During investigation of mechanical properties of the tire in vertical and longitudinal direction it is recommended to keep the big ratio between the vibration amplitude and the distance l_{fr}. It causes that the moment of inertia about frame's rotation axis during the vertical vibration can be easily neglected during data analysis. However in the test of lateral tire properties it is recommended to keep the distance small in order to minimalize the influence of lateral force acting on the test tire on the behavior of the whole vehicle. The third function refers to the kinematical steer angle that can be changed in range of $\delta_k = \{+15°, -15°\}$, see the **Figure 4.1, c**. The positioning is conducted by hydraulic piston and can be changed using control box during the test run. The forth function refers to the camber angle that can be set up by using screw link and must be done before the test. Because of the fact that axle comes from real tractor, changing the steer angle causes the simultaneous change of camber angle, see the **Figure 4.1, d**. In the full range of kinematical steer angle (e.g. ca. *90°*) the camber angle changes about $\pm 15°$. The screw link can be exchanged with hydraulic cylinder. It would make possible to change the camber angle during test run separately from the steer angle. The fifth function refers to the braking moment can be applied in a transient way to the test wheel during the test run, see the **Figure 4.1, e**. The multiple-disc brake is included in the planetary wheel hub. The sixth function that is till now inactive refers to the possibility of application of driving moment to the test wheel, see the **Figure 4.1, f**. This function would enable to conduct the traction tests of certain tire that are crucial in so called performance test influencing the fuel consumption.

4.2   Dynamic analysis

Vertical Model [61, 62]

The plane vertical model of tractor and portable tire test rig is shown in **Figure 4.2**. The tractor alone was loaded in that way that its coupling mass, that determines reciprocal vibratory influence between the front and rear axle, equals around zero [44, 63].
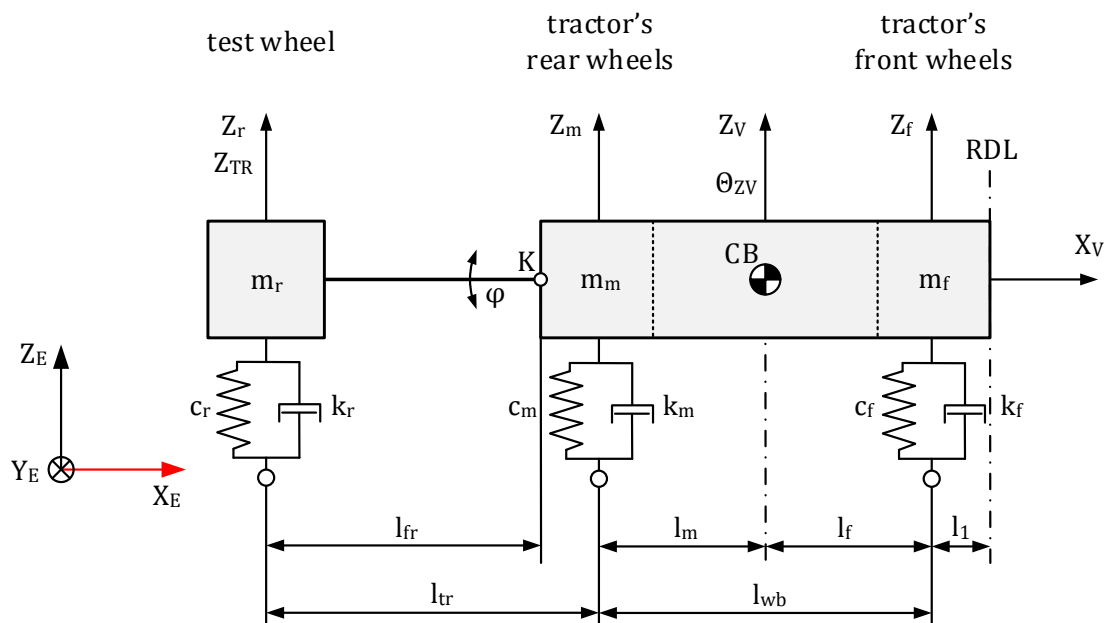
Figure 4.2 Plane vertical model of mobile tire test rig and tractor

Therefore the tractor mass m_t could be decoupled on the mass that lies down directly above the front m_f and the rear axle m_r. The whole MTTR is also balanced in such a way that its whole mass lies nearly above the rotation axis of test wheel Y_{TR}. It does not change significantly the tractor's front and rear axle load. This is physical model of quarter vehicle that is presented as the rigid body over the tire shown as a spring-damper element. This creates the solution idea for aims and approach of this research. It is coupled to the tractor's body by the massless link. With those boundary conditions it can be presumed that the test wheel behaves as linear one mass-oscillator. Excited by the road unevenness rotates in reference to the tractor around the point *K*, see the **Figure 4.2**. Those assumptions are crucial for further data analysis and enable to measure vertical stiffness and damping ratio of the tire with stochastic excitation. It also enables the test by free oscillations for bigger excitation. The tire mechanical parameters can be measured for different slips and different slip angles. The braking moment and the kinematic steer angle can be

varied during the test and so the transient behavior can be reproduced. More information about method of data analysis is presented in the chapter five.

Because the lateral and vertical position of the center of the mass is neglected in this model and the whole analysis in this research, instead of the term: center of gravity *CG* is used the term: center of balance *CB*. The presented procedure for balance computation is used by shipping agency [64]. The payload is measured with *5 [kg]* resolution and all distances are rounded in the usual manner to the whole *50 [mm]*. In case of multi-axle vehicles first is measured distance from a reference datum line (RDL) to the every axle. Every distance is multiplied by weight of the axle, and then the sum of moments is divided by gross weight. The resulting figure is the number of millimeters to be measured from the reference line to the CB of the vehicle:

$$\frac{l_1 \cdot m_f + (l_1 + l_{wb}) \cdot m_m + (l_1 + l_{wb} + l_{tr}) \cdot m_r}{m_f + m_m + m_r} = l_1 + l_f \qquad [4.1]$$

The meaning of all symbols shown in the **Figure 4.2** and **Figure 4.3** and their values are listed in the table 4.1.

Table 4.1 The parameters of vertical and horizontal model of tractor and MTTR

Symbol	Meaning	Values	
l_1	distance from RDL to the front axle	0.4 m	
l_{wb}	the wheel base	2.6 m	
l_{tr}	distance between tractor's rear axle and the rotation axis of the test wheel	2.8 m	
l_{fr}	distance between the rotation axis of the test wheel and the rotating axis of the MTTR's frame	1.65 m	
The parameters regarding the test wheel		Front	Rear
m_f	tractor's front payload	4145 kg	4145 kg
m_m	tractor's rear payload	3830 kg	3830 kg
m_r	test wheel payload	2710 kg	3300 kg
l_f	distance from the front axle to the CB	2.3 m	2.45 m
l_m	distance from the rear tractor's axle to the CB	0.3 m	0.15 m
l_r	distance from the test wheel to the CB	3.1 m	2.95 m
Θ_{ZV}	moment of inertia around vehicle vertical axis	17500 kg·m²	19500 kg·m²

Horizontal Model [65–68]

The linear single track model of vehicle as shown in the **Figure 4.3** was used to analyze lateral dynamics of the tractor with coupled mobile tire test rig during the test runs. The solution idea for the goals defined in this research that is quarter-vehicle coupled behind the tractor is checked for its reasonability. Wheels of front

and rear tractor's axle are reduced to one wheel in the middle. The test wheel which is situated on the longitudinal axis behind the tractor is represented also through one wheel. With the assumption that the velocity is constant and the center of gravity lays on the track there are only two degrees of freedom: yaw and lateral movements. There are no roll movements. The geometry parameters and the gross mass relates to the John Deere 6920S tractor. The mass of frame with rear test wheel equals *3300 [kg].* Its local center of gravity lies over the rotation axis of the measuring wheel. The mass of inertia around the vertical axis for the tractor and the mobile tire test rig is estimated as *19500 [kg·m²].* The aim of this analysis is to answer the question: "How the tractor with mobile TTR will behave when rear test wheel will be turned for certain one angle by certain velocity?"
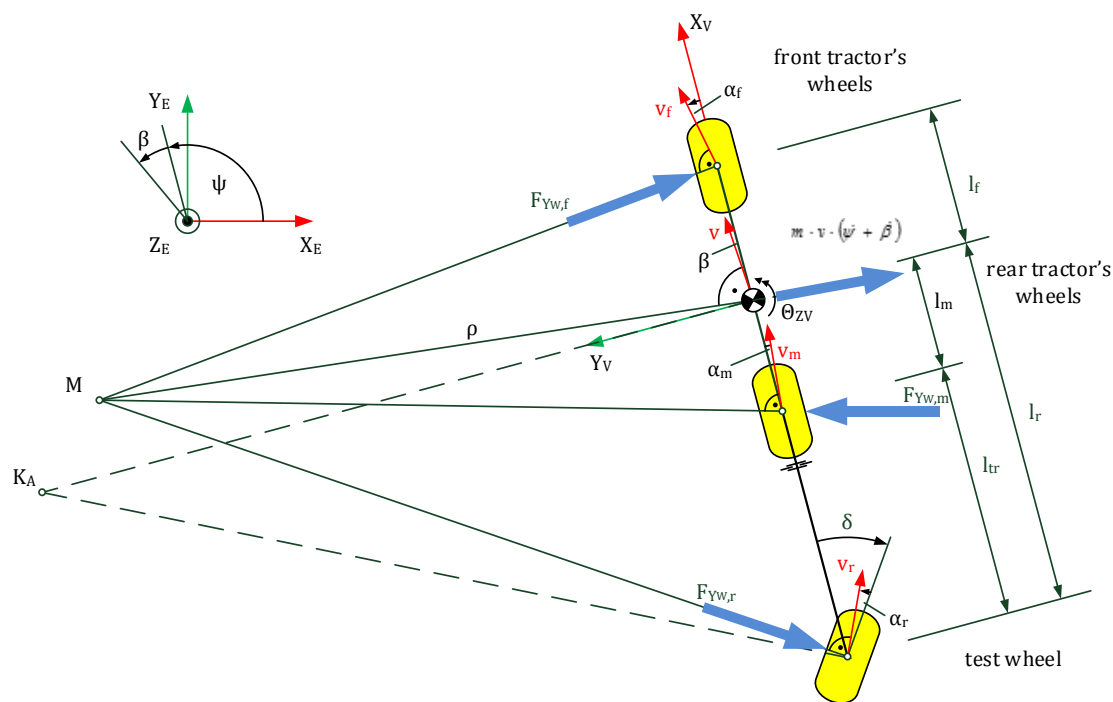

Figure 4.3 Single track of mobile tire test rig and tractor

The centripetal acceleration equals

$$\frac{v^2}{\rho} = v(\dot{\psi} + \dot{\beta})$$ [4.2]

The velocity of center of balance equals

$$\vec{v} = \begin{bmatrix} v_{X_V} \\ v_{Y_V} \\ v_{Z_V} \end{bmatrix} = \begin{bmatrix} v \cdot \cos(\beta) \\ v \cdot \sin(\beta) \\ 0 \end{bmatrix}$$ [4.3]

The acceleration of center of balance equals $a = v(\dot{\psi} + \dot{\beta})$, so its components equal

$$\vec{a} = \begin{bmatrix} a_{X_V} \\ a_{Y_V} \\ a_{Z_V} \end{bmatrix} = \begin{bmatrix} -v \cdot (\dot{\psi} + \dot{\beta}) \cdot \sin(\beta) \\ v \cdot (\dot{\psi} + \dot{\beta}) \cdot \cos(\beta) \\ 0 \end{bmatrix}$$ [4.4]

It can be noticed that the velocity of each wheel is connected to the velocity of vehicle by its geometry. The slip angle for each wheel can be calculated by compering those velocities for each component *x, y, z* and assuming that it all happens for small angles:

front
wheel
$$\vec{v_f} = \begin{bmatrix} v \cdot \cos(\beta) \\ v \cdot \sin(\beta) + l_f \cdot \dot{\psi} \\ 0 \end{bmatrix} = \begin{bmatrix} v_f \cdot \cos(\alpha_f) \\ v_f \cdot \sin(\alpha_f) \\ 0 \end{bmatrix}$$

$$\rightarrow \tan(\alpha_f) = \frac{v \cdot \sin(\beta) + l_f \cdot \dot{\psi}}{v \cdot \cos(\beta)}$$ [4.5]

$$\alpha_f = \beta + l_f \cdot \frac{\dot{\psi}}{v}$$

middle
wheel
$$\vec{v_m} = \begin{bmatrix} v \cdot \cos(\beta) \\ v \cdot \sin(\beta) - l_m \cdot \dot{\psi} \\ 0 \end{bmatrix} = \begin{bmatrix} v_m \cdot \cos(\alpha_m) \\ -v_m \cdot \sin(\alpha_m) \\ 0 \end{bmatrix}$$

$$\rightarrow \tan(\alpha_m) = -\frac{v \cdot \sin(\beta) + l_m \cdot \dot{\psi}}{v \cdot \cos(\beta)}$$ [4.6]

$$\alpha_m = -\beta + l_m \cdot \frac{\dot{\psi}}{v}$$

rear
wheel
$$\vec{v_r} = \begin{bmatrix} v \cdot \cos(\beta) \\ v \cdot \sin(\beta) - l_r \cdot \dot{\psi} \\ 0 \end{bmatrix} = \begin{bmatrix} v_r \cdot \cos(\delta - \alpha_r) \\ -v_r \cdot \sin(\delta - \alpha_r) \\ 0 \end{bmatrix}$$

$$\rightarrow \tan(\delta - \alpha_r) = \frac{v \cdot \sin(\beta) + l_r \cdot \dot{\psi}}{v \cdot \cos(\beta)}$$ [4.7]

$$\alpha_r = \delta + \beta - l_r \cdot \frac{\dot{\psi}}{v}$$

The relation between the wheel slip angle and the lateral forces is linearized

$$\begin{aligned} F_{Y_W,f} &= c_{\alpha f} \cdot \alpha_f \\ F_{Y_W,m} &= c_{\alpha m} \cdot \alpha_m \\ F_{Y_W,r} &= c_{\alpha r} \cdot \alpha_r \end{aligned}$$ [4.8]

The system of two equations of motion of the single track model is necessary to analyze the vehicle dynamics of MTTR and the tractor. First equation is driven from

moments around the center of balance. The moment of inertia around vehicle vertical axis is designated with capital Greek letter 'theta' without any index θ:

$$\theta\ddot{\psi} = -c_{\alpha f} \cdot \alpha_f \cdot l_f - c_{\alpha m} \cdot \alpha_m \cdot l_m + c_{\alpha r} \cdot \alpha_r \cdot \cos(\delta) \cdot l_r \qquad [4.9]$$

The projection of forces on axis y_V yields the second equation:

$$m \cdot v(\dot{\psi} + \dot{\beta}) \cdot \cos(\beta) = -c_{\alpha f} \cdot \alpha_f + c_{\alpha m} \cdot \alpha_m + c_{\alpha r} \cdot \alpha_r \qquad [4.10]$$

Notations:

$\dot{\psi}$ – yaw velocity;

β – body side slip angle;

δ – steer angle of the test wheel;

$\alpha_f, \alpha_m, \alpha_r$ – wheel slip angle of front, middle and rear wheel;

$c_{\alpha f}, c_{\alpha m}, c_{\alpha r}$ – cornering stiffness of front, middle and rear wheel.

Thanks of assumption that this model describes the vehicle dynamic only within linear range e.g. for small angles, the equations [4.9] and [4.10] can be linearized as follows:

$$\begin{cases} \theta\ddot{\psi} = -c_{\alpha f} \cdot \alpha_f \cdot l_f - c_{\alpha m} \cdot \alpha_m \cdot l_m + c_{\alpha r} \cdot \alpha_r \cdot l_r \\ m \cdot v(\dot{\psi} + \dot{\beta}) = -c_{\alpha f} \cdot \alpha_f + c_{\alpha m} \cdot \alpha_m + c_{\alpha r} \cdot \alpha_r \end{cases} \qquad [4.11]$$

After substituting the particular wheel slip angles from equation [4.5-4.7], the system of equation of motion [4.11] can be easily modified into the state matrix of state space representation:

$$\begin{aligned} \dot{x} &= A \cdot x + B \cdot u \\ y &= C \cdot x + D \cdot u \end{aligned} \qquad [4.12]$$

The input vector u represents the steer angle δ. The state variables are the yaw rate $x_1 = \dot{\psi}$ and the side slip angle $x_2 = \beta$. The state equation of the linearized single track model for multi-axle vehicle with rear steering looks as follows:

$$\begin{bmatrix} \ddot{\psi} \\ \dot{\beta} \end{bmatrix} = \begin{bmatrix} \dfrac{-c_{\alpha f} \cdot l_f{}^2 - c_{\alpha m} \cdot l_m{}^2 - c_{\alpha r} \cdot l_r{}^2}{\theta \cdot v} & \dfrac{-c_{\alpha f} \cdot l_f + c_{\alpha m} \cdot l_m + c_{\alpha r} \cdot l_r}{\theta} \\ \dfrac{-m \cdot v^2 - c_{\alpha f} \cdot l_f - c_{\alpha m} \cdot l_m - c_{\alpha r} \cdot l_r}{m \cdot v^2} & \dfrac{-c_{\alpha f} - c_{\alpha m} - c_{\alpha r}}{m \cdot v} \end{bmatrix} \cdot \begin{bmatrix} \dot{\psi} \\ \beta \end{bmatrix} + \begin{bmatrix} \dfrac{c_{\alpha r} \cdot l_r}{\theta} \\ \dfrac{-c_{\alpha r}}{m \cdot v} \end{bmatrix} \cdot \delta \qquad [4.13]$$

$$
\begin{bmatrix} \dot{\psi} \\ \beta \\ F_{Y_{W,f}} \\ F_{Y_{W,m}} \\ F_{Y_{W,r}} \end{bmatrix} = \begin{bmatrix} 1 & 0 \\ 0 & 1 \\ \dfrac{c_{\alpha f} \cdot l_f}{v} & c_{\alpha f} \\ \dfrac{c_{\alpha m} \cdot l_m}{v} & c_{\alpha m} \\ \dfrac{-c_{\alpha r} \cdot l_r}{v} & c_{\alpha r} \end{bmatrix} \cdot \begin{bmatrix} \dot{\psi} \\ \beta \end{bmatrix} + \begin{bmatrix} 0 \\ 0 \\ 0 \\ 0 \\ c_{\alpha r} \end{bmatrix} \cdot \delta
$$

All elements of state matrix A (see **Equation 4.13)** with input steer angle $\delta = 5°$ and the velocity $v = \{10, 20, 30, 40\}\,[km/h]$ with parameter shown in the table 4.1 e.g. with front and the rear tire as the test wheel are negative.

These parameters represent poles of continuous-time state-space model of single track model. In other words the poles of the system are roots of the denominator polynomial. The fact that they are negative is the evidence that the system is stable. This is very important because the two-axle vehicles with rear steering are usually unstable. The introduction of fixed third axle changes positively the system. The test of sensibility of parameters shows that as the center of balance moves towards the front axle the system becomes unstable.
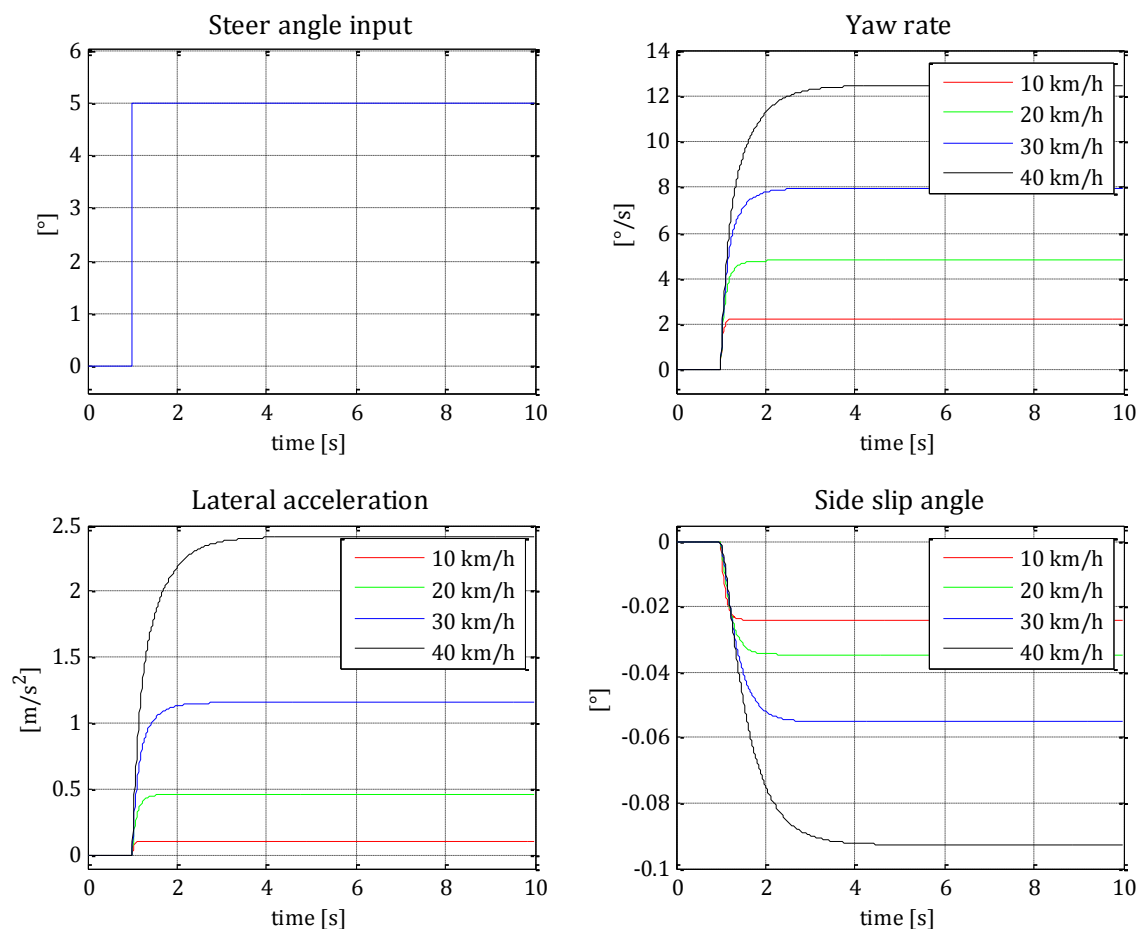
Figure 4.4 The kinematic results step response of single track model

The **Figure 4.4** presents the step response of continuous-time state-space single track model. The input signal is step steer angle of value *5[°]*. The yaw velocity achieves steady-state value without overshoot. It means that the system is over-damped. The lateral acceleration is under *4 [m/s²]* that means that the assumption of linearity of the single track model is valid. The negative side slip angle depict that the velocity vector points to the right side of vehicle while the whole vehicle is rotating in counter-clockwise direction. The point *M* on the **Figure 4.3**, around that rotates the vehicle body should be moved in front of the center of balance towards the front axle.
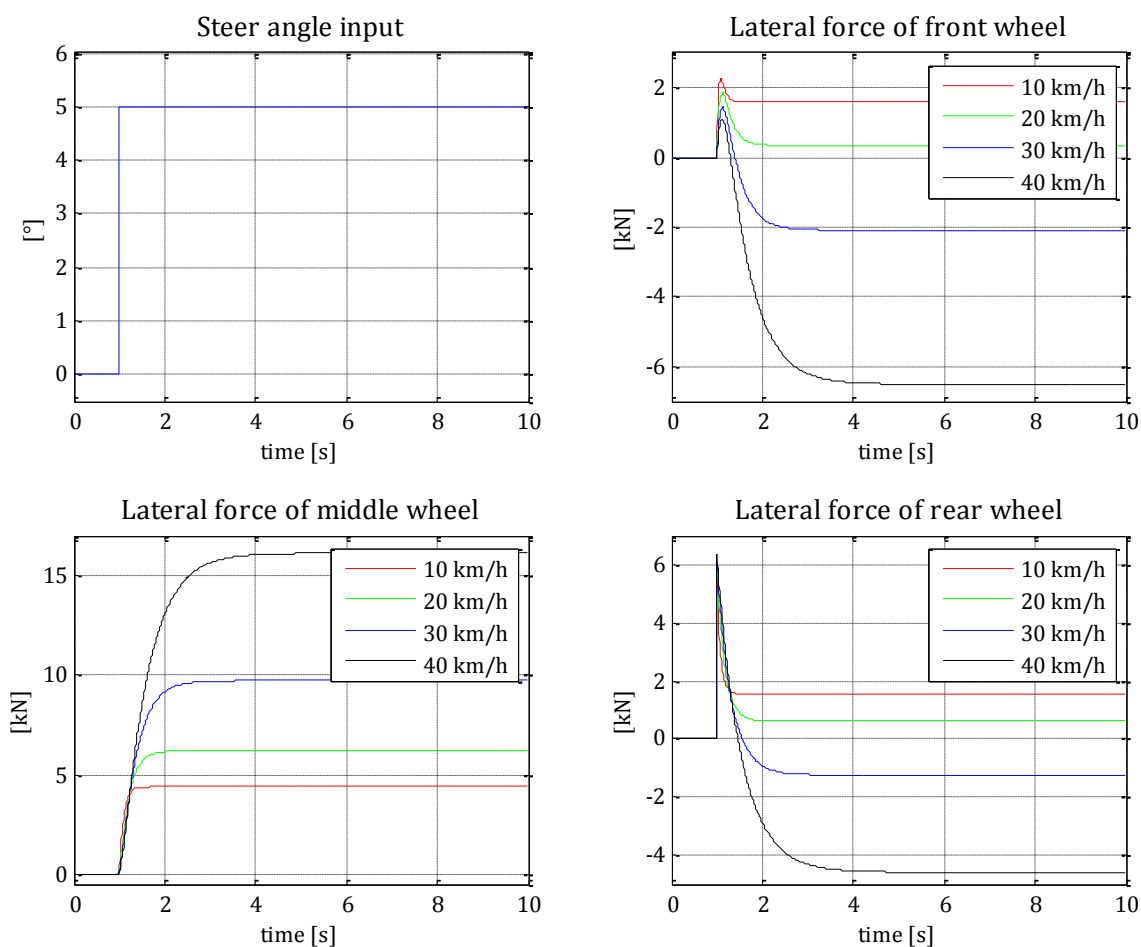
Figure 4.5 The kinetic results step response of single track model

The **Figure 4.5** presents the lateral force response acting on the front, middle and real wheel of the single track model on the steer angle input. The forces of front tire for velocity of *10* and *20 [km/h]* have little overshoot and stay in positive range. That means that they act in direction as shown on the **Figure 4.3**. For velocity of *30* and *40 [km/h]* the state value stays negative. The force of middle wheel e.g. the rear tractor's wheels is positive and its magnitude rises with the velocity. The force

acting on the rear wheel behaves similar as in case of front wheel force. The rear lateral force for velocity of *10* and *20 [km/h]* is positive and for *30* and *40 [km/h]* becomes negative. The force gained by multiplying the lateral acceleration *ay* by gross weight of vehicle is equal to the resulting lateral wheel force. This indicates in some range the propriety of the model.

Stability and controllability of three-axle rear steering vehicle [32, 68]

The two-axle vehicles are stable independently if the front or rear axle is steered. After achieving the peak value of side steering forces the front wheel steered vehicles become first unstable but still controllable, whereas the rear wheel steered vehicles become, irrespective from caster angle, both unstable and uncontrollable. The tractor with mobile tire test rig during test rides becomes three-axle rear steering vehicle. Because the front and middle wheels are fixed, they produce aligning torque what makes the vehicle stable. Eventually rear wheel skid is still recoverable.

However the three-axle rear wheel steering vehicle has some peculiarities in common with two-axle rear steering vehicles. After achieving certain velocity, during the transition from straight to curvilinear driving, the side forces act on the steered wheels first outwards and then inwards, see **Figure 4.5**. The direction of the steered side forces alter in dependence on the situation. They act always outwards during begin of cornering and initial rotation about centre of gravity. The side forces always act inwards during going out of the curve. In steady-state driving in a bend the direction of side forces depends on velocity, see **Figure 4.5**. Because of the positive caster angle the outward side steering forces induce self-aligning torque that counteracts steering wheel deviations. If the side forces act inwards the steering system amplifies the steering wheel deviations. This phenome is minimalized by hydraulic steering system, see **Figure 4.8**. The nature of this vehicle can be changed by altering the geometry, the location of COG or cornering stiffness.

4.3   Structure

The mobile tire test rig is the practical realization of solution idea that is quarter-vehicle. The whole frame of MTTR within WFTMD is presented as 3D model in the **Figure 4.6**. It consists of six main sections designated on the figure by rectangular label with their names and yellow filling. The 'tractor' section serves to attach the

whole TTR to the tractor's three point hitch. This is only one section that does not oscillate during the test. It is connected to the rest of the TTR's frame by the pivoting axle. The 'front' and the 'left' section transfer the main loads from the test wheel to the tractor. The 'right' and 'upper' section are built out of smaller profiles than 'front' and 'left' section. They together with rear plate reinforce the frame and enhance its stiffness. The weights can by mounted on the 'right' and the 'left' section, see the **Figure 4.6**.
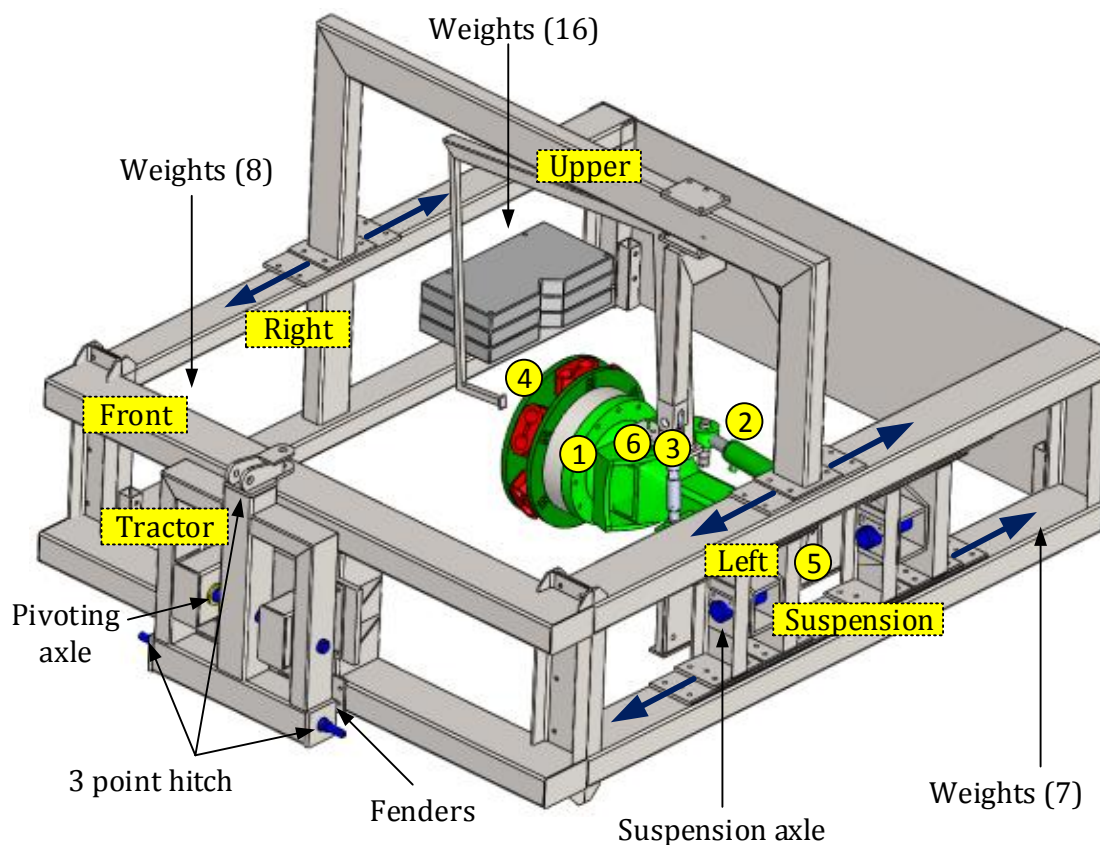
Figure 4.6 The structure of mobile tire test rig

However because bigger and heavier profiles of the 'left' section and the 'suspension' section the left side is much heavier than the right side of the frame. The frame of the test rig is loaded in such a way that the local center of gravity lies as close as possible the wheel rotation axis Y_C. This is crucial condition that must be full field in order the assumption of one mass oscillator and the presented evaluation method of signal will be valid. In order to change the distance from test wheel to the pivoting axle l_{fr} (see the **Figure 4.2**) the whole 'suspension' and 'upper' section must be moved stepwise into the right position. Special fenders are mounted to the 'tractors' section beneath the pivoting axle. During the test the tractor section is lowered, the TTR

frame rest first on the test wheel and between the fenders and front section appears a gap. The gap enables free oscillation of the frame in reference to the tractor. Sometimes hydraulic upper linkage must be extended in order to increase the gap. Inversely as the 'tractor' section is uplifted by the three point hitch, the fenders contact the 'front' section beneath the pivoting axle and the whole ttr goes up as the ordinary operating tools. So the tractor can easily turned back during the test or just drive to the test track.

Table 4.2 Actuators and sensors

Type	Function
Actuators	
1 - multiple-disc brake	braking moment
2 - steer angle cylinder	kinematical steer angle
3 - camber screw link	camber angle
Sensors	
4 - WFTMD	forces and moments in the wheel center
5 - rotary position transducer	rotational position of the measuring hub
6 - 1D accelerometer	vertical Z_{TR} acceleration of the test rig
7 - laser sensor	dynamic radius of the test wheel
8 - distance sensor	kinematical steer angle
9 - pressure sensor	input for braking moment
10 - longitudinal velocity sensor	longitudinal velocity of the vehicle
11 - lateral velocity sensor	lateral velocity of the vehicle
12 – slip body angle transducer	slip body of the vehicle

Three actuators and ten sensors are installed in the tire test rig. They are listed in the **Table 4.2**. The position of all actuators is pointed also in the **Figure 4.6**. The multiple-disc brake, see no. 1, are installed in the planetary gear of the wheel hub. The test wheel and measuring hub are mounted to an original tractor steering knuckle which is attached to the axle body. A hydraulic cylinder, see no. 2, which can control the kinematical steer angle, is mounted between the steering knuckle and plate. Due to the fact that the suspension has been taken from a real tractor, every change of the steer angle involves a change of camber angle. The axle body is fixed to a plate which can rotate around its longitudinal suspension axle, see **Figure 4.6**. The whole suspension assembly is supported by a camber screw linkage, see no. 3. By screwing this linkage the whole wheel suspension inclusive the hydraulic cylinder for steering angle rotates around the longitudinal suspension axle so the inclination of symmetry plane of the test wheel changes in relation to the frame. In this way the camber angle of the tire can be set for desired value.

Three sensors only that are installed in the TTR are pointed in the **Figure 4.6**. The WFTMD, see no. 4, described in chapter 3 enables measurement of forces and torques in the center of the wheel. It is mounted between the original hub and wheel rim. The actual angular wheel's position is detected by rotary position transducer, see no. 5. As it was mentioned in the previous chapter the final position is the third one, see also **Figure 3.25**. Because of the fact that this sensor measures practically the rotation of the driving shaft (see **Figure 4.6)** the ratio of planetary gear must be considered in order to determine the real wheel position. The algorithm for this signal operation is introduced in the appendix B. The accelerometer is mounted to the steering knuckle. It is always leveled as the load of whole frame lies on the test wheel so the active axis is parallel to the vertical axis of the wheel Z_C. The accelerometer measures vibration of the free oscillating mass and is one of the most important sensor in this method.

Figure 4.7 The photo of the tractor and mobile tire test rig - top, the Joystick – bottom left; the gap between the 'tractor' and 'front' section- bottom middle; the wheel suspension – bottom right

The laser sensor is used to measures the dynamic radius of the tire (see **Figure 4.7** bottom right). A distance sensor is used to measure the stroke length of the hydraulic cylinder used for controlling the steer angle of the test wheel (see

Figure 4.7 bottom right). The braking system contains a pressure control valve and pressure sensor in order to reduce and control the braking pressure (see **Figure 4.7** bottom right). The longitudinal, lateral velocity and the slip body angle transducer are used to trace the vehicle trajectory during the test. The frame of TTR can freely oscillate around the lateral pivoting axle, angle φ on **Figure 4.2**. The test wheel is mounted into a frame of TTR which is pulled behind the tractor. The tire represents the spring-damper element and together with the frame and its weight, represents a single-mass oscillator.
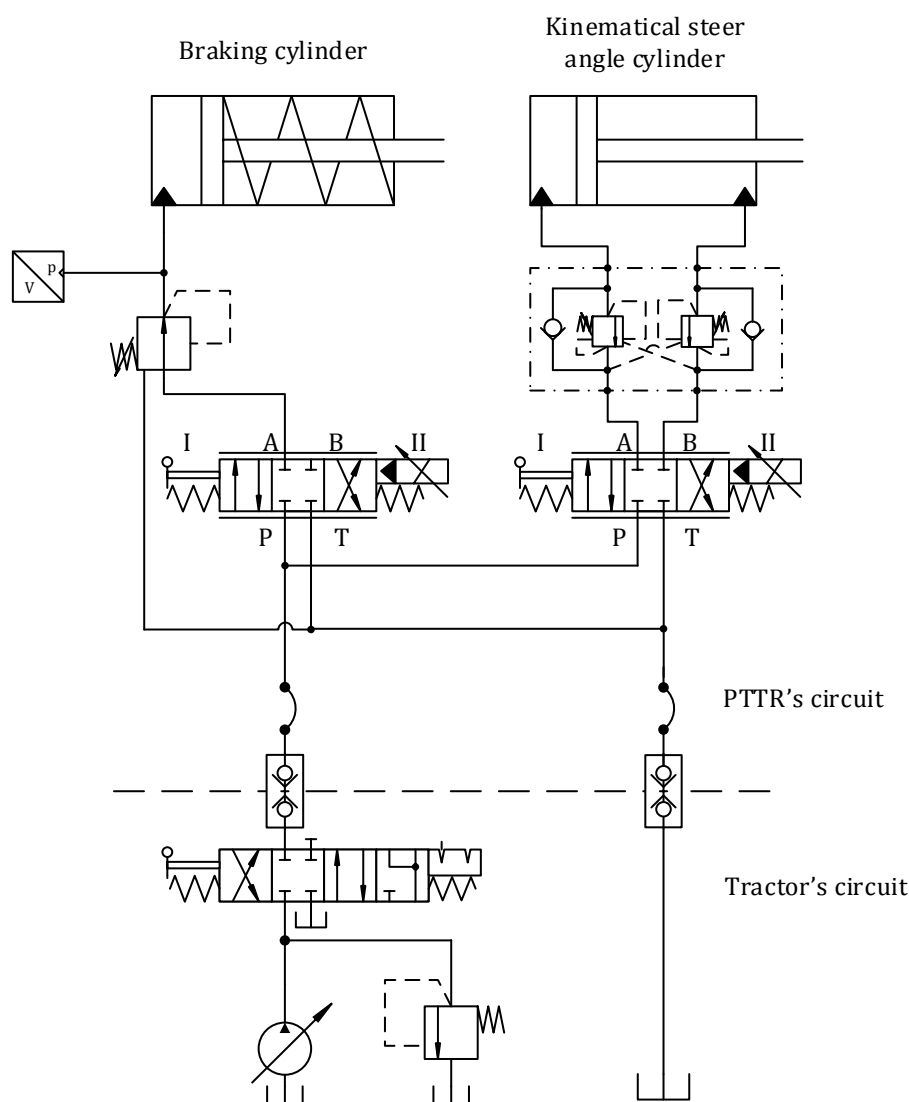
Figure 4.8 The hydraulic circuit of mobile tire test rig

The hydraulic circuit of TTR is connected to the tractor's hydraulic system (see **Figure 4.8**). The return pipe line is connected to the pressureless inlet. The supply line can by switch on by the manually operated 4/4 valve with detent, which is

located on the operator panel in the tractor's cabin. The two actuators of braking and steer angle subsystem are operated by the proportional 3/4 valve with electric linear actuator. The PVG 32 valve from SauerDanfoss has lever and hydraulic pilot pressure for electric operation.

The braking actuator is single-acting differential cylinder with spring on the rod side. The supply line has pressure reducing valve with drain in order to limit the operating pressure up to *75%* of nominal pressure which is *33* bar. The pressure transducer is used to monitor braking pressure. Eventually pressure peaks can damage of braking piston. The kinematical steer angle actuator is double-acting differential cylinder (78/45/130). The valve for controlling the lowering brake is installed with the steel pipes directly on the cylinder. The function of this valve is to prevent from uncontrolled wheel turn in case of damage of the supplying pipe or failure of the hydraulic system. Further the valves are connected to the 3/4 valve by the elastic pipe. The proportional valve PVG 32 is operated from the control panel installed in the tractor's cabin on the right hand side of the driver. By operating the joystick the test wheel can by simultaneously braked and turned left or right. Because the valve is closed in the middle position the residual pressure can be relieved by connecting the pressure line with the oil reservoir. Thanks to APEM robust and industrial potentiometer joystick all operation can be carried out smoothly.
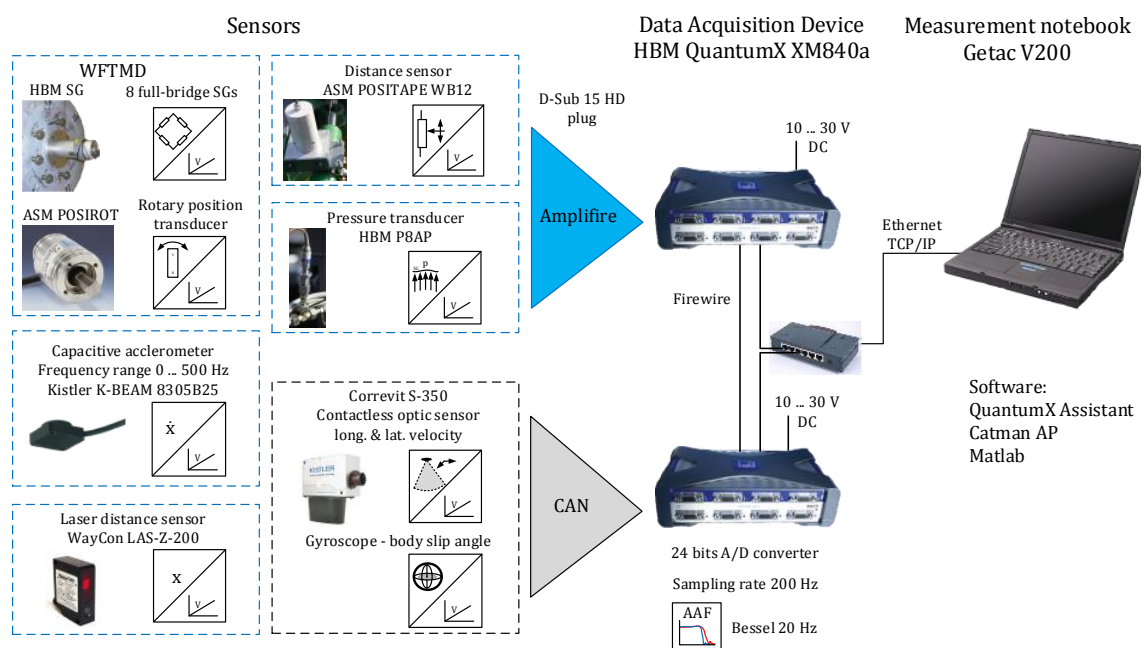
Figure 4.9 The measurement chain of mobile tire test rig

4.3.1   Measurement chain

The structure of measurement system is presented on the **Figure 4.9.** The most sensors provide voltage output proportional to their signal. Only the velocity and body slip sensors provide digital output signal through CAN interface. All sensors are contacted into QuantumX XM840a data acquisition device manufactured by HBM enterprise. Every single sensor is connected to two synchronized DAQ instruments QuantumX 840 manufactured by HBM. The voltage signals are first amplified by certain factor. Then, they are filtered by Bessel low-pass Anti-Aliasing Filter (AAF) with *20 [Hz]* corner frequency for *-3dB*. All analog signals are digitalized with *200 [Hz]* sampling rate and 24-bit resolution. Two DAQs are connected with each other by the fire wire cable in order to synchronize the measurement. Further the digital signals' histories are send by the Ethernet cable the measurement notebook. The digital signal processing and graphical interpretation are conducted by the software as Catman AP and Matlab.

Chapter 5

5 Method of tire test and data evaluation

The methods of tire testing used in this research and evaluation of measurement data are described in this chapter. The necessary theory needed to estimate stiffness and damping ratio of tire in vertical direction by two methods is introduced at the beginning. Next the background of necessarily operations made during signal analysis is explained. The explanation is supported by already identified and proved nature of tire and road characteristics. The third test called: step response of lateral force shows how the lateral force is being build up in dependence on wheel slip angle. The tire is exposed in this test in transient way that is one of the most important tasks in this research. The tire – ground characteristic is result of this test. The aim of this test is to prove the functionality of WFTMD too.

All tests were conducted on the test ground of TÜV Rheinland in Cologne. The asphalt lane is about *3 [m]* width and *170 [m]* long. All tests were started from the same point and driven in the same direction as shown in the **Figure 5.1**. The inclination is about *0* degrees through the whole length. The test lane has three visible asphalt joints and accompanying them unevenness. It has significant and negative influence on tests inducing strong step excitations. The last *30 [m]* long section is dominated by high unevenness and it is not suitable for any test.
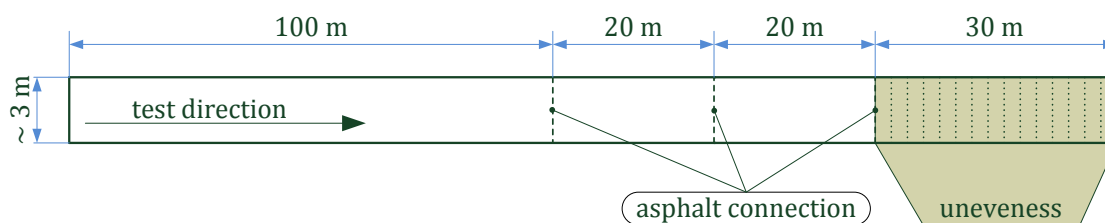
Figure 5.1 Dimensions of test road and its defects

5.1 Tire properties in vertical direction

The vertical stiffness and damping ratio of tire are investigated by two methods: test by free oscillations and test of random vibrations. These two methods should emphasize the nonlinear character of the tire.

5.1.1 The elementary theory about single dof mass oscillator

The calculation of vertical stiffness and damping ratio bases on the fact that the test tire is represented by the spring – damper element loaded by the mass of its payload. In other words the MTTR is damped free, single – degree – of – freedom, vibration mechanical system, shown in the **Figure 5.2**. The system is base excited by road unevenness (input coordinate z_{CTC}). The boundary conditions as payload, tire inflation pressure, velocity, steering and camber angle within one test run are constant. Therefore the tire is considered as a linear time invariant (LTI) system. The acceleration signal $\ddot{z}_r$ represents the vibratory output of the system. It is used for determination of vertical tire properties within two methods.
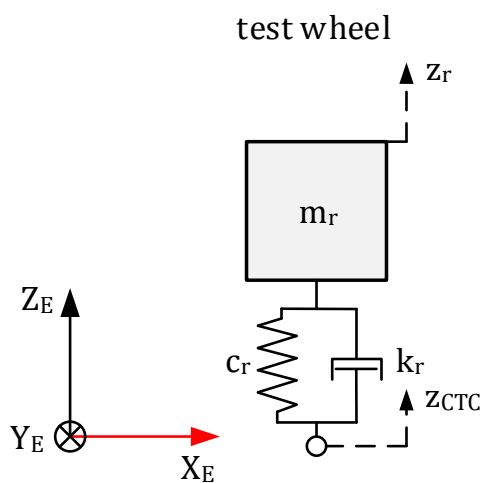
Figure 5.2 Damped linear one–degree–of–freedom mechanical system

The linear differential equation describing the motion of the damped free vibration single dof LTI mechanical system equals

$$m\ddot{z}_r + c\dot{z}_r + kz_r = 0 \qquad [5.1]$$

The stiffness k and viscous damping constant c are those of interest. The mass m is known. Dividing the equation [5.1] by the mass, yields

$$\ddot{z}_r + \frac{c}{m}\dot{z}_r + \frac{k}{m}z_r = 0 \qquad [5.2]$$

If *natural circular frequency* of undamped oscillator

$$\omega_0{}^2 = \frac{k}{m} \qquad\qquad [5.3]$$

and decay rate

$$\delta = \frac{c}{2m} \qquad\qquad [5.4]$$

Is set into the equation [5.2], it becomes:

$$\ddot{z}_r + 2\delta\dot{z}_r + \omega_0{}^2 z_r = 0 \qquad\qquad [5.5]$$

The mathematical relation between frequency, circular frequency and oscillation period are presented below:

$$f = \frac{1}{T} = \frac{\omega}{2\pi}\ [Hz] \qquad T = \frac{2\pi}{\omega}\ [s] \qquad \omega = 2\pi f\ \left[\frac{rad}{s}\right] \qquad [5.6]$$

Assuming a solution $x(t) = Be^{\lambda t}$ for linear homogeneous differential equation [5.5] leads to the *characteristic equation*

$$\lambda^2 + \lambda 2\delta + \omega_0{}^2 = 0 \qquad\qquad [5.7]$$

or using the description of motion from equation [5.1][69]

$$\lambda^2 m + \lambda c + k = 0 \qquad\qquad [5.8]$$

The roots for equation [5.7] are

$$\lambda_{1/2} = -\delta \pm \sqrt{\delta^2 - \omega_0{}^2} \qquad\qquad [5.9]$$

Or for equation [5.8]

$$\lambda_{1/2} = -\frac{c}{2m} \pm \sqrt{\left(\frac{c}{2m}\right)^2 - \frac{k}{m}} \qquad\qquad [5.10]$$

There are three different solutions in dependence on radicand

$$\delta^2 - \omega_0{}^2 \qquad\qquad [5.11]$$

Mathematically the radicand [5.11] can be smaller, equal or bigger than zero. In order to distinguish those three cases and to define the influence of damping can be introduced dimensionless *damping ratio*

$$\xi = \frac{\delta}{\omega_0} \qquad\qquad [5.12]$$

In case the radicand is smaller than zero $\delta^2 - \omega_0^2 < 0$ the both roots [5.9] are complex conjugate:

$$\lambda_{1/2} = -\delta \pm \sqrt{(\omega_0^2 - \delta^2)(-1)} = -\delta \pm j\sqrt{(\omega_0^2 - \delta^2)} \qquad [5.13]$$

The root from equation [5.13] is called *damped natural circular frequency* and is related to the natural circular frequency and the damping ratio as follows

$$\omega_d = \sqrt{\omega_0^2 - \delta^2} = \omega_0\sqrt{1 - \left(\frac{\delta}{\omega_0}\right)^2} = \omega_0\sqrt{1 - \xi^2} \qquad [5.14]$$

In vibration theory there is one more dimensionless magnitude called *quality factor* that for high values is related to the damping ratio as follows

$$Q = \frac{1}{2\xi} \qquad [5.15]$$

Since publication of the norm DIN 1311-2 in August 2002 [70] the intensity of damping in the mechanical one – dof system is classified into four categories. They are presented in the Table 5.1. They are defined by different magnitudes described by equations [5.3], [5.12], [5.14] and [5.15].

Table 5.1 Four grades of damping intensity

light damping	strong damping	critical damping	over-damping
$\xi \ll 1$	$\xi < 1$	$\xi = 1$	$\xi > 1$
$Q > {}^1\!/_2$	$Q > {}^1\!/_2$	$Q = {}^1\!/_2$	$Q < {}^1\!/_2$
$\omega_d \approx \omega_0$	$\omega_d < \omega_0$		$\omega_d > \omega_0$

The tires belong to the lightly damped single dof vibration system. The one of the nonlinearity of the tire is revealed by the excitation amplitude. Because the test by free oscillation and test by random vibration provide other magnitudes of vertical tire stiffness and damping ratio, in the next subsections the detailed calculation way is presented.

5.1.2   Test by free oscillation

This chapter describes test of vertical step response of the tire. During the test by free oscillation the physical magnitudes of velocity and steer angle were measured only to control the test conditions. The signal used to evaluate the vertical stiffness and damping ratio presented the movement of test wheel in relation to the ground after rolling over the obstacle. The acceleration signal of the test wheel was used for this purpose [63].

The test wheel overcame square beam with unobserved excitations at the first attempt of this test. This phenomenon of pressing in the beam with small height as a consequence of large volume and elasticity of *ag* tires, was observed also by Mr. von Holst [14]. As the height of the beam was increased the whole frame of tire test rig began to pitching, e.g. oscillating around its lateral axis Y_{TR}.
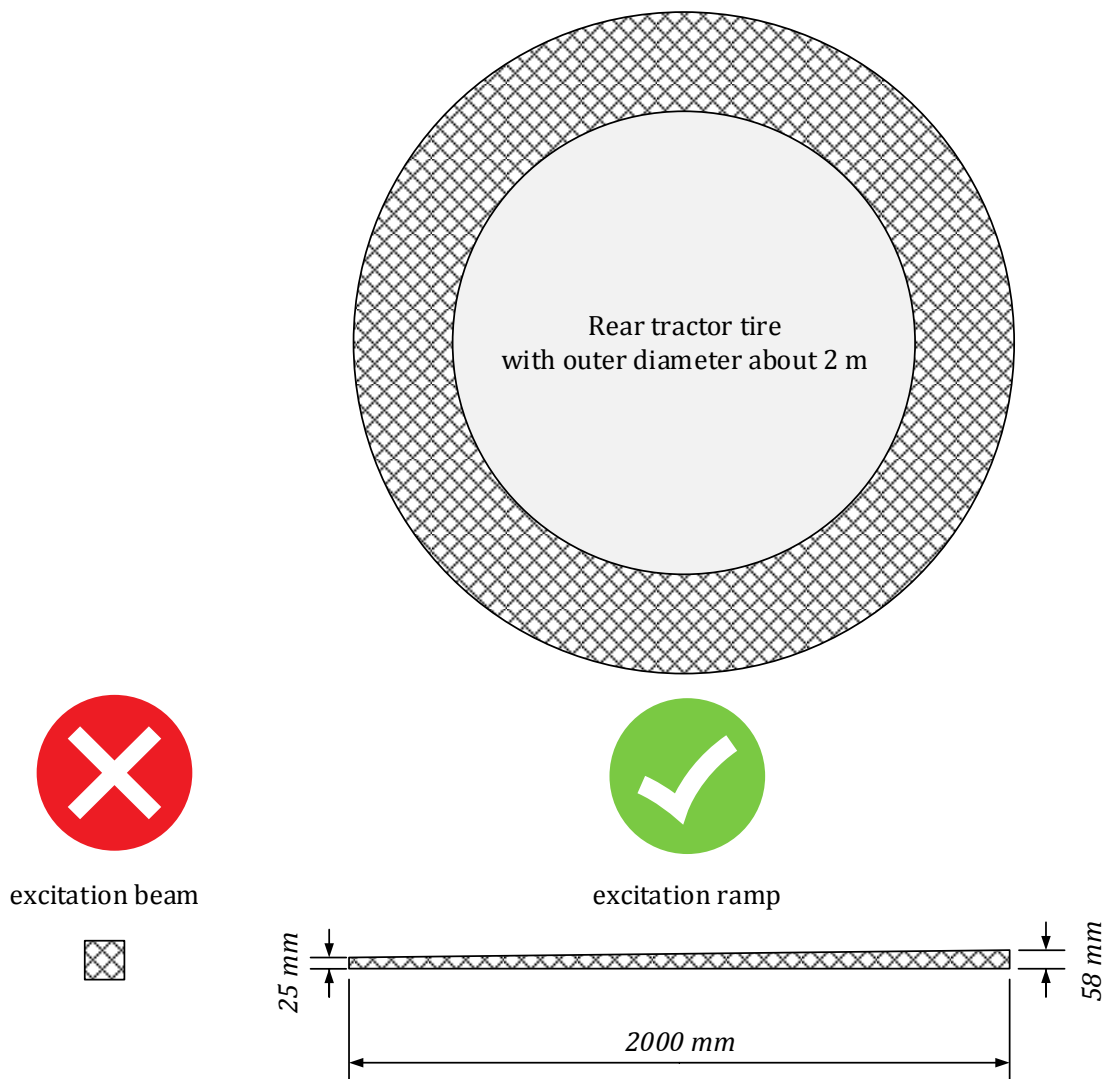
Figure 5.3 The excitation ramp

Under these circumstances a ramp with rectangle trapezoid longitudinal cross section that is presented in the **Figure 5.3** was developed. The ramp was used instead of beam with rectangular cross section for vertical excitation. The width of the ramp used for this test equals *620 [mm]*. That guarantees that the whole tire's patch roll over the ramp.
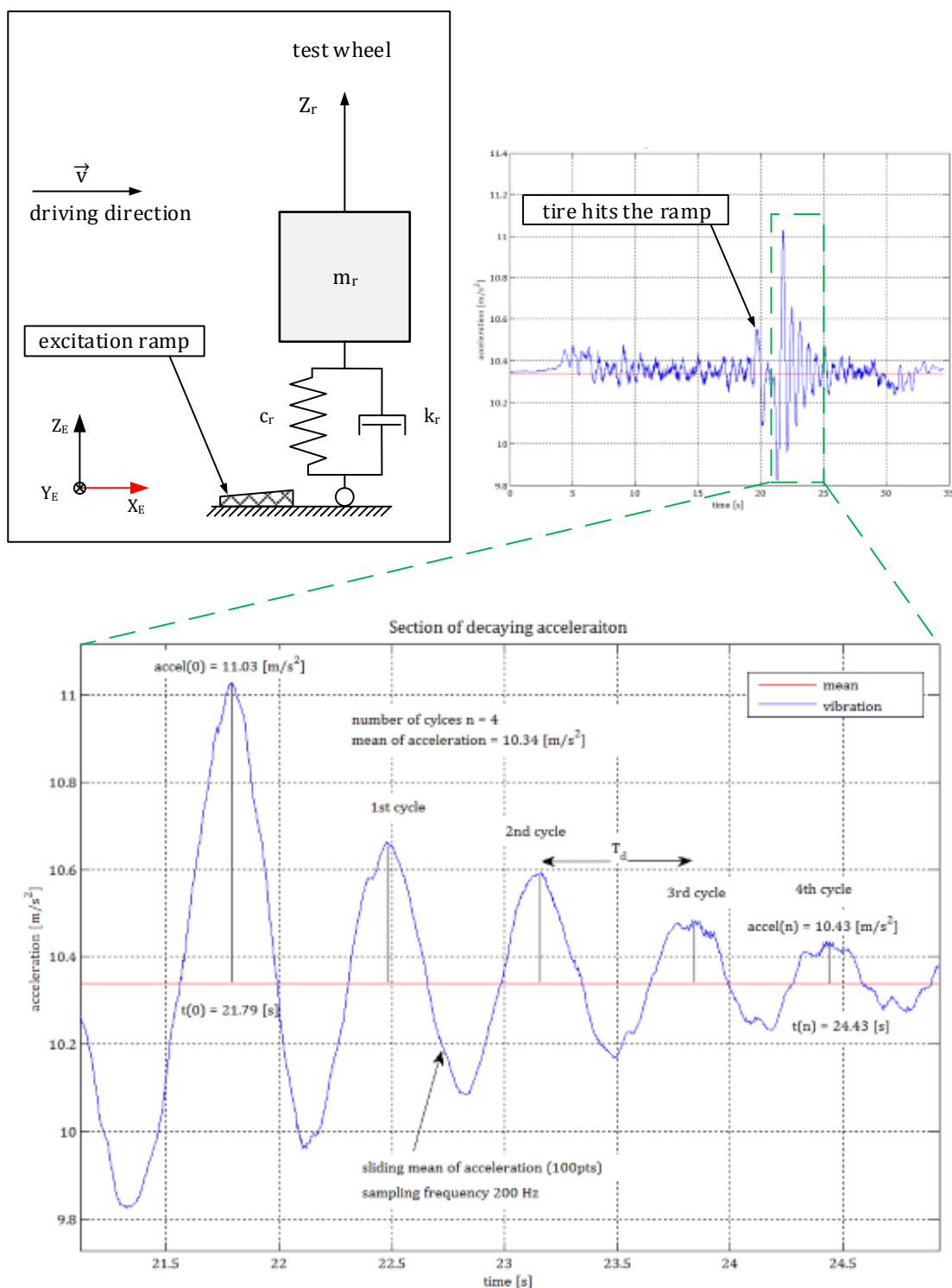
Figure 5.4 History of vertical vibration of the test wheel

The front height of the ramp of *25 [mm]* was determined by the strength of wooden beams. The length of the ramp equals *2000 [mm]*. In general the greater length is better because the tire must retrieve its unpressed, nearly round form during rolling over the ramp. This is even more important for higher driving velocities, when the tire travels in shorter time over the ramp. The **Figure 5.4** presents the vibration signal of the test wheel in the vertical direction during test by free oscillation by the driving speed *5 [km/h]*. The tractor's rear tire with payload $m = 3300\ [kg]$ was mounted in the test rig. On the plot in the right upper corner the point where the tests tire hits the ramp is visible interchangeable. Next the vibration falls in and the tire is dropped down from the rear edge of the ramp on the road surface. The rear height of the ramp was *58 [mm].* It was larger than the front edge but smaller than the height of the profile pattern. Between the front and rear edge of the ramp the potential energy of the test wheel is smoothly increased and additionally the tire returns into its uncreeped shape. As the tire travelled through the ramp the certain work that was equal to payload times *32 [mm]* was always carried out independently from driving velocity. As the velocity increased it changed simultaneously the time in which the work was carried out. Because of that the energy which the tire was exposed to increases with the driving velocity. The functionality of the ramp relies on the fact that nearly undeformed tire is exposed rapidly to the certain excitation.

The signal of vibration plotted with blue line was evaluated by the *sliding mean[2]* algorithm. The acceleration signal is sampled with *200 [Hz]* frequency. The block of sliding mean has the size of *100* points. The mean of this particular vibratory sample plotted with red line creates symmetry value. The oscillation signal is convergent to the symmetry value. This is crucial for calculating the amplitude of free damped vibrations. Because the signal goes through 'zero' more than one time the system must be light or strong damped, see Table 5.1. The section of decaying acceleration is chosen from vibration signal, see **Figure 5.4** bottom. Six values are read from this part of the signal: time of the zero peak $t(0) = 21.79\ [s]$, the value of the zero peak $\ddot{z}_r(0) = 11.03\ [m/s^2]$, time of the *n-th* peak $t(n) = 24.43\ [s]$, the value of the *n-th* peak $\ddot{z}_r(n) = 10.43\ [m/s^2]$, the value of the vibration mean $\ddot{z}_{r\ mean} = 10.34\ [m/s^2]$

---

[2] Also called *running avarage.*

and the number of oscillation cycles $n = 4$. Taking into account more than one vibration cycle minimalizes the inaccuracy that arises due to read off error. So the period of damped vibration equals $T_d = \frac{t(n)-t(0)}{n} = 0.66 \ [s]$. The damped natural circular frequency equals

$$\omega_d = \frac{2\pi}{T_d} = 9.52 \ \left[\frac{rad}{s}\right] \tag{5.16}$$

The *logarithmic damping decrement* can be calculated also using the plot. The first free damped amplitude equals $\ddot{z}_r(t) = \ddot{z}_r(0) - \ddot{z}_{r \ mean} = 0,69 \ [m/s^2]$ and the amplitude after n cycles equals $\ddot{z}_r(t + nT_d) = \ddot{z}_r(n) - \ddot{z}_{r \ mean} = 0,09 \ [m/s^2]$. Those values yield

$$\Lambda = \frac{1}{n} ln \frac{x(t)}{x(t + nT_d)} = 0.5092 \ [-] \tag{5.17}$$

The decay rate is logarithmic decrement divided by the period of damped vibration T_d

$$\delta = \frac{\Lambda}{T_d} = 0.77 \ \left[\frac{1}{s}\right] \tag{5.18}$$

The natural circular frequency can be calculated using the damped natural circular frequency and decay rate as follows

$$\omega_0 = \sqrt{\omega_d{}^2 + \delta^2} = 9.55 \ \left[\frac{rad}{s}\right] \tag{5.19}$$

In order to calculate the spring constant the mass must be multiplied by squared natural circular frequency

$$k = m\omega_0{}^2 = \ 301 \cdot 10^3 \ \left[\frac{N}{m}\right] \tag{5.20}$$

The damping ratio equals the decay rate divided by natural circular frequency

$$\xi = \frac{\delta}{\omega_0} = 0.0808 \ [-] \tag{5.21}$$

The viscous damping constant equals

$$c = \delta 2m = 5.09 \cdot 10^3 \ \left[\frac{Ns}{m}\right] \tag{5.22}$$

The three parameters of the tire in vertical direction: the spring constant k, the viscous damping c, and damping ratio ξ are results of every test run.

5.1.3   Test by random excitations

The purpose of this method is to define stiffness and damping constant of the tire in vertical direction for **small amplitude** excitations. The precise definition of limit between small and great amplitude is not known at this stage of tire research in general. This method relies on processing acceleration signal $\ddot{z}_r$ (see **Figure 5.2**) that represents the vibration of the tire. The sensor acquitting the output signal is mounted on the axle of the test wheel. Other physical magnitudes as longitudinal velocity and steer angle are measured only to control the test conditions. The signal samples obtained from test of rear wheel by velocity of *25 [km/h]* are here used for explanation of the method of random vibration. The payload equals 33*00 [kg]*; the steer and camber angle equal *0°*. The test wheel is not braked or driven. In order to prepare the signals to the frequency analysis and check-up the severity they are processed first in the time domain.

Statistical properties of random vibration in time domain

In general the road irregularities generate broad band *random* excitation with Gaussian density function [66]. The tire is subjected to these excitations. In order to identify the system based on the acceleration signal $\ddot{z}_r$ it must be checked if it has really *Gaussian* distribution. In general if one LTI system is subjected to the Gaussian excitation its response has the Gaussian distribution too. However, for the system as tire that is not very strong damped and therefore strongly resonant, one exception is permitted. It means that if such system is subjected to the broad band excitation the response tends to be Gaussian even if the input is not. This is very important relationship because properties of the input are not known. Relying on the literature the excitation is not white noise but only covers the resonance peak of response. The term of *white noise* is used to wide band process which PSD has uniform density through all frequencies. This lets to analyse the system based only on the output signal.

The term of *Gaussian random process* implies that the ensemble of time function is included for time *t* between $-\infty$ and $+\infty$. In practice, including this research, it is not possible to complete process analysis by a large numbers of an acceleration signals according to the time with a very long duration. The full list of tests is shown in the **C.11** and **B.2.2.** It indicates that there are five up to ten record of one process.

Fortunately the random movements follow well-defined statistical laws and the Gaussian character is replaced with two very useful notions that are called **stationarity** and **ergodicity.** Those properties enable to limit the statistical process analysis made up of several recordings with reasonable duration.
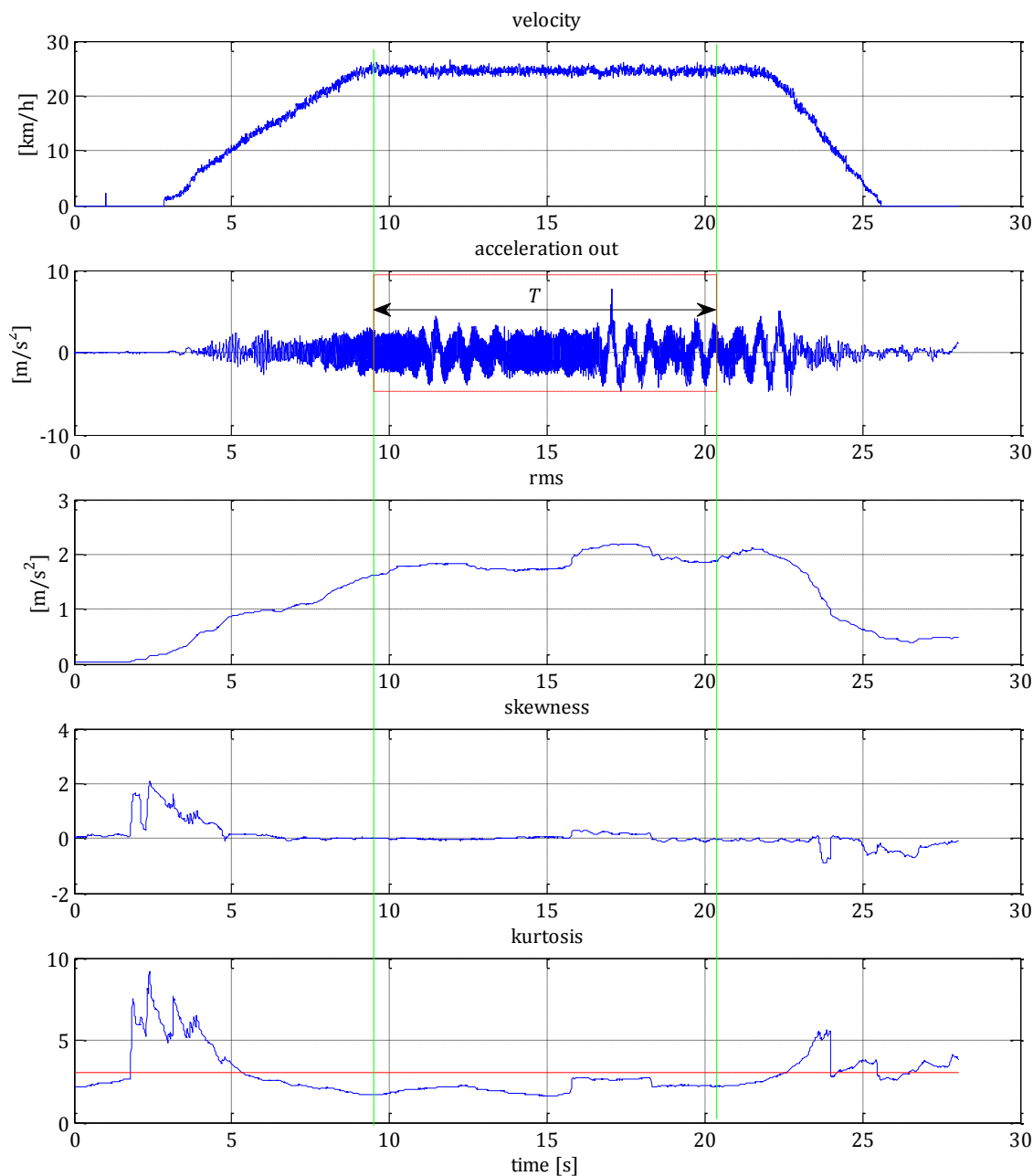
Figure 5.5 Juxtaposition of velocity, acceleration and sliding mean of rms value, skewness and kurtosis according to time

The ergodicity can be determined by comparing temporal and ensemble averages. One process is ergodic if all temporal averages (such as: the mean, mean square value, standard deviation) exist and have the same value as the corresponding

ensemble averages calculated at an arbitrary given moment. An ergodic process is automatically stationary.

Because the vibratory signal acquainted during one test ride contains several phases (see **Figure 5.5**) as parking, accelerating, driving with constant velocity and decelerating and parking again it would be pointless to calculate ensemble averages. Those phases are known as 'events'. Additionally there is much too less recordings for one driving speed to calculate ensemble averages. Because of that fact it was not possible to calculate the ensemble statistical properties. Thus it was not possible to determine if the acceleration signal is ergodic, *strictly* or even in *wide-sense stationary*. But the stationarity can be defined by means of temporary averages.

The temporal averages yield one value for the whole recording. Therefore they are called 'along the process' averages. The application of an algorithm known as *sliding mean* enabled to break down the signal into particular events. In this particular case it focuses on block of *500* consecutive points. It can be applied to calculate different averages. The curves are smoother for higher numbers of points. The stationarity is defined when the statistical process properties do not evolve over time. In practice it is sufficient that only the *rms value* does not change in relation to time.

In order to separate those events the driving velocity, the acceleration signal and the sliding mean of rms value are plotted one above another, see **Figure 5.5**. The whole random vibratory signal of response is clearly non-stationary over duration of one test ride. However thanks to *rms value* it can be divided into short intervals of duration *T* that are still long enough with respect to the time of response of the dynamic system. Thus, the *rms value* between two green lines in **Figure 5.5** varies sufficiently slowly so the vibratory signal surrounded by red rectangle can be regarded as *quasi-stationary* random function. Further, as it is usually made in practice, it is assumed that the process is ergodic too. The stationary part lasts ca. *12* seconds. The range between the fourth and ninth second has transient distribution. The separated section of the recording fully represents the process. However, the length of signal must be sufficient in order to conduct frequency analysis with required accuracy. This is discussed in the next subsection.

In order to decide if the output signal has *Gaussian* distribution the property of *skewness* and *kurtosis a*re drawn with sliding mean of the same size in the **Figure**

5.5. The skewness defines the symmetry of probability density law with regard to mean. The kurtosis makes it possible to estimate the flatness of the probability density curve. Therefore, instead of superposing the histogram of acceleration signal with Gaussian distribution it is possible to define the shape of histogram by numbers. The skewness and kurtosis for Gaussian instantaneous distribution equals to *0* and *3*, respectively. This condition is fulfilled quite well for signal segment between two green lines. The small exception appears between second *16* and *18* where step on both skewness and kurtosis curve appears. The kurtosis is clearly lower than *3* what means that the probability histogram is flatter than typical Gaussian plot. Only the section between second *16* and *18* lays nearer to the value of *3*. In general the plot of kurtosis against time, drawn with sliding mean, easy enables to detect the presence of local irregularity of the signal due to a shock or due to loss of signal. Since rapid increase of kurtosis is present in every recording around *16th* second it seems that it is caused by asphalt joints marked also in the **Figure 5.1**.
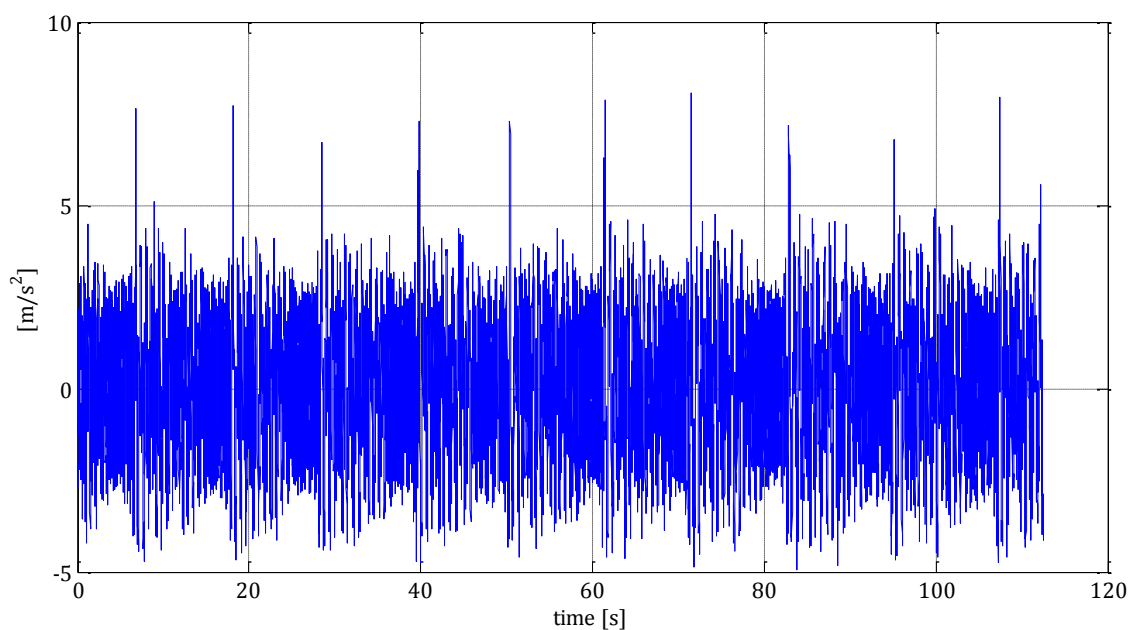
Figure 5.6 Centred acceleration signal of rear tire vibratory response

The stationary section of vibration was cut out from every test run. These ten sections were brought to zero by subtracting mean value and merged into one stationary signal, see **Figure 5.6**. Such sections with finite duration are called *pseudo-random vibration*. The term *pseudo* indicates that in case of road vehicles are always any variations between samples due to external environmental condition or

load distribution within the vehicle. However, since the mean value of the merged signal equals zero the boundary conditions for test rides with in one velocity were kept constant and the influence of environment were minimal. It verifies the autostationarity too by method used by Ulrich [44]. The temporal averages equals: rms value $\ddot{z}_{r_{rms}} = 1.93 \frac{m}{s^2}$, $skewness = 0.08$ and $kurtosis = 2.43$. Therefore the final centred signal can be considered as *stationary*, *ergodic* but only nearly *Gaussian*. Therefore every centred signal representing the tire's vibratory response for one velocity will be described by the rms value, skewness and kurtosis in order to qualify its statistical utility.

Random vibration properties in the frequency domain

The frequency content of quasi-stationary random signal provides very useful information about mechanical system which undergoes the vibration. The *Power Spectral Density,* denoted by its acronym **PSD** is a result of transferring the signal from time into frequency domain. The *PSD of acceleration* signal indicates intensity of magnitude of measured signal over the frequency *f*. The PSD is calculated by means of *Fourier transform*. Thus, the resulting curve has unit of square of acceleration divided by frequency: *(m/s²)²/Hz*. In frequency analysis there are two requirements regarding the choice of filter bandwidth that must be satisfied: first, the frequency bin should be narrower than a quarter of the width of expected resonance peak. Second, the statistical error should remain smaller than *15%.* These rules limit the bias error ε_{bias} and statistical error ε_{stat} within reasonable ranges. The total error equals

$$\varepsilon = \sqrt{\varepsilon_{bias}^2 + \varepsilon_{stat}^2} \qquad \left[\frac{N}{m}\right] \qquad [5.23]$$

The total error shall be less than $\varepsilon < 20\%$. Because of the nature of bias and statistical error, there is always a conflict between resolution and precision. Therefore as it is suggested by Lalanne [71] (p. 216) there were conducted two analysis with different PSD parameters. First analysis was conducted with narrow filter in order to emphasize resonances and second analysis with broader filter in order to improve precision. The magnitudes of filter bandwidth and statistical error depend on sampling frequency, Anti-Aliasing filter, sample duration, averaging, overlapping and windowing. In order to achieve right resolution and precision the certain PSD settings were calculated for two scenarios. The short explanation of the

strategy and values of averaging, overlapping and windowing are pointed out to increase the comprehensibility of this work. The script of this algorithm is saved in m-file <PSDparam> which is included in the appendix B3.

First, the filtered and digitalized merged signal sample is described by total duration, displayed in seconds, and the number of points. The duration of signal presented in the **Figure 5.6** equals *112.49* seconds and contains *22498* points. The signals were digitized with $f_{samp} = 200$ [Hz] sampling rate.
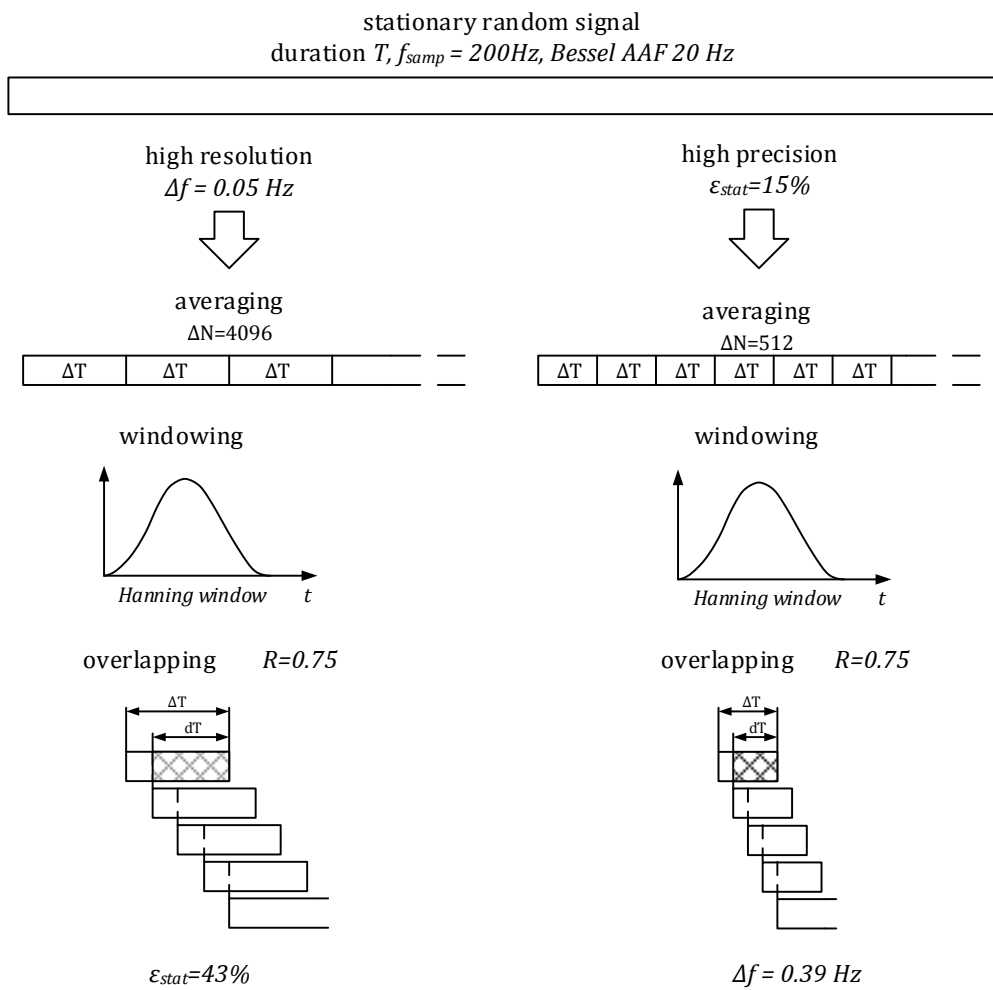
Figure 5.7 Two strategies of PSD calculation

Further, the m-file calculates parameters necessary to conduct the PSD estimation with **high resolution** (narrow filter). Basically there is no reason to expect narrower resonance peak of CM – tire than *0.2 [Hz]* [44]. Since the filter width equals $\Delta f = 0.05$ [Hz] the first rule is fulfilled. So the bias error is about *3%* of the width and *2%* of amplitude of the peak. The number of degree of freedom equals $n = 11.24$. In general it should be approximately *90*. According to that the number

of PSD points between 0 and Nyquist frequency $\left(f_{Nyq}\right)$ M are calculated. Because of the Fourier analysis the number of M is increased to the next power of 2. In such a way is calculated the number of points per block $\Delta N = 2 \cdot M = 4096$. Having the size of the block, the number of blocks after **averaging equals** $K = 5.49$. In the next step the acceleration signal is multiplied by Hanning window. This is one of the most frequently used window for mechanical vibration analysis. It has the most appropriate properties as the width of main lobe and high roll-off side lobes rate [72]. Therefore the Hanning window is used for each PSD estimation. The **overlapping** is conducted in the next step. This operation reduces the statistical error by averaging higher number of blocks keeping the duration T of the signal constant. In this particular case the overlapping keeps the length of the block ΔT constant and calculates the new number of overlapped blocks $K' = 18.97$. For this particular window the overlapping rate $R = dT \, / \, \Delta T \; = 75\%$ guarantees negligible amplitude ripples [71] (p.205). That makes it the most rational value. The statistical error $\varepsilon_{stat} = 43\%$ is calculated at the end of definition of PSD parameters with the purpose of high resolution. The magnitude of statistical error exceeds the *15%* what is not satisfactory. In other words the estimation of PSD with those parameters and calculating the vertical stiffness and damping ration of rear tire is subjected to a massive calculation error. Therefore it represents very purely the physical system.

The **second part** of the algorithm calculating the PSD parameters is logically inverted. The PSD calculation parameters are defined in such a way in order to guarantee the **precision** of PSD curve. The initial condition is set by statistical error $\varepsilon_{stat0} = 15\%$. The total duration T and the number of points of digitalized signal sample N are the same. Further the order of calculation is quite similar. Using the statistical error and the number of points in the whole merged signal sample the number of points M is calculated. Dividing *Nyquist* frequency by the next power of two of number of points of PSD, yields the new frequency step that equals $\Delta f = 0.39 \, [Hz]$. Further the number of degree of freedom $n = 87$ and the number of points per block $\Delta N = 512$ are calculated. Now the magnitude n has desirable value. Next the operation of averaging and overlapping are taken into account. The new number of blocks after averaging and overlapping $K' = 172$ is calculated. The new statistical error reduced because of greater number of blocks $\varepsilon_{stat} = 10\%$ is calculated as the last property in the list of PSD parameters. So the second

requirement regarding the choice of filter bandwidth in frequency analysis is full field with these settings. But in general for such short duration of this particular analysed vibratory signal it is not possible to obtain good resolution whilst preserving an acceptable statistical error.
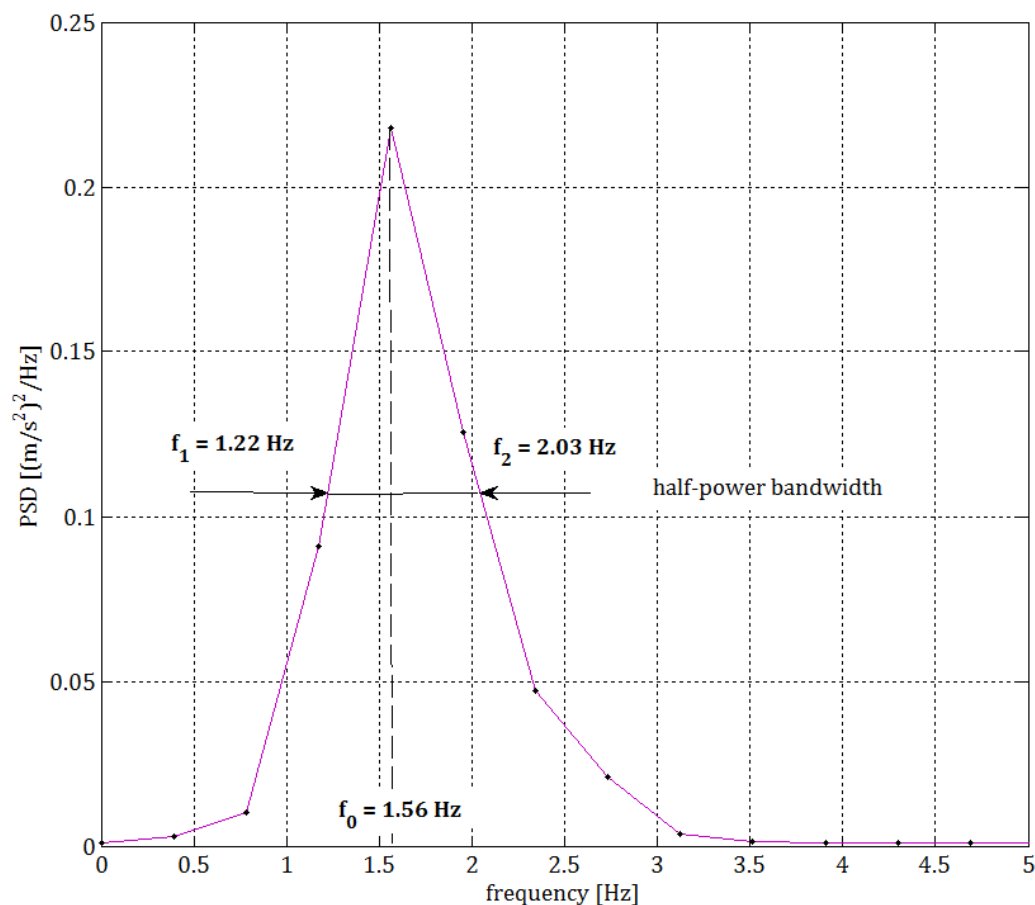
Figure 5.8 PSD of response signal of rear wheel by velocity *25 [km/h]* calculated with an statistical error $\varepsilon_{stat} = 10\%$ and frequency resolution $\Delta f = 0.39\ [Hz]$

Though of great potential of adding zeroes for artificially smoothing the PSD curve this operation was not applied. However it can be pointed out that the resolution and statistical error stays unchanged by adding zeroes. The additional points of the PSD lie between the original points corresponding to the duration ΔT. Taking into account the massive importance of filter width used for analysis and statistical error they are specified on every PSD curve. The plot of one-sided PSD has linear axis. This is necessarily for this approach. The autospectrum in normalised for reading signal *rms* value. The algortihm for calculating the PSD takes into account the size of the window and apply right *coherent* and *noise gain* [72].

Equivalence between bandpass filter and one-dof linear system

According to the equivalence suggested by D.M. Aspinwall the perfect bandpass filter and linear one-dof system let the same quantity of power pass in response to white noise excitation [71]. This statement enables identification of tire's parameters as stiffness and damping ratio by usage of PSD of vibratory response signal. The identification of the system is carried out with transfer function of the first definition because in this approach is used only the outputs signal. The transfer function $|H_1(f)|$ is strongly peaked near f_0 for lightly damped system. That lets replace in practice the actual excitation by a fictitious white noise with constant PSD. Even further it is permitted that the input signal does not have to possess uniform power density. The equivalent white noise excitation is equal to that of the actual excitation at the natural frequency of the system [73], see the **Figure 5.9**.
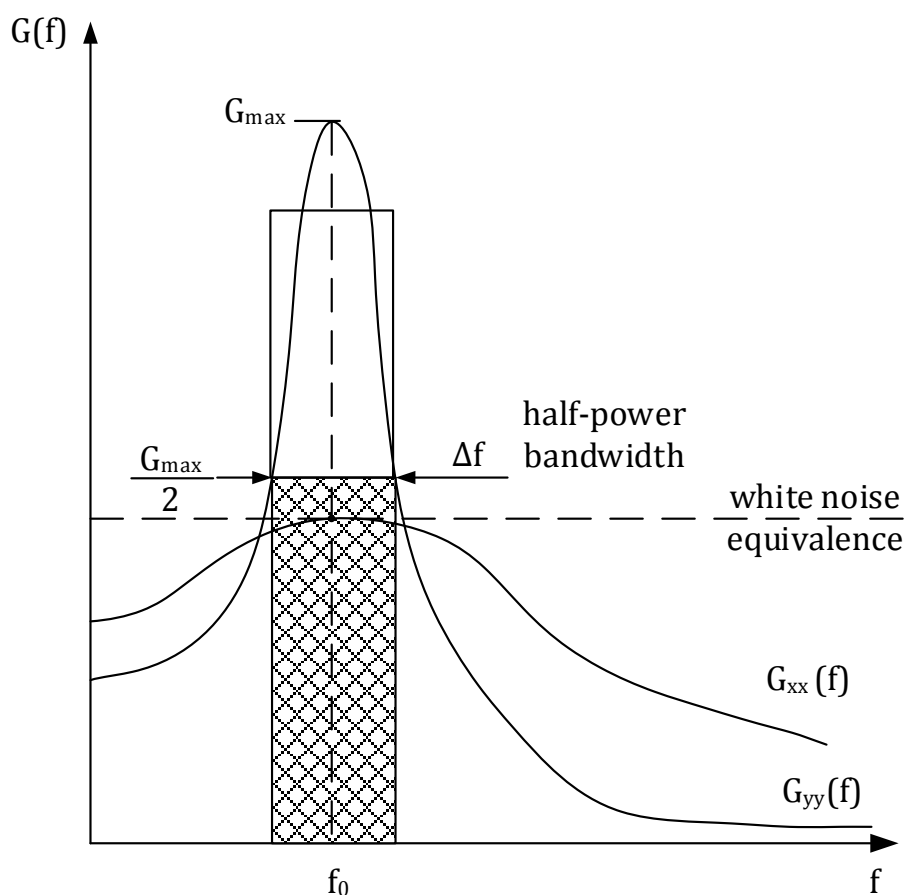
Figure 5.9 Time invariant single input single output linear system

The shape of PSD curve and its position along the frequency axis lets determine the system properties. The quality factor Q can be calculated by dividing the natural

frequency f_0 by the half-power bandwidth Δf of the PSD at the resonance. The values form **Figure 5.8** are used for calculation

$$Q = \frac{f_0}{\Delta f} = \frac{f_0}{f_2 - f_1} = \frac{1.56}{0.81} = 1.92 \, [-]$$

[5.24]

The half-power bandwidth is equal to the difference between frequencies where the amplitude of the response is half its maximum. The stiffness can by calculated by transferring the equation **[5.3]** into

$$k = m\omega_0{}^2 = 317 \cdot 10^3 \left[\frac{N}{m}\right]$$

[5.25]

In order to calculate the damping ratio the equation **[5.15]** can be transformed into

$$\xi = \frac{1}{2Q} = 0.26 \, [-]$$

[5.26]

The damping coefficient can by calculated from equations **[5.4]** and **[5.12]** as follows

$$c = 2\xi m\omega_0 = 16.844 \cdot 10^3 \left[\frac{N \cdot s}{m}\right]$$

[5.27]

The three parameters of the tire in vertical direction for excitation with small amplitude: the spring constant k, the viscous damping c, and damping ratio ξ are results of every test run.

5.2 The lateral tire-ground characteristics

The investigation of the tire-ground characteristics in horizontal plane by mobile test rig on the real surface is one of the main aims in this research. The cornering stiffness, e.g. the dependency between side tire forces and wheel slip angle, was chosen as the most influential characteristic during collision avoidance. Because the asphalt test lane was only *3* meters wide with grass-land on the sides, see **Figure 5.1**, as soon as one wheel was driven on the meadow the test run was interrupted by simply engaging the coupling, see **Figure 5.10** around *18th* second. This was conducted due to the fact that the stability of the whole vehicle is guaranteed as long as the cornering stiffness of front and middle axis is equal or greater than rear one. In the moment when the front tires of tractors meet the grass-land, the cornering stiffness would decrease significantly. It would cause the loss of steady-state driving in the bend for certain velocities, see section 4.2. Under these circumstances this test was interrupted as soon as one wheel left the asphalt

surface. In consequence it was sometimes reduced to only transient phase. Since the transient tire-ground characteristics can be very poorly modelled by DEM simulation, this test is even more attractive. The process of this test was as follows (see **Figure 5.10**). The tractor was driving with velocity of *5 [km/h]* straight forward, and around 8th second the rear test wheel was braked with constant pressure. Subsequently, around *12th* second the rear test wheel was steered to the left for angle about *10* degrees. After engaging the coupling, around *17th* second the whole vehicle was rolling into the curve. It was finally stopped by braking test wheel around *18th* second. The braking pressure exceeds set pressure by switching on as a consequence of insufficient reaction time of reducing pressure valve. The longitudinal force reflects it immediately. There is around one second delay between beginning of steer angle changes and rising of the lateral wheel force, F_{Y_C}. Around *18th* second the longitudinal force changes its direction. This occurs already when the whole vehicle is stopped.

The forces in the center of the wheel are plotted for purpose of this test. However they serve also to prove the functionality of the wheel force sensor.
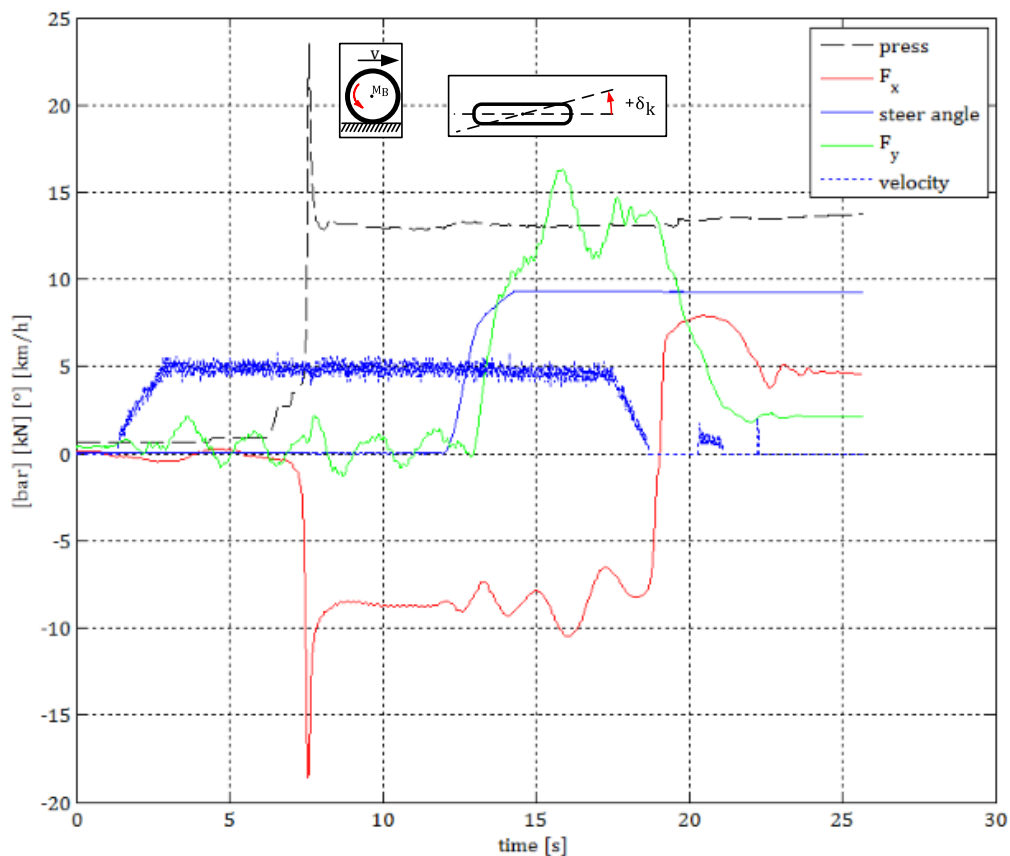
Figure 5.10 Test overview obtained within signals from test of cornering stiffness

5.2.1   Step response of lateral force

In order to calculate the slip angle of the rear wheel α_r five signals must be involved. **Figure 5.11** depicts the signals in the graphical manner by usage of single track model. **Figure 5.12** represents the signals measured during one test run. The steering angle δ is measured indirectly by the stroke of hydraulic cylinder, which moves the steering-knuckle. The vehicle slip angle is calculated by dividing the lateral velocity by longitudinal velocity

$$\beta = arctg\left(\frac{v_y}{v_x}\right) \cong \frac{v_y}{v_x} \ [°] \tag{5.28}$$

The distance between the center of balance and the rear wheel l_r varies in dependence of mounted wheel. It equals $l_r = 2.95 \ [m]$ and $l_r = 3.1 \ [m]$ for rear and front wheel respectively. The yaw rate and resulting velocity are measured directly on the vehicle and acquired by measuring instrument. The wheel slip angle is calculated (with five signals plus the constant value l_r) according the following equation:

$$\alpha_r = \delta + \beta - l_r \cdot \frac{\dot{\psi}}{v} \quad [°] \tag{5.29}$$

The wheel slip angle is shown in the **Figure 5.12** on upper plot.
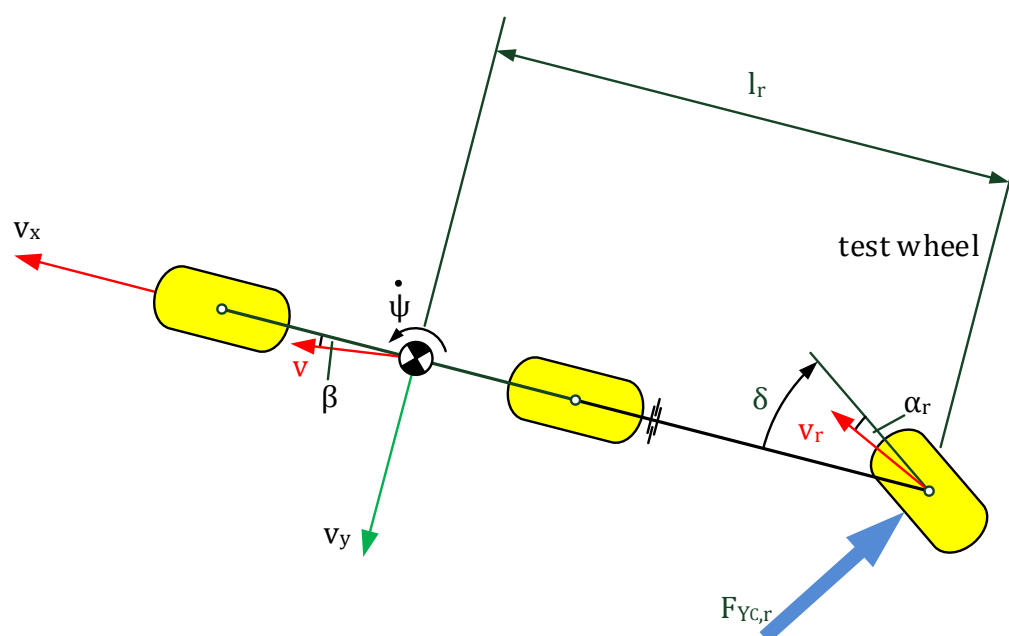
Figure 5.11 Single track model presenting parameters needed to calculate the side force of test wheel in function of wheel slip angle

Since the symmetrical planes of the wheel force sensor and of the rim overlays each other (see **Figure 3.25**) the vertical and longitudinal forces do not influences the load rings in the *y* direction. However the longitudinal and lateral forces oscillate slightly as a consequence of test wheel bouncing. After braking and especially turning the test wheel, the vertical fluctuations become more intense. Additional reason for oscillations of the wheel side force is cross-over talk from the axis *x* into the axis *y* which equals about *10%*, see section 3.4.3. The lateral force acting in the center wheel axis coordinate system F_{Y_C}, that is presented in the **Figure 5.11** was calculated by usage of only four signals: *ay, cy, ey, fy* without taking into account the signal of wheel rotation.
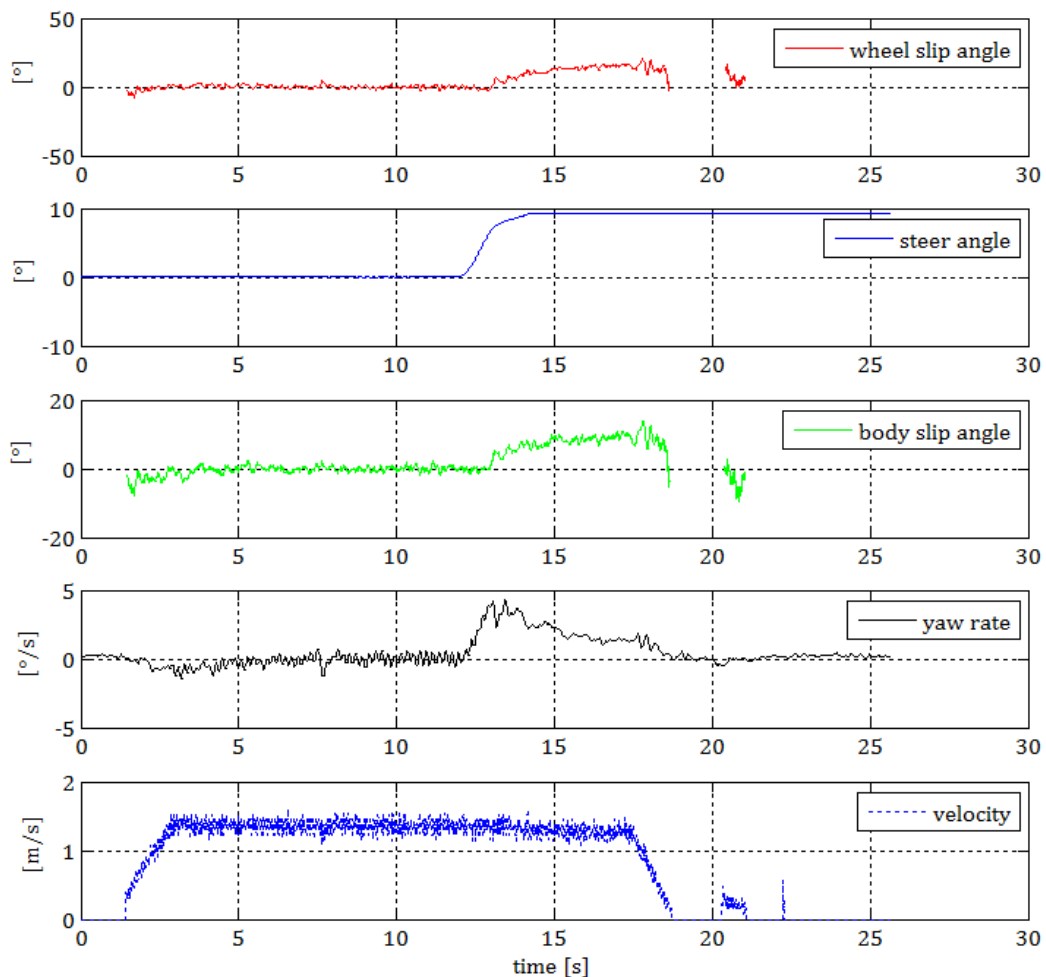
Figure 5.12 Kinematic signals used for calculation of the wheel slip angle, α_r

First, the single load ring signals were centered so that their zero line is common for four transducers; see the indices '*m*' in the equation [5.30]. The addition of the signals from load rings that lays in front of each other let clear out the influence of

moment around OX and OZ axis: $\{sig33 = ey_m + ay_m;\ sig44 = fy_m + cy_m\}$. Because of small fluctuation in the signal *sig33* and *sig44*, they were added to minimize it. The fluctuations occur due to the fact that the active load rings do not cover the circumstance in the uniform manner. So in order to keep the formula expressed by equation [3.73] and [3.74] the signals were multiplied by 3/2. The signals were also multiplied by trend line factor and coefficient 2.5 in order to take into account the difference in supply voltage comparing with calibration.

$$F_{Y_C} = (ey_m + ay_m + fy_m + cy_m) \cdot \frac{3}{2} \cdot x\_coeff \cdot 2.5 \qquad [5.30]$$

In the similar way the longitudinal force F_{X_C} was calculated (see **Figure 5.10** and the equation [5.31]). Four signals proportional to the force acting on the load cells in the direction: *ax, cx, ex, fx* are used in this algorithm. The signal of wheel rotation is not taken into account too. Because of fluctuations caused by different factors the calculation was conducted in a very similar manner as for the side wheel force. The addition of signal from load cells laying in front of each other lets clear out the influence of vertical force F_{Z_C}. The particular pairs of forces are denoted in the algorithm as follows: $\{sig3 = ex_m + ax_m;\ sig44 = fx_m + cx_m\}$. According the assumption taken within the section 3.4.2 about the lack of longitudinal force acting along axis X_C, the longitudinal force F_{X_C} comes from the rolling resistance, braking or traction and therefore is sensed also as the moment around wheel rotation axis. As it is shown in **Figure 5.10** between the second *3* and *7*, the longitudinal force behaves very smoothly when the tire test rig already drives with constant velocity of *5 [km/h]* and is not braked. However the fluctuations are so big that force caused by rolling resistance obfuscates. The great advantage of the fact that the longitudinal force is recalculated from moment around wheel central axis M_{Y_C} is that the nonuniformity of active load rings along wheel circumference does not play any role. Additionally the stiffness of the single load ring along axis *z*, that is not measured does not disturb sensing the longitudinal force. The complex explanation of the origin of the longitudinal is described in the subsection 3.4.2.

$$F_{X_C} = (ey_m + ay_m + fy_m + cy_m) \cdot \frac{3}{2} \cdot x\_coeff \cdot 2.5 \qquad [5.31]$$

The calculation of vertical force is preceded as described in the section 3.4.2. The instantaneous angular position of the wheel φ is used to calculate the vertical force.

The results of algorithm calculating the vertical force and the algorithm of restoring the exact wheel rotation basing on the real data are presented in the appendix B.

The cornering stiffness is calculated out of stationary relation between the wheel slip angle and side force. In this particular case even when the steer angle and the velocity achieved its constant value, the wheel slip angle drifts slightly, see **Figures 5.10, 5.12, 5.13**. Additionally, the obstacle in assigning the cornering stiffness out of stationary behavior is that the side forces oscillates significantly as soon as the steer angle obtains its final value, see **Figure 5.13**.
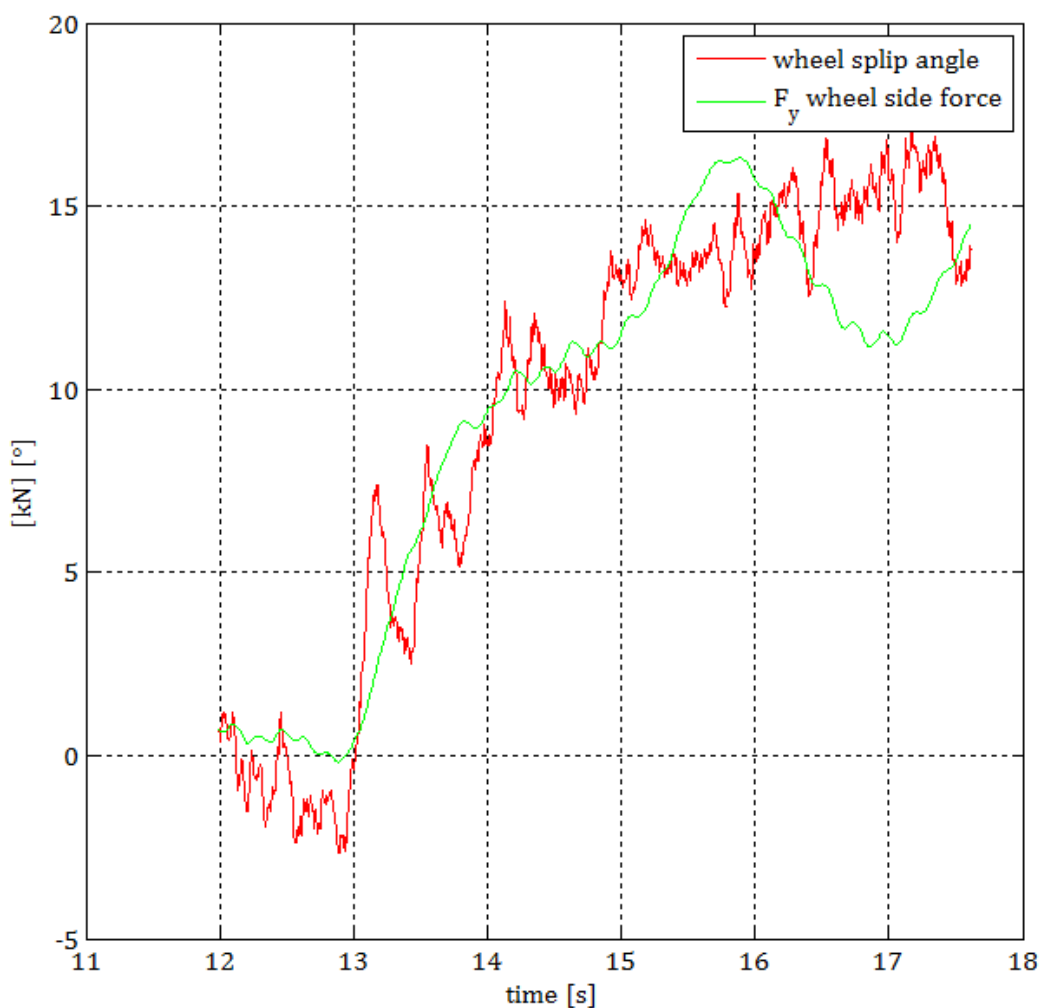
Figure 5.13 Signals used for calculation of the cornering stiffness

Therefore in this approach the cornering stiffness is calculated out of transient behavior. The **Figure 5.13** presents the section of transient lateral force and wheel slip angle. They were superimposed in order point out their dependency. The cornering stiffness comes into being when the side force is plotted in function of wheel slip angle. The result of such transformation of two functions in time domain

into data collection that does not deserves for the term function. The fitting that represents the cornering stiffness was conducted with the method of last-squares and it was plotted with the green line on the **Figure 5.14**. It has a form of *1st* degree polynomial function $y = a \cdot x + b$.
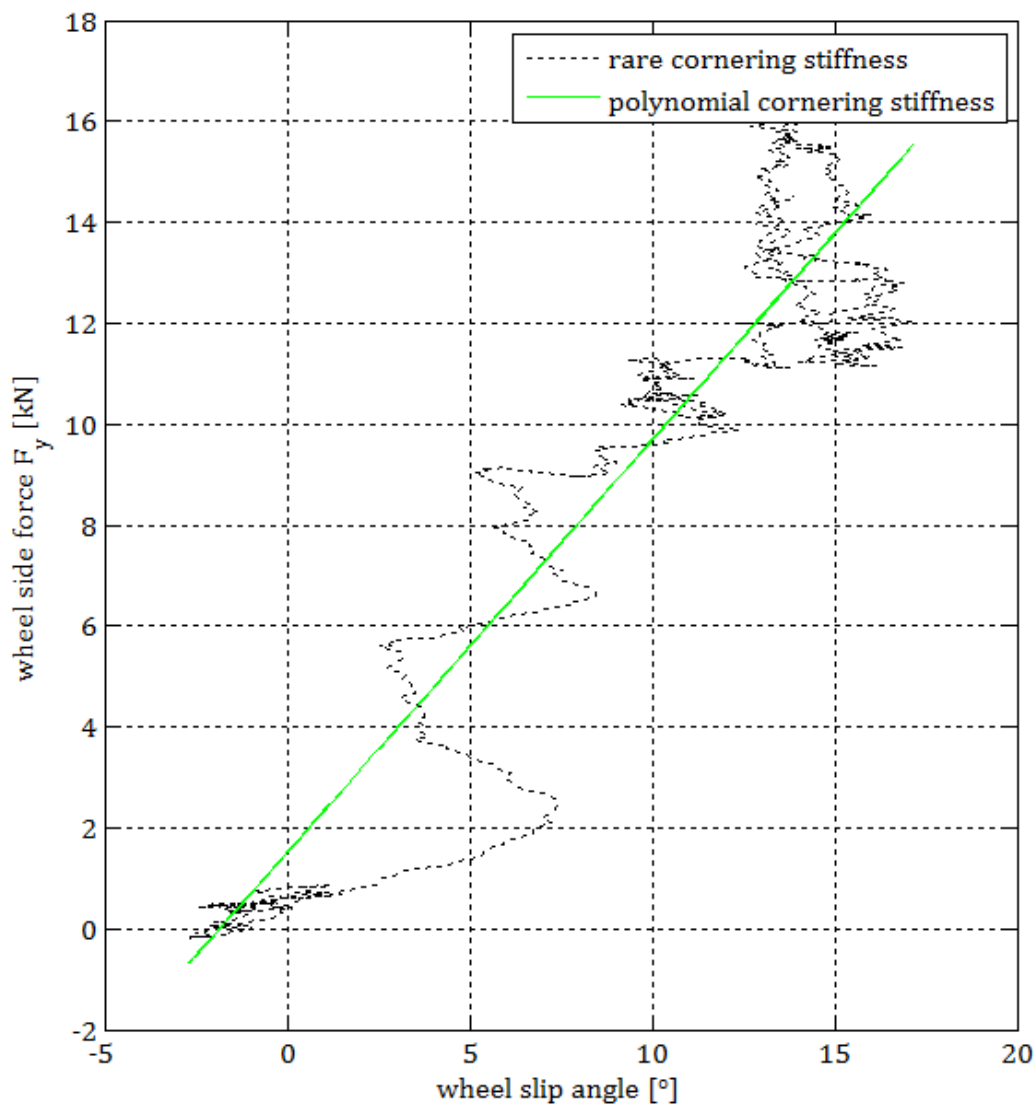
Figure 5.14 The cornering stiffness calculated out of transient phase

Because the linear function does not go through the zero besides the coefficient determining the stiffness there is a magnitude '*b*' which defines the initial force for zero degree steer and wheel slip angle. The offset can appear due to non-zero camber angle.

$$y = 0.818 \left[\frac{kN}{°}\right] \cdot \alpha[°] + 1.49 \, [kN] \tag{5.32}$$

The equation **[5.32]** represents the result of the step response of lateral force test for velocity of *5 [km/h]*. However this is not a substitute of tire – ground characteristic presenting the lateral force in function wheel slip angle.

Chapter 6

6   Results

The results of tire's investigation conducted with three methods and incorporating the mobile tire test rig are presented in this chapter. The tubeless Michelin Xeobib tractors tires were used for the test. The tire inflation pressure was *1.0 bar* for both tires through all tests. The list of all tests conducted during this research is shown in the appendix B.2. They were designed with ultraflex technology. The Xeobib VF710/60 R38 and Xeobib VF600/60 R30 are notations for rear and front tire respectively. According to the manufacturer their design overcomes standard tractors tires in discipline of soil protections and tractions. Thanks up to *24%* bigger footprint they offer up to *50%* reduction of soil pressure. They let save fuel and shorten time in means of reduced up to *20%* rolling resistance and simultaneously reduced wheel slip. The constant inflation pressure up to 1 bar can be applied on the field and on the road. They guarantee handling on the road in means of safe braking, precise steering and ride comfort [74, 75]. Their maximal speed is *65 [km/h]*.

6.1   Results of test by free oscillation

The sections of decaying accelerations of rear wheel measured in free oscillation tests are presented in the **Figure 6.1**. The acceleration signal presented on the plots was evaluated with sliding mean with *10* and *20* points size of block. The acceleration signal processed with the size of block with *10* points especially for velocity of *10 [km/h]* was very swinging and therefore hardly useful for evaluation. However the operation of sliding mean conducted with *20* points size of block guaranteed good run of signal without excessive deformation or flattening. The run of decaying acceleration especially for velocity of *20 [km/h]* did not correspond with good quality of an ideal damped one mass oscillator. It happened due to the fact that rolling over the ramp generated longitudinal force input. This force acted on the level of dynamic radius of the rear tire. This caused pitching movement of the whole test rig's frame.
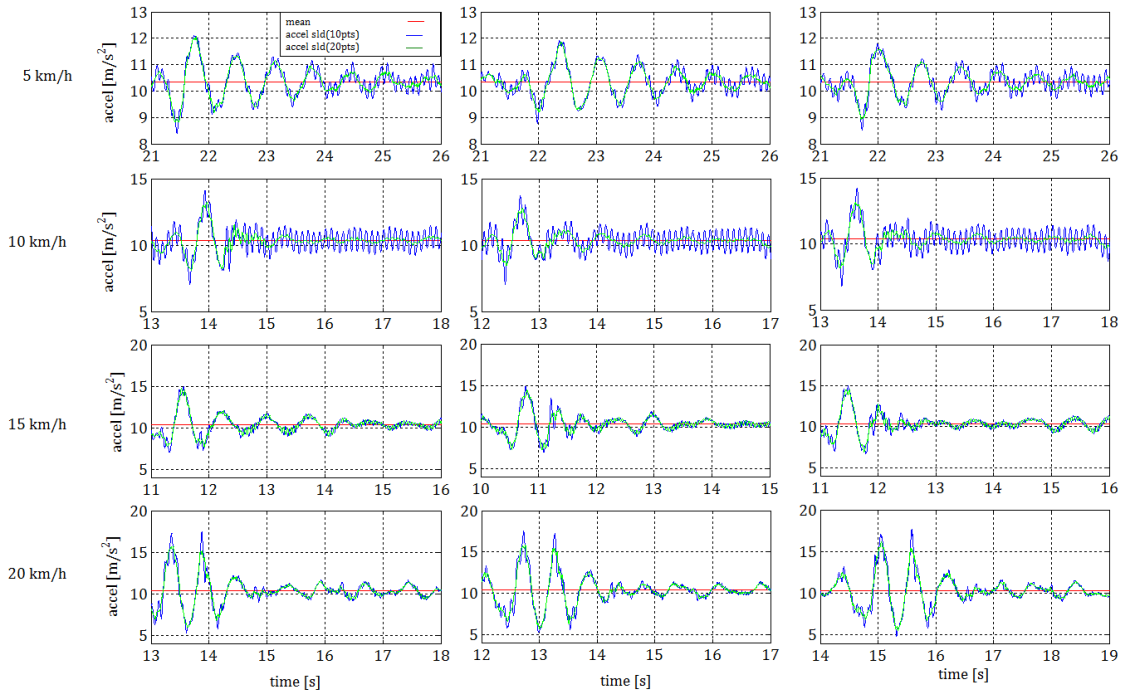
Figure 6.1 Decaying acceleration of rear wheel measured in test by free oscillation
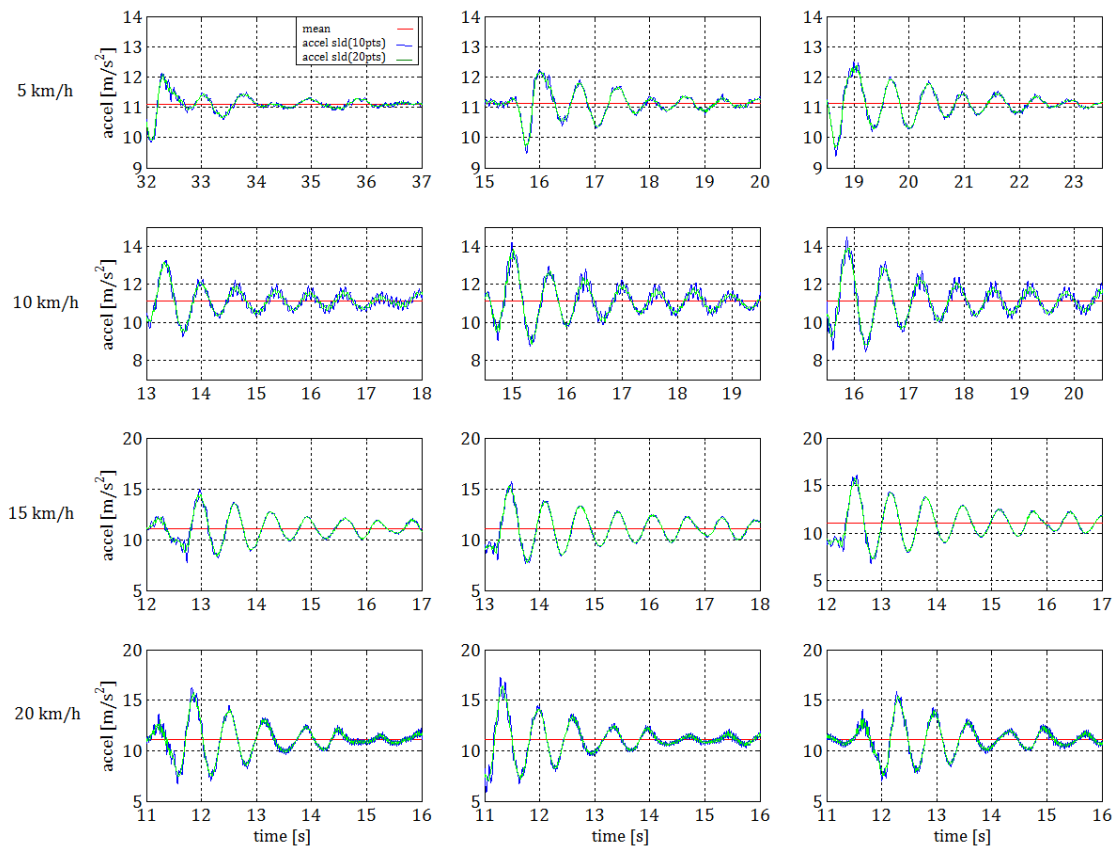
Figure 6.2 Decaying acceleration of front wheel measured in test by free oscillation

The sections of decaying accelerations of front wheel obtained in free oscillation tests are presented in the **Figure 6.2**. The oscillations of signal for velocity of

10 [km/h] was hardly observable. In general the signal's run corresponded more to the decaying acceleration of an ideal damped one mass oscillator. This happened due to the fact that the longitudinal force input acted on significantly shorter level, e.g. dynamic radius of the front tire. The sliding mean block of size *10* and *20* points delivered very similar run of the signal. The **Figure 6.1** and **6.2** contain the information about tire vertical parameters. The maximal velocity of tire test was *20 [km/h]* because of insufficient length of the test track.
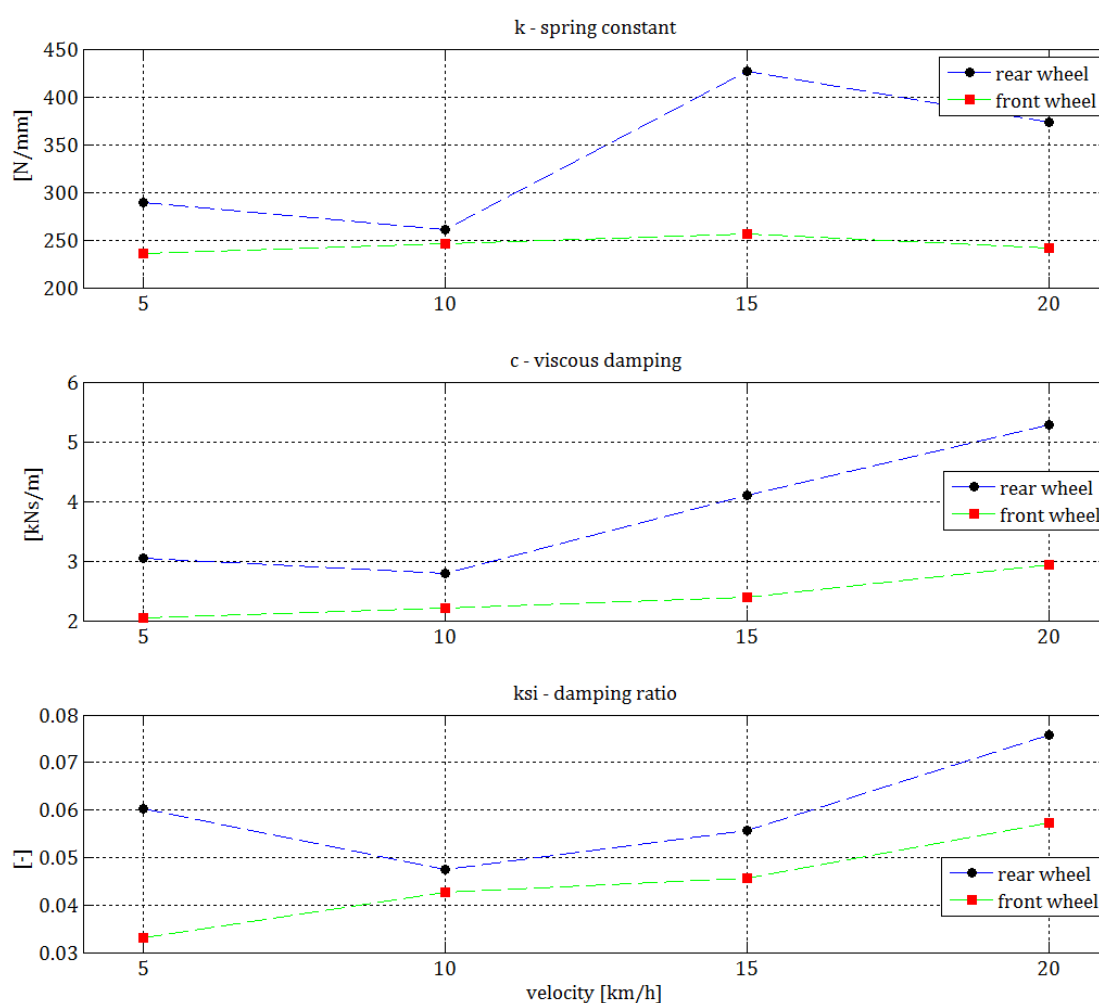
Figure 6.3 Tire parameters for vertical direction measured in test by free oscillation

The stiffness, damping and damping ratio in vertical direction of front and rear tire in function of velocity are presented in the **Figure 6.3**. The three parameters of front wheel are plotted with green line. The blue line presents the parameters of rear wheel. In all three cases the parameters corresponding to the rear tire had greater numerical values than the parameters of front tire. That met the finding of

Langenbeck [18] and von Holst [14] that the stiffness, damping and damping ration increase with rim width and tire volume.

The vertical stiffness of front tire stayed constant with increasing velocity. The vertical stiffness of rear tire increased with increasing velocity. This was opposite to findings by other researchers. That could be explained by the bad quality of the acceleration history for velocity of *10, 15* and *20 [km/h]*. The viscous damping and the damping ratio lightly increased with rising velocity. That was opposite to results of other researchers. But in general the range of stiffness, viscous damping and damping ratio corresponded with the values found in works of Ulrich (1983) [44], Langenbeck (1991) [18], Pickel (1993) [12] and von Holst (2000) [14].

6.2 Results of test by random vibration

The test by random vibration served to investigate the tire's behaviour under stochastic base excitations. The amplitudes of these excitations were smaller than the one in test by free oscillation. Lightly different tire parameters were expected because of nonlinearity of Voigt-Kelvin tire model.

Table 6.1 Statistical parameter of merged quasi-stationary random rear wheel acceleration signal

Parameters	Velocity [km/h]				
	05	**10**	**15**	**20**	**25**
Signal duration $T\ [s]$	360	153	150	107	112
RMS value $\ddot{z}_{r\,rms}\ \left[\frac{m}{s^2}\right]$	0.405	1.080	0.947	1.240	1.933
Skewness $[-]$	0.040	0.185	0.037	-0.320	0.086
Kurtosis $[-]$	1.860	2.088	2.376	2.538	2.428
DOF n $[-]$	140	59	59	42	44
Statistical error ε_{stat}	**7.5 %**	**10 %**	**10 %**	**12.5 %**	**12.5%**

The signal analysis in the time domain was conducted to prove the fact that the response signal was random and stationary, see the Table 6.1 and 6.2. This compulsory analysis was dictated by boundary conditions of this approach. The sampling ratio of *200 [Hz]* and the duration of signal recordings predetermined the accuracy of the PSD estimation. The *rms* value of the acceleration signal indicated its intensity and enabled the comparison between two measurements.
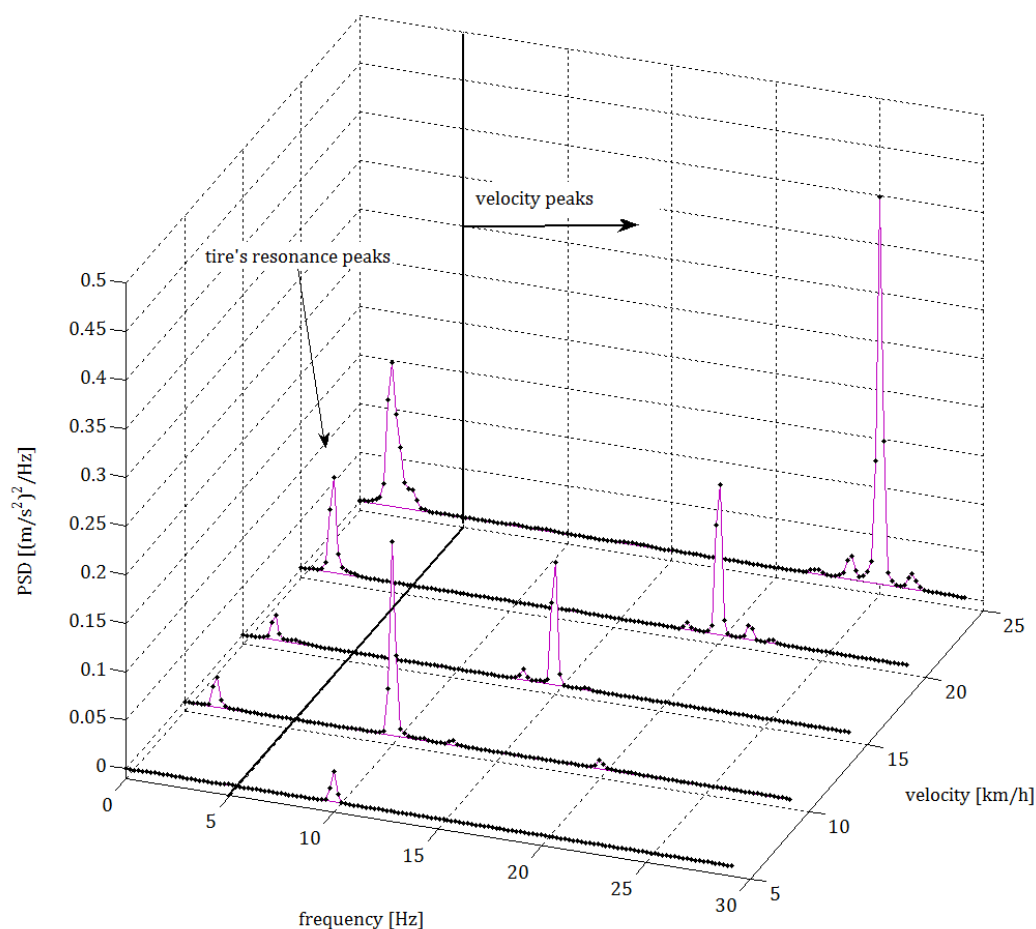
Figure 6.4 Waterfall plot of PSD of rear wheel acceleration (with statistical error see the Table 6.1 and frequency resolution $\Delta f = 0.1953 \ [Hz]$)

Table 6.2 Statistical parameter of merged quasi-stationary random rear wheel acceleration signal

Parameters	Velocity [km/h]				
	05	**10**	**15**	**20**	**25**
Signal duration $T \ [s]$	318	149	157	112	105
RMS value $\ddot{z}_{r\,rms} \ \left[\frac{m}{s^2}\right]$	0.169	0.558	0.698	1.176	1.289
Skewness $[-]$	-0.071	0.261	0.396	0.284	0.145
Kurtosis $[-]$	3.696	2.937	3.180	2.880	3.283
DOF n $[-]$	124	58	61	44	41
Statistical error ε_{stat}	**8.3 %**	**10 %**	**10 %**	**11 %**	**11%**

The plot of skewness and kurtosis enabled to monitor the instantaneous values of acceleration signal in aspect of compatibility with *Gaussian process*. It enabled to

compare probability density of every signal with the Gaussian histogram in very easy way. So the quality of the signal could be defined by number. The symmetry of probability density function of rear wheel vibration signal was quite good but the histogram was flatter than Gaussian distribution, see the Table 6.1. The probability density function of front wheel vibration signal was leaned into the right site but the height of the histogram oscillated around an ideal Gaussian distribution, see the Table 6.2.
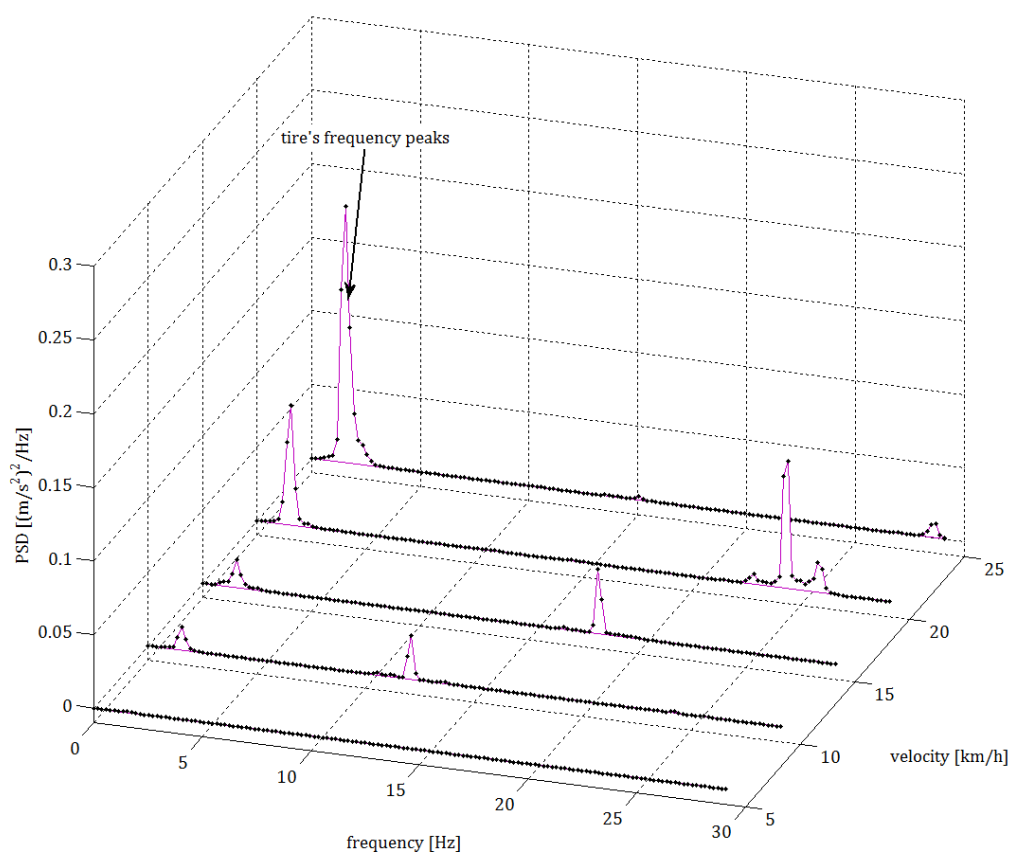
Figure 6.5 Waterfall plot of PSD of rear wheel acceleration (with statistical error see Table 6.2 and frequency resolution $\Delta f = 0.1953\ [Hz]$)

The indices of the frequency resolution and the statistical error were placed on every PSD plot, see **Figure 6.4** and **6.5**. The signal duration and filter width were constrained with each other by statistical error and number n of degree of freedom, as it is listed in the Tables 6.1 and 6.2. Two rules from section 5.1.3 about filter width and statistical error the number n that should equal *90* or more were preserved. The filter width that influences the height of resonance peak much more than statistical error was kept constant for every PSD estimation. It was

$\Delta f = 0.1953 \ [Hz]$ for both front and rear tire. The PSD of acceleration signal by velocity of *5 [km/h]* for rear and front tire did not reveal resonance peak. Therefore it was impossible to determine the tire parameters. In all cases the peak of natural frequency was placed in one and the same location $f_0 = 1.56 \ [Hz]$. It might be caused by relatively wide filter width.
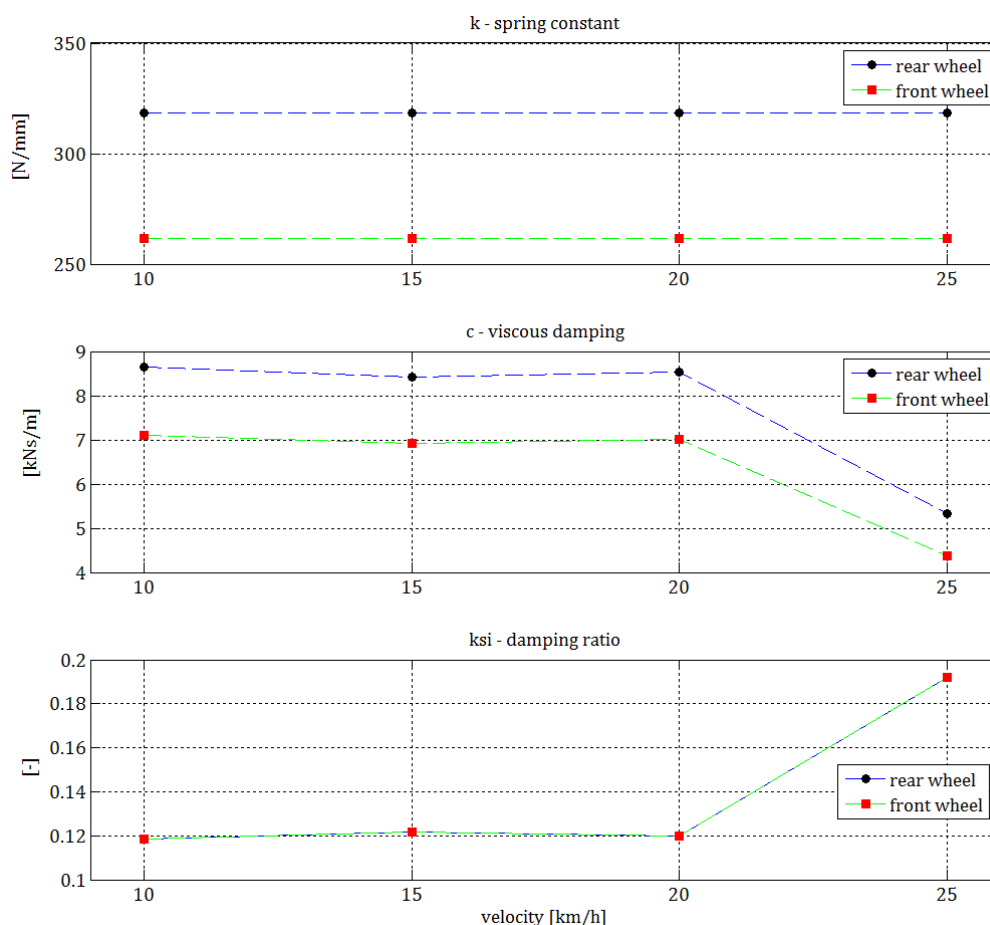
Figure 6.6 Tire parameters for vertical direction obtained in test by random vibration

The resonance peak contained in its shape the quality factor *Q.* This was calculated as the ratio between the numerical value of natural frequency and the value of half-power-width. The tire's stiffness, viscous damping and damping ratio was calculated in further steps. The tire parameters for vertical direction obtained in test by random vibration are shown in the **Figure 6.6**. The spring constant of rear tire was greater than the one of front tire alike as in case of results obtained in test by free oscillations. The stiffness of both rear and front tires had constant value in range of measured velocities that is *10* up to *25 [km/h]*. The stiffness of front tire obtained in

this test is lightly bigger than the stiffness obtained in the test by free oscillations. The viscous damping of rear and front tire was greater than respective values obtained in test by free oscillations. Alike the viscous damping of rear tire was greater than the one of front tire. They had constant value for velocity range from *10* up to *20 [km/h]*. The damping of both tires significantly decreased for velocity of *20 [km/h]*. The damping ratio of both tires was exactly the same in the range of velocity from *10* to *20 [km/h]* and was greater than the values obtained in test by free oscillations. In the velocity range from *10* to *20 [km/h]* it stayed constant and for velocity of *25 [km/h]*, it increased about *50%*. For the accuracy of parameters has influence the value of the quality factor. If it is greater than $Q > 10$ the error is smaller than *10%.*
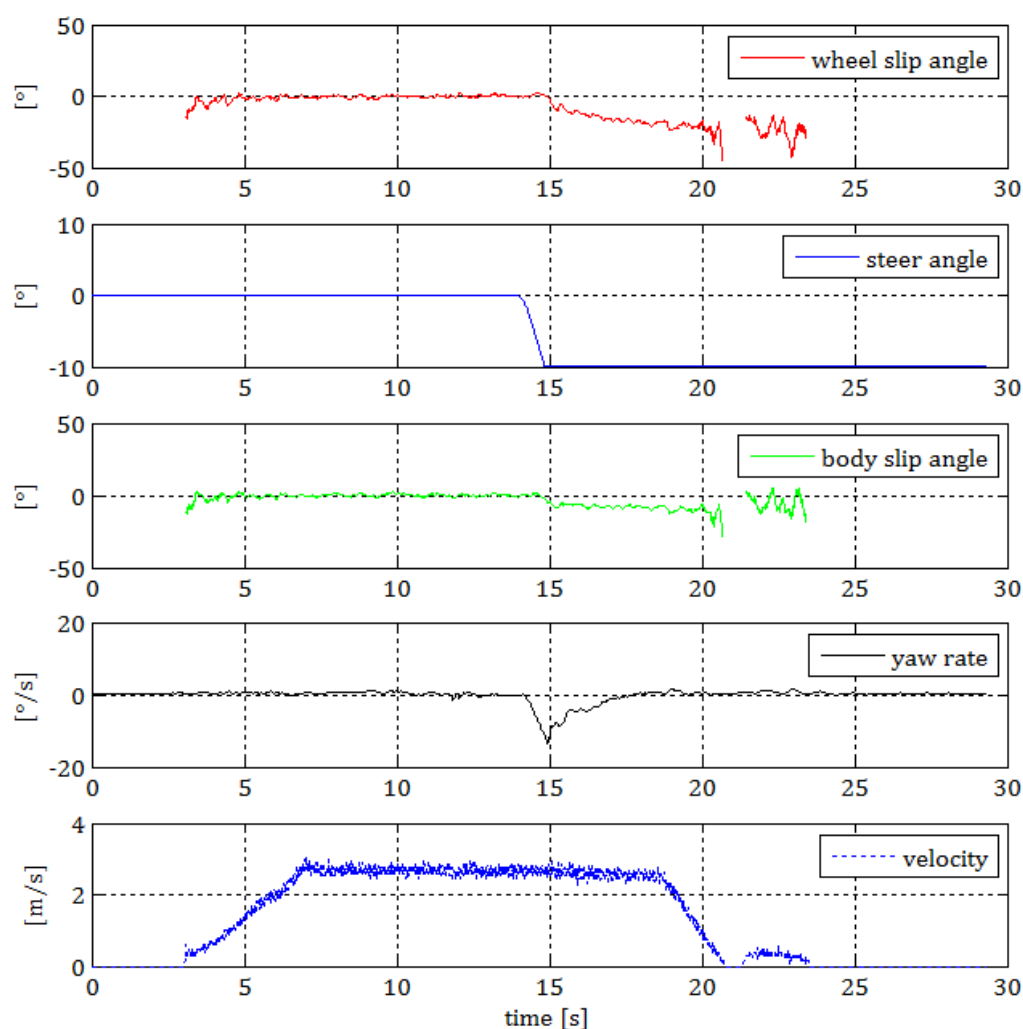
Figure 6.7 Kinematic signals used for calculation of the wheel slip angle, α_r

6.3   Results of step response of lateral force test

The test for estimation of the tire – ground characteristics was conducted only with rear tire. The driving velocity was limited up to *15 [km/h]* because of too narrow asphalt lane (see **Figure 5.1**). The result of this test for velocity of *5 [km/h]* was presented in the chapter 5.2. Therefore, the results of step response of lateral force test only for velocity *10 [km/h]* and *15 [km/h]* are presented subsequently in this chapter.
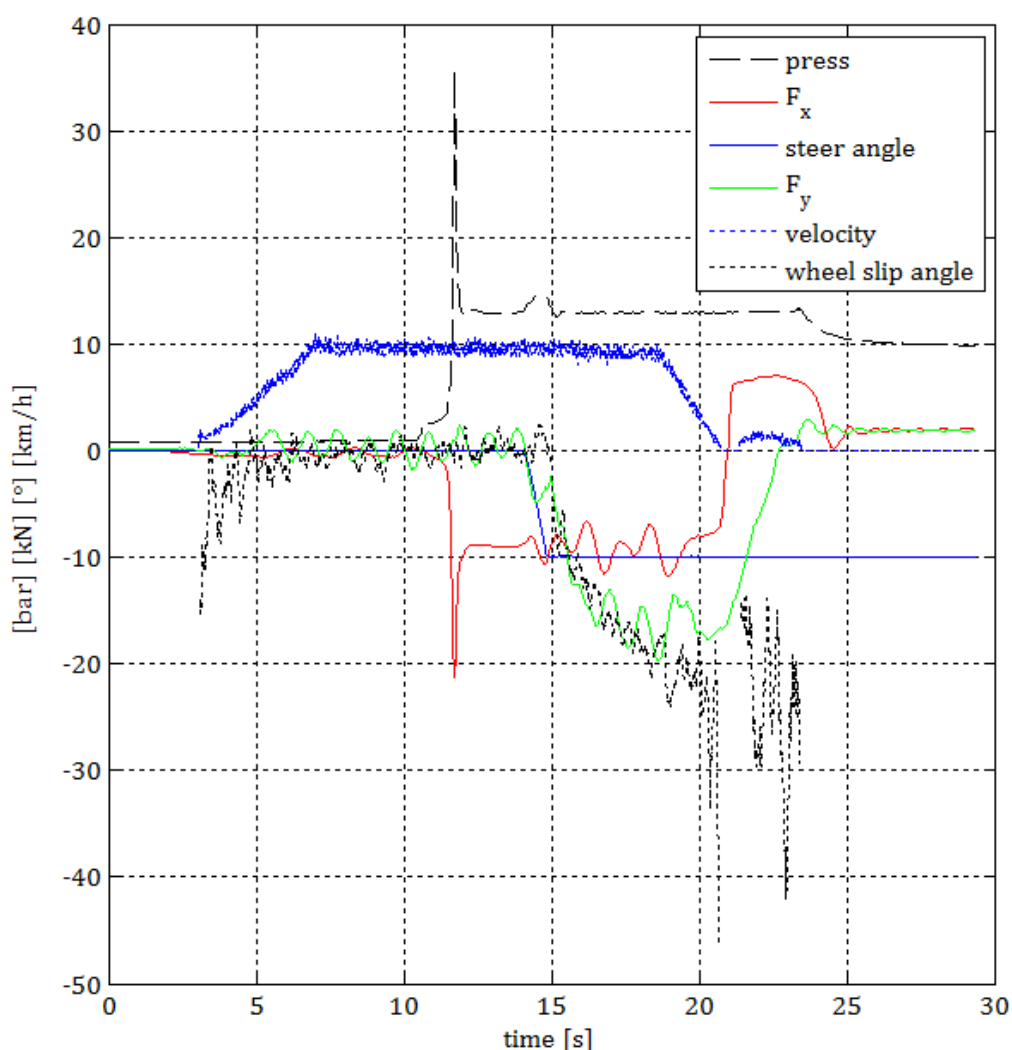
Figure 6.8 Test overview obtained within signals from test of cornering stiffness

Figure 6.7 presents the kinematic signals of test conducted with velocity of *10 [km/h]*. Once the test vehicle almost achieved its stationary state about the 18th second, one of the front wheel leaved the asphalt and the test run was immediately interrupted. At this time the coupling was engaged and the vehicle was stopped mainly by braked and turned test wheel. Because of the decreasing longitudinal

velocity v_x which is located in the denominator, see equation **[5.28]**, the vehicle slip angle β increased, see **Figure 6.8,** even if all other components of wheel slip angle were nearly zero.
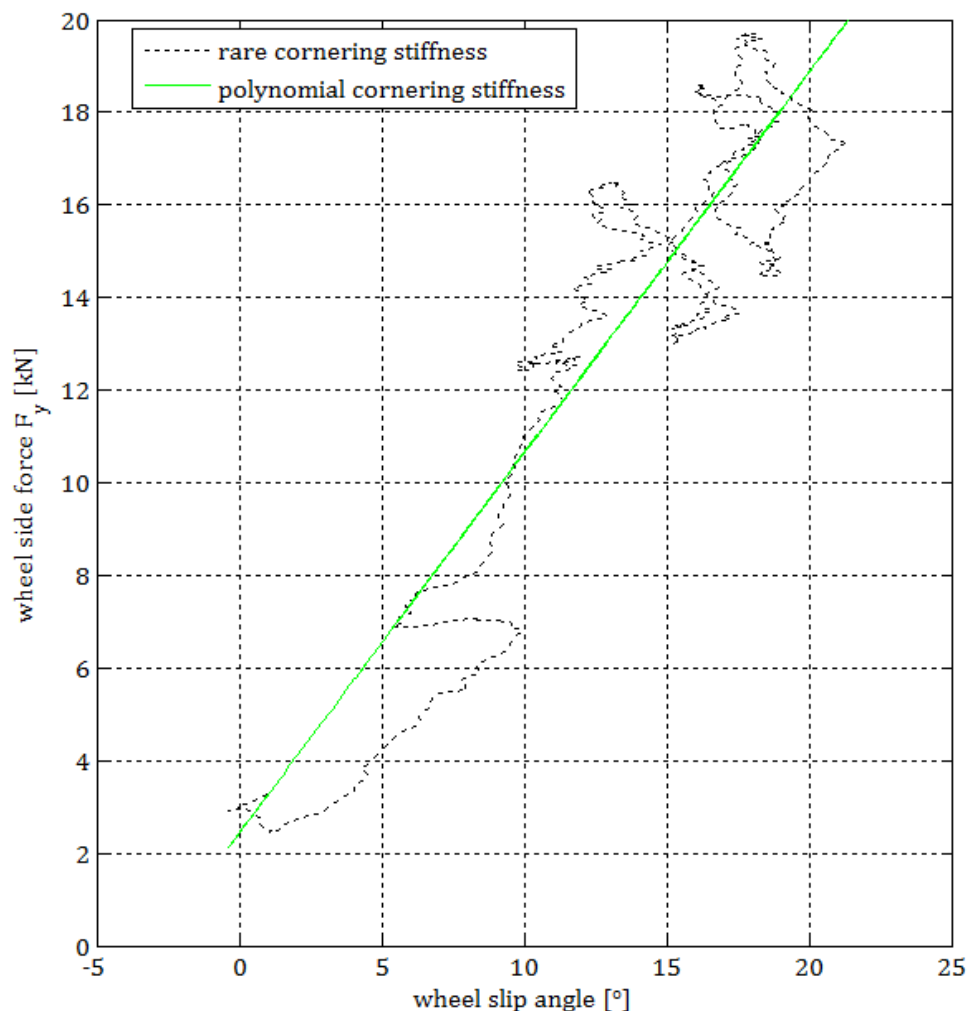
Figure 6.9 The cornering stiffness calculated out of transient phase

The cornering stiffness was roughly the same as for test with velocity of *5 [km/h]*. However the initial offset (in the sense of wheel side force for zero degree of wheel slip angle) was lightly greater; see **Figure 6.9** and the factor *c* in equation 6.1. The reaction time and rising time of lateral wheel force was much shorter because of higher rotation velocity than in case of test with of *5 [km/h];* see **Figure 6.8.**

$$y = 0.818 \left[\frac{kN}{°}\right] \cdot \alpha[°] + 2.14 \ [kN] \qquad\qquad [6.1]$$

The equation [6.1] represents the result of the step response of lateral force test for velocity of *10 [km/h]*.
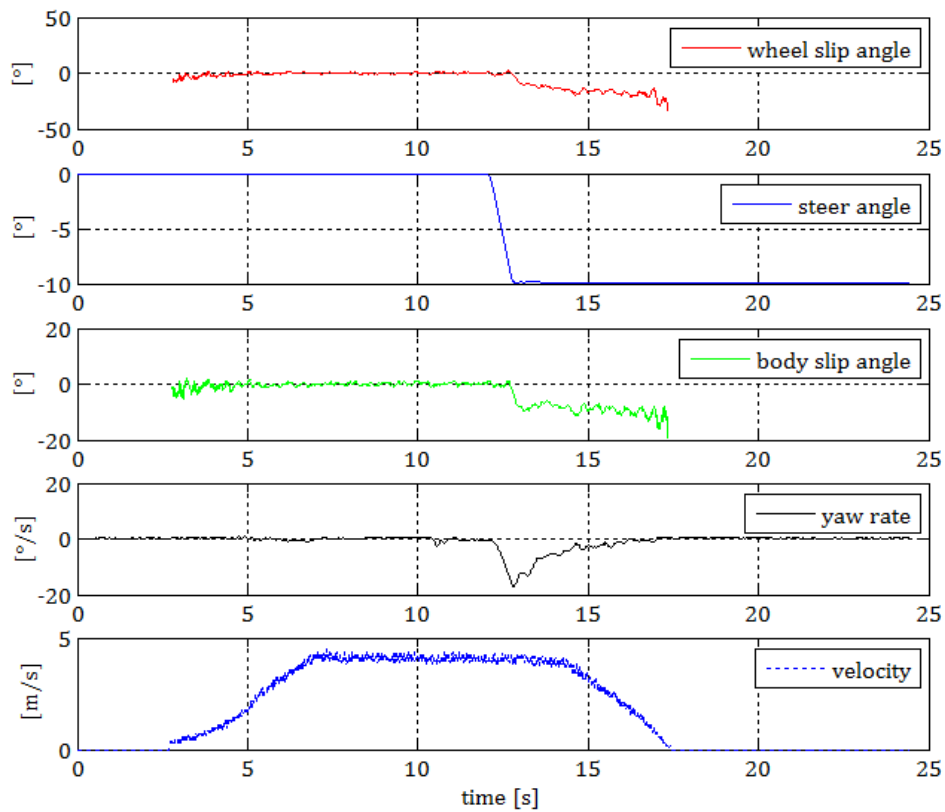
Figure 6.10 Kinematic signals used for calculation of the wheel slip angle, α_r
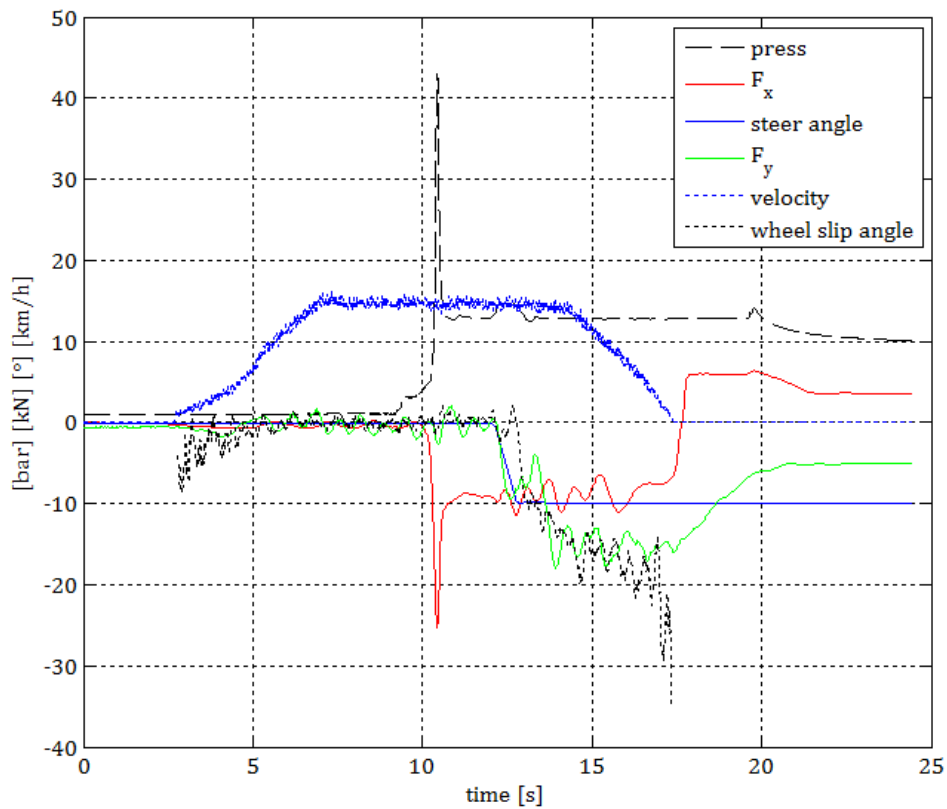
Figure 6.11 Test overview obtained within signals from test of cornering stiffness

Figure 6.10 presents the kinematic signal of test conducted with velocity of *15 [km/h]*. Once the test vehicle almost achieved its stationary state about the 14th second, one of the front wheel leaved the asphalt and the test run was immediately interrupted. Alike as in previous cases at this time the coupling was engaged and the vehicle was stopped mainly by braked and turned test wheel. Because of velocity v_x located in the denominator, the vehicle slip angle β increased; see **Figure 6.10** and **6.11** even if all other components of wheel slip angle were nearly zero.
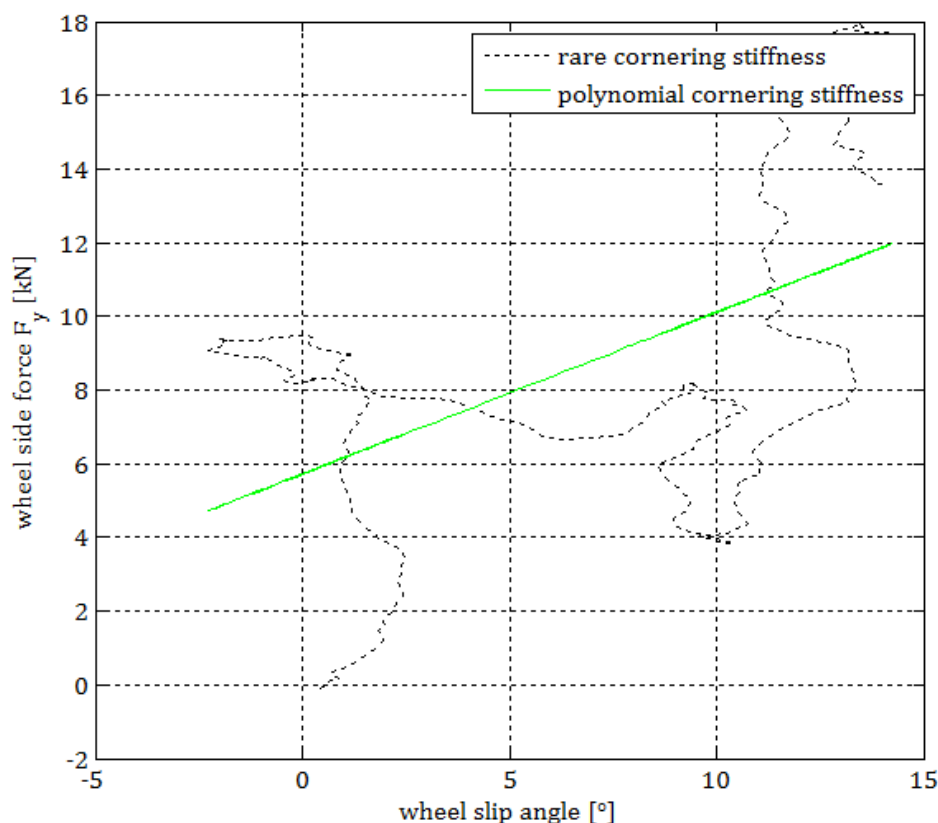
Figure 6.12 Test overview obtained within signals from test of cornering stiffness

The cornering stiffness was roughly the same as for test with velocity of *5 [km/h]* and *10 [km/h]*. However the initial offset (in the sense of wheel side force for zero degree of wheel slip angle) was even greater; see **Figure 6.12** and the factor c in equation 6.1. The reaction time and rising time of lateral wheel force was shorter because of higher rotation velocity than in case of test with of *5 [km/h]* and *10 [km/h];* see **Figure 6.11.**

$$y = 0.818 \left[\frac{kN}{°}\right] \cdot \alpha[°] + 2.14 \, [kN] \qquad\qquad [6.2]$$

The equation 6.2 represents the result of the step response of lateral force test for velocity of *15 [km/h]*.

In general, the results obtained in this research confirmed the functionality of the tire test method with mobile test rig and the wheel force sensor. In the test by free oscillations were measured three tire mechanical properties in vertical direction: spring constant, viscous damping and damping ratio. These properties were measured for front and rear tire in the velocity range from *5 km/h* to *20 km/h*. The results demonstrated that this kind of test can be conducted with one mobile test rig for different tire sizes under controlled and variable boundary conditions. The high reproducibility was reflected by three following properties:

- The symmetry acceleration converged to the value of $10\ [m/s^2]$ with increasing driving velocity.
- The acceleration amplitude increased with driving velocity.
- Roughly the same number of oscillations occurred within one driving velocity.

The accuracy of the results obtained by this method could be enhanced by greater number of test runs. The ramp used for excitation instead of square beam was deciding improvement in this method.

The test by random vibration proved the functionality of this method and the MTTR too. In this test were measured the same three tire mechanical properties in vertical direction: spring constant, viscous damping and damping ratio. These properties were measured for front and rear tire in the velocity range from *10 [km/h]* to *25 [km/h]*. The hypothesis that the tire mounted in the test frame and pulled on asphalt lane behind the tractor behaves as single DOF mass oscillator excited by random *Gaussian* vibrations was confirmed. This method introduced the statistical calculations of random process in time domain as: kurtosis, skewness and statistical error. These characteristics were neglected in other researchers using PSD for tire's identification. The analysis in time domain is crucial to monitor the signal quality. The dependency between the sampling frequency and sample duration and their influence by windowing, overlapping and averaging on the calculation error were presented in this research.

The test of step response of lateral force with its goal to define the tire-ground characteristics, verified the functionality of the mobile tire test rig and the wheel force sensor. The lateral tire force in function of wheel slip angle was measured in

transient states. The force measurement hub enabled to measure two forces F_{X_C}, F_{Y_C} and one moment M_{Y_C} in the wheel center. The design of the WFTMD made possible to mount original wheel rims of different sizes. This tire test method showed the possibility of defining tire cornering stiffness for transient states under different velocities. However, the cornering stiffness is subjected to the great inaccuracy because of wheel loads fluctuations. The test by random vibration and test of step response of lateral force showed very pointedly the demand for quite big test area with possible even road surface.

Chapter 7

7 Discussion

7.1 Comparison with other results from the past

The agricultural tires were investigated in vertical direction in test by free oscillation by few researchers as Langenbeck [18], Böhler [6]. However Langenbeck and Böhler did not used decaying acceleration in order to evaluate the test data. They calculated the vertical stiffness and damping by usage the force signal and the signal representing the dynamic radius. They did not define the accuracy of estimated tire parameters. According to those investigations the vertical tire stiffness stayed constant with increasing velocity [6, 12, 18]. The parameters obtained in this research for front tire by two methods the tendency of the vertical tire stiffness coincide with the findings of Langenbeck [18], Böhler [6] and Ulrich [44]. The parameters of rear tire do not coincide with the results from literature. That can be explained by the bad quality of the acceleration history for velocity of *10*, *15* and *20 [km/h]*. In the work of Ulrich it was pointed out that the stiffness increases with tire's deflection, what almost ten years later confirms Langenbeck. The results in this research were obtained by two different test method: test by free oscillation and random vibrations. The results for front tire confirm the tendency that the stiffness increases with tire's deflection.

Von Holst estimated vertical stiffness and damping ratio in test by free oscillation and using envelope curve. He used the signal of distance between the wheel axis and the surface instead of acceleration history. But the calculation of stiffness and viscous damping was exactly the same as the one described in the chapter 5.1.2. There was no accuracy analysis too. He determined the vertical stiffness and damping in function of velocity under different payload and tire inflate pressure. His tests confirmed that the stiffness is nearly constant for velocity up to *40 [km/h]* while the viscous damping is decreasing with rising velocity. Mr Langenbeck found

that the viscous damping decreases with increasing velocity. In his research the viscous damping starts from the value of *2.2 [kNs/m]* for *0 [km/h]* and falls down to zero by *40 [km/h]*. He strongly emphasized that the damping characteristic for higher velocity must increase in order to improve handling and the driving safety. Mr Böhler within test conducted on partly the same indoor test rigs discovered that the viscous damping falls rapidly for velocities *0 [km/h]* up to *10 [km/h]* and further lightly decreases to ca. *1000 [kNs/m]* for *60 [km/h].*

On the Berlin University of Technology there were researches that investigated the damping ratio and plotted it in function of velocity. The damping ration, according to Pickel [12], fell rapidly for velocities under *10 [km/h]* and further lightly decreased up to *50 [km/h]* to value ca. *0.02*. Quite similar course of damping ratio showed von Holst 2000 [14]. In general the range of stiffness, viscous damping and damping ratio correspond with the values found in works of Ulrich (1983) [44], Langenbeck (1991) [18], Pickel (1993) [12], von Holst (2000) [14] .

In general the ramp used for excitation instead of square beam and the fact that the test wheel was pulled in the frame behind the tractor on the asphalt lane was the crucial improvement in this method. The signal run for *20[km/h]* pointed out that the ramp shall be even longer. The length of the ramp shall be tuned so, that the energy needed to level up the test wheel was constant.

Mr von Holst determined the vertical stiffness and damping for small amplitudes in test by random stochastic excitation of the belt rig [14]. Because he had input and output signal he involved the magnificent function [3] instead of Aspinwall equivalency. He pointed out the filter width but neglected the statistical error of FFT function. Ulrich had used the equivalency of ideal filter to one dof mass oscillator and so he identified the tire parameters by analysing the PSD resonance peak. However, in many works using PSD calculation method to identify the parameter of mechanical system in wide sense there is habitual lack of information about statistical properties of the signal and also indicators of spectral accuracy as filter width and statistical error [6, 7, 12, 13, 31, 44]. Taking into account that the PSD estimation without averaging can be subjected to the error greater than *80%* [76],

---

[3] Called also Frequency Response Function

raises the question if tire parameters defined with this method were reliable. The origin of error of picket fence effect caused by discrete nature of the frequency spectrum has been described in the chapter 5.1.3.

7.2   Perspective for future research

The method of random vibrations offers great possibilities in term of defining the spring constant and viscous damping of the tire in vertical direction. This procedure enables to define the accuracy of measurement parameters. The signal properties in time domain enable to monitor the boundary conditions. This guarantees high reproducibility. The measurements and results obtained in different research centres could be compared with each other. This method is also attractive because it reveals new possibilities for measurement as the influence of wheel slip angle or wheel slip on the tire mechanical properties in vertical direction. Such disturbances are closely related to the wheel behaviour during critical road situations.

However, disposing only the output signal history it is possible to use only the first expression of transfer function $|H_1(f)|$. It can over or underestimate the real transfer function $H(f)$ according to signal-to-noise-ratios at input and response. Simultaneous measurement of the PSD of the test track would deliver the history of input signal. The new ways for data evaluation would be possible. This would significantly enhance this method in term of accuracy.
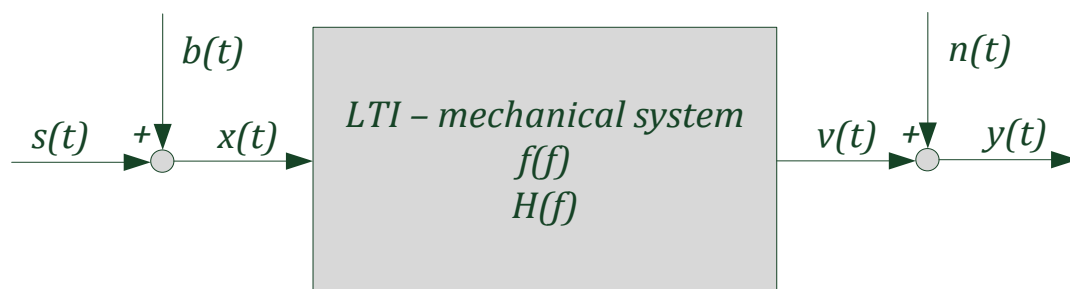
Figure 7.1 Time invariant single input single output linear system

The main reason why the signal in time domain is converted into frequency domain is that the relation between the input and output signal can by described by multiplication. Taking into account that the linear mechanical system undergoes the stationary random excitation signal $s(t)$ the response signal $v(t)$ is also stationary

random. In the absence of noise on input $b(t) = 0$ and noise on the response $n(t) = 0$, measured $x(t)$ and $y(t)$ are identical to $s(t)$ and $v(t)$ respectively

$$x(t) = s(t) + b(t)$$
$$y(t) = v(t) + n(t)$$

[7.1]

The graphical presentation of presence or absence of noise on the input and output signal is shown on the **Figure 7.1**.

If the $G_x(f)$ is one sided power spectral density of the input signal $x(t)$ and $G_y(f)$ is one sided power spectral density of the output signal $y(t)$. Their relationship is described by transfer function $H(f)$ by following equation:

$$G_y(f) = |H(f)|^2 G_x(f)$$

[7.2]

with usage of angular frequency, the expressions becomes:

$$G_y(f) = |H(j\Omega)|^2 G_x(f)$$

[7.3]

The expression [7.2] yields a first definition of the transfer function, which is often called $H_1(f)$:

$$|H_1(f)| = \sqrt{\frac{G_{yy}(f)}{G_{xx}(f)}}$$

[7.4]

The second and third definition of transfer function is described by application of one sided power spectral density of excitation or response (autospectrum) and (one sided) cross-power spectral density of excitation and response $G_{xy}(f)$:

$$G_{xy}(f) = H(f)G_{xx}(f)$$

[7.5]

and

$$G_{yy}(f) = H(f)G_{yx}(f).$$

[7.6]

The equation **[7.5]** and **[7.6]** yield second and third expression of transfer function:

$$H_2(f) = \frac{G_{xy}(f)}{G_{xx}(f)}$$

[7.7]

and

$$H_3(f) = \frac{G_{yy}(f)}{G_{yx}(f)}$$

[7.8]

These expressions **[7.4]**, **[7.7]** and **[7.8]** are theoretically the same as long as:

- the input $x(t)$ and output $y(t)$ signals have no noise;

- there is no other excitation contributing to the response $y(t)$;
- PSDs are calculated with a very low statistical error.

The output signal in this research consist other vibration sources coming from profile or even inhomogeneity of tire, rim or tire parameters along its circumference. Therefore it could be expected that the input and output signal are loaded by noise. Having synchronized in- and output there would be possible to monitor influence of noise. The magnitude of noise interrupting the excitation and response can be determined by *coherence function*

$$\gamma^2(f) = \frac{H_2(f)}{H_3(f)} \qquad\qquad [7.9]$$

For the coherence function $\gamma = 1$ there is no noise on the excitation and response of the linear system and all three definitions of transfer functions are equal:

$$|H_1(f)| = H_2(f) = H_3(f) \qquad\qquad [7.10]$$

The magnitude of noise can be checked by the *signal-to-noise-ratio (SNR)*:

$$R(f) = \frac{\gamma^2}{1-\gamma^2} \qquad\qquad [7.11]$$

However the input signal is absolutely needed in order to calculate the transfer function defined by second and third expression, the coherence function and signal-to-noise-ratio.

The attempt of using skid wheel in this research for measurement road PSD did not work because of several reasons. The skid wheel and the frame carrying the test wheel were mounted to the tractor that drives on the same road path. The roughness and all irregularities of asphalt lane excited the tractor, skid and test wheel. The vibrations were transferred to the constrain of the frame. Even the residual fluctuation of the distance between the road and tractor's body induced the force excitations because of the spring pushing the skid wheel against the surface. For that reason the skid wheel was not freely rolled on the asphalt lane where excited by unevenness but was excited by the force.

Chapter 8

8   Conclusion

As described in previous chapter, the results obtained in this research fit reasonably well into what other researchers in the field of large-volume tire testing have found. The three **test methods**:

- test by free oscillation,
- test by random vibration,
- step response of lateral force,

conducted with **mobile tire test rig** confirmed that it is possible to measure **tire parameters** as stiffness and viscous damping in vertical direction, and **tire-ground characteristics** with one device on rigid surface under different operation situation. This fact confirms the main part of research hypothesis about tire test method that bases upon quarter-vehicle. The measured forces and one torque verify the functionality of Wheel Force and Torque Measurement Device. The great advantage of the measurement hub is that different original wheel rims can be mounted without remanufacturing. However the performance of the measurement hub can be enhanced by applying force cells that are able to measure forces within three orthogonal directions. New force transducers and reliably sensor that measures directly the wheel rotation would simplify the calculation algorithm and enable to measure all six components in the wheel center.

The common conclusion out of three test methods is that one bigger test area is needed to conduct test effectively and with better quality. The longer test track would enable to conduct the test with higher velocities which was one part of the purpose in this research. The longer test track with smoother surface would enable to improve the accuracy of the parameters obtained within test by random vibration. The measurement of the PSD of the test track would enable a lot of new possibilities of increasing the accuracy, comparability and reproducibility. This

research reveals the necessity of introducing an attempt to define the accuracy for the parameters conducted in test by free oscillation. A bigger test area would enable to measure the tire-ground characteristics in velocities over *15 [km/h]* and in stationary states. The results of tire parameters in vertical direction imply that the mobile test rig can replace the indoor tire test facilities. The results of this research matter in regarding to three incoherencies mentioned in the chapter 1.1 concerning about motivation. This research can contribute in long term to help to:

- eliminate the gap between TM and TTM;
- merge various Test Methods into one that can be realized by one TTR delivering inputs for different types of TM;
- elaborate standardized tire test rig and benchmarking method.

However further improvement of tire test rig as design of lighter frame enabling wider range of weights for variable loads, better control of braking, steering and camber angle are necessary.

The significance of this research is even bigger when it is considered that more accurate Tire Models and reliable parameters that will be available in the future will enable for sophisticated vehicle dynamics analysis in early stage of tractor's design. Besides higher controllability and better handling they can become quicker and more productive by shortening the work cycle in general.

9   Bibliography

[1]   Health and Safety Executive, "Using tractors safely", Safety Instruction, UK, 2013

[2]   European Agency for Safety and Health at Work, "Directive 2002/44/EC - vibration"

[3]   S. Hammes, "Analytische und experimentelle Untersuchungen zur Fahrdynamik bei Ackerschleppern mit Niederquerschnittsreifen," Fachhochschule Köln, 2007

[4]   K. Armbruster, "Untersuchung der Kräfte an schräglaufenden angetrienen Ackerschlepperrädern," Hohenheim, 1991

[5]   B. Ferhadbegovic, "Entwicklung und Applikation eines instationären Reifenmodells zur Fahrdynamiksimulation von Ackerschleppern," Universität Stuttgart, 2008

[6]   H. Böhler, "Traktormodell zur Simulation der dynamischen Belastungen bei Transportfahrten," Technische Universität München, 2001

[7]   B. Thomas, "Konzeption und Simulation eines passiven Kabinenfederungssystems für Traktoren," Technische Universität Carolo-Wilhelmina, 2001

[8]   I. Sharon, "Untersuchungen über die Schwingungseigenschaften großvolumiger Niederdruckreifen," Technische Universität Berlin, 1975

[9]   A. Kising, "Dynamische Eigenschaften von Traktor-Reifen," Technische Universität Berlin, 1988

[10]   A. Kising and H. Göhlich, "Dynamic Characteristics of Large Tyres," *Br. Soc. Res. Agric. Eng.*, pp. 11–21, 1989

[11]   T. Siefkes, "Die Dynamik in der Kontaktfläche von Reifen und Fahrbahn und ihr Einfluß auf das Verschleißverhalten von Traktor-Triebradreifen," Technische Universität Berlin, 1993

[12]   P. Pickel, "Simulation fahrdynamischer Eigenschaften von Traktoren," Technische Universität Berlin, 1993

[13]   C. Kaplick, "Verifikation und Bewertung fahrdynamischer Traktor fahrdynamischer Traktorsimulationsmodelle," Technische Universität Berlin, 1995

[14]   C. von Holst, "Vergleich von Reifenmodellen zur Simulation der Fahrdynamik von Traktoren," Technischen Universität Berlin, 2000

[15] H. Pacejka, *Tyre and Vehicle Dynamics*, Delft University of Technology, 2006

[16] P. Zegelaar and H. Pacejka, "The In-Plane Dynamics of Tyres on Uneven Roads," *Vehicle System Dynamics*, 1996

[17] H. Schrogl, "Dynamische Eigenschaften von Ackerschlepper-Triebradreifen bei höheren Rollgeschwindigkeiten," Universität Hohenheim, 1989

[18] B. Langenbeck, "Untersuchungen zum Fahrverhalten von Ackerschleppern unter besonderer Berücksichtigung der Reifeneigenschaften," Hohenheim, 1991

[19] J. Plesser, "Dynamisches Verhalten von Ackerschlepperreifen in Vertikal- und Längsrichtung auf fester Fahrbahn," Universität Hohenheim, 1997

[20] A. Heine, "Experimenteller Beitrag zum Schräglauf- und Lenkmomentverhalten rollender Reifen landwirtschaftlicher Fahrzeuge auf starrer Fahrbahn und nachgiebiger Fahrbahn," Universität Stuttgart, 1991

[21] T. Barrelmeyer, "Untersuchung der Kräfte an gelenkten und angetriebenen Ackerschlepperrädern bei Gelände- und Straßenfahrt," Stuttgart, 1996

[22] V. Schlotter, "Einfluss dynamischer Radlastschwankungen und Schräglaufwinkeländerungen auf die horizontale Kraftübertragung von Ackerschlepperreifen," Universität Stuttgart, 2005

[23] C. Brinkmann, V. Schlotter, and B. Ferhadbegovic, "Untersuchungen zur Verschiebung des Aufstandspunktes für angetriebene Reifen," in *Landtechnik Tagung*, 2005

[24] C. Brinkmann, B. Ferhadbegovic, and J. Haberland, "Investigation on Agricultural Tyres - Test Stands and Results"

[25] B. Ferhadbegovic, S. Böttinger, and H. D. Kutzbach, "Mehrkörpersimulation in der Fahrdynamik von Ackerschleppern." Universität Hohenheim, Hohenheim, 2007

[26] B. Ferhadbegovic, S. Böttinger, and H. D. Kutzbach, "Handling Analysis of Agricultural Tractors Using Multi-Body Simulation," *VDI Conference - Agritechnika*, 2007

[27] B. Ferhadbegovic, C. Brinkmann, and J. Haberland, "Hohenheimer Reifenmodell - Basis für ein instationäres Fahrzeugmodell" Universität Hohenheim

[28] B. Ferhadbegovic, C. Brinkmann, H. D. Kutzbach, and S. Böttinger, "Hohenheimer Reifenmodell – ein dynamisches dreidimensionales Modell für Fahrdynamiksimulation," *Agric. Eng. Res.*, vol. 1, 2007

[29] B. Ferhadbegovi, C. Brinkmann, H. D. Kutzbach, S. Böttinger, B. Ferhadbegovic', and B. Ferhadbegovic, "Hohenheim Tyre Model - A Dynamic Model for Agricultural Tyres," in *Proceedings of the 16th CIGR World Congress*, 2006

[30] B. Ferhadbegovic, H. D. Kutzbach, and S. Böttinger, "A Multi-Body Model of an Agricultural Tractor for Driving Dynamics Analysis." ISTVS, 2007

[31] J. W. Betzler, "Verfahren zur Beschreibung schneller ungefederter Radfahrzeuge hinsichtlich Fahrverhalten und Fahrbahnbelastung," Technische Hochschule Darmstadt, 1989

[32] K. U. Wermann, "Ein Beitrag zum Straßenfahrverhalten ungefederter schnellfahrender Radfahrzeuge unter besonderer Berücksichtigung der querdynamischen Fahrzeug- und Reifeneigenschaften," Technische Hochschule Darmstadt

[33] B. Ferhadbegovi, C. Brinkmann, and H. D. Kutzbach, "Dynamic Longitudinal Model for Agricultural Tyres," in *Proceedings of the 15th International Conference of the ISTVS*, 2005

[34] J. Dunlop, W. Gordon, D. Gentz, and E. Schuch, "Tire Research Facility (TIRF)," Buffalo, NY, 2008

[35] MTS, "Flat-Trac Tire Test Systems," Catalog, 2013

[36] H. Wallentowitz, "Tire technology – Simulation und Testing," Aachen, 2006

[37] MTS, "The Rolling Resistance Measurement System" MTS, Eden Prairie, 2007

[38] M. Meywerk, "Dynamische Reifenprüfanlage," IFAS, Helmut-Schmidt Universität, Universität der Bundeswehr Hamburg, 2009

[39] J. Ejsmont, J. Jackowski, W. Luty, G. Motrycz, P. Stryjek, and B. Swieczko-Żurek, "Analysis of Rolling Resistance of Tires with Run Flat Insert," *Key Eng. Mater.*, vol. 597, Dec. 2013

[40] BASt, "BASt - Presse - BASt-Prüfstand dreht sich wieder" [Online]. Available: http://www.bast.de/DE/Presse/2007/presse-04-2007.html. [Accessed: 25-Jun-2014]

[41] W. Seibert, "Anwendungszentrum Automobiltechnik," Hochschule für Technik und Wirtschaft des Saarlandes, Forschungsbericht, Saarland, 2001

[42] DeVetec, "Mobiler Messanhänger - BERTA", Brochure, 2001

[43] A. Rehnberg, "Suspension design for off-road construction machines," Royal Insitute of Technology, Doctoral Thesis, 2011

[44] A. Ulrich, "Untersuchungen zur Fahrdynamik von Traktoren mit und ohne Anbaugeräte," Technische Universität Berlin, Berlin, 1983

[45] S. Solyom, "Synthesis of a Model-based Tire Slip Controller," Departament of Automatic Control, Lund Institute of Technology, Lund Sweden, 2002

[46] M. Beato, V. Ciaravola, M. Russo, and A. Volpe, "Lateral Tyre Force by a Milliken Test on a Flat Track Roadway Simulator," *Veh. Syst. Dyn.*, no. 912873516, 2010

[47] M. Göbel, "Potenzial der Radkraftmessung für fahrdynamische Regelsysteme," Technischen Universität Braunschweig, Aachen, 2009

[48] Kistler, "Wheel Force Measurement - RoaDyn Measuring wheels and measuring hubs for every application," Catalog, 2010

[49] MTS, "Spinning Wheel Integrated Force Transducer," White Paper, 2012

[50] PCB, "Multi-Axis Wheel Force Transducer," White Paper, 2012

[51] Kistler and D. Barz, "High End Engineering for Crash Barriers and Measuring Wheels," *Vehicle News*, 2007

[52] M. Sayers, "Standard Terminology for Vehicle Dynamics Simulations," University of Michigan Transportation Research Institute, 1996

[53] H. Unrau, J. Zamow, "TYDEX-Format," Reference Manual, Release 1.3, 1997

[54] R. Just, "Konstruktion einer 6-Komponenten-Menabe für den Hinterachsantrieb eines Ackerschleppers," Technischen Universität Berlin, 1980

[55] D. L. Hoag and R. R. Yoerger, "Designing load rings for measurment," *Trans. ASAE*, 1974

[56] D. L. Hoag and R. R. Yoerger, "Analysis and design of load rings," *Trans. ASAE*, 1975

[57] HBM, "Strain Gages and Accessories," Catalog, 2008

[58] P. Sarantopoulos, "Optimierung und Inbetriebnahme einer Halterung zum Kalibrieren einer Sechs-Komponenten-Messnabe," Semesterarbeit, Fachhochschule Köln, 2010

[59] M. Thiele, "Konstruktion und Inbetriebnahme eines Rahmens zur Kalibrierung einer Sechs-Komponenten-Messnabe," Semesterarbeit, Fachhochschule Köln, 2010

[60] M. Stockhorst, "Neukonstruktion einer mobilen Reifenmesseinrichtung zur Untersuchung der auftretenden Radkräfte in kritischen Fahrsituationen," Diplomarbeit, Fachhochschule Köln, 2010

[61] Reimpell, "Vertikaldynamik," Vorlesungsskript, 2008

[62] R. Colusso, "Simulationsmodell eines Fahrzeuges," FH Lippe, 2011

[63] K. Centkowski, "Vorgehensweise zur Identifikation von wichtigen Fahrzeugparametern bei einer mobilen Arbeitsmaschine", Technische Universität Warschau, 2008

[64] Shipping International, "Determination of Center of Balance and Center of Gravity" Regulation

[65] R. Isermann, "*Fahrdynamik-Regelung,*" Vieweg, 2006

[66] G. Rill, *"Vehicle Dynamics",* vol. 504, no. 7478. 2013

[67] W. F. Milliken and D. L. Milliken, "*Race Car Vehicle Dynamics,*" SAE International, 1995

[68] L. Strandberg, "Danger, Rear Wheel Steering," *J. Occup. Accid.*, vol. 5, pp. 39–58, 1983

[69] P. H. Wirsching, T. L. Paez, and K. Ortiz, "*Random Vibrations, Theory and Practice,*" John Wiley & Sons, Inc, 1995

[70] M. Knaeble, H. Jäger, and R. Mastel, *"Technische Schwingungslehre,"* 6th ed. Wiesbaden: Teubner, 2006

[71] C. Lalanne, "*Mechanical Vibration and Shock Analysis, Mechanical Shock" (Volume 2)*, Wiley-ISTE, 2009

[72] H. Schmid, "How to use the FFT and Matlab's pwelch function for signal and noise simulations and measurements," vol. 2012, no. August, 2012

[73] A. Preumont, "*Solid Mechanics and its Applications, Random Vibration and Spectral Analysis,*" vol. 33. Bruxelles, Belgium: Kulwer Academic Publishers, 1994

[74] Michelin, "Michelin Agricultare and Compact Line," Michelin, 2012

[75] Michelin, "Betriebsanleitung Landwirtschaftsreifen," 2006

[76] C. Lalanne, "*Mechanical Vibration and Shock Analysis, Random Vibration" (Volume 3)*, vol. 3. ISTE Ltd, 2009

Appendix A

A.1 Structural model of single load ring

The reaction forces occurring in the circular portion of the load ring:

Normal (horizontal) reaction forces

$$N_r = \frac{F_x}{2} \tag{A.1}$$

$$N_l = -\frac{F_x}{2} \tag{A.2}$$

Cross (vertical) reaction forces

$$V_r = -\frac{F_y}{2} - \frac{M_0 \cdot \left(\frac{2}{L} + \frac{\pi}{R}\right)}{\left(8 + \frac{R \cdot \pi}{L} + \frac{2 \cdot L \cdot \pi}{R}\right)} \tag{A.3}$$

$$V_l = \frac{F_y}{2} - \frac{M_0 \cdot \left(\frac{2}{L} + \frac{\pi}{R}\right)}{\left(8 + \frac{R \cdot \pi}{L} + \frac{2 \cdot L \cdot \pi}{R}\right)} \tag{A.4}$$

Bending moments at the top of the beams:

Portion on the right hand side

$$M_r = \frac{F_x \cdot R}{2} + \frac{F \cdot R}{\pi} + \frac{M_0 \cdot \left(2 + \frac{R \cdot \pi}{2 \cdot L}\right)}{\left(8 + \frac{R \cdot \pi}{L} + \frac{2 \cdot L \cdot \pi}{R}\right)} \tag{A.5}$$

Portion on the left hand side

$$M_l = -\frac{F_x \cdot R}{2} + \frac{F \cdot R}{\pi} - \frac{M_0 \cdot \left(2 + \frac{R \cdot \pi}{2 \cdot L}\right)}{\left(8 + \frac{R \cdot \pi}{L} + \frac{2 \cdot L \cdot \pi}{R}\right)} \tag{A.6}$$

The horizontal deflection is equal on the left and right hand side:

$$\delta_x = \delta_{xl} = \delta_{xr} \tag{A.7}$$

$$\delta_{xr} = \frac{R^2}{E \cdot I} \cdot \left(-\frac{F_x \cdot R \cdot \pi}{4} + \frac{\frac{M_0 \cdot R \cdot \pi}{L} \cdot \left(\frac{\pi}{2} - \frac{4}{\pi}\right)}{\left(8 + \frac{R \cdot \pi}{L} + \frac{2 \cdot L \cdot \pi}{R}\right)} \right) \tag{A.8}$$

The vertical deflection is different on the left and right hand side:

$$\delta_{yr} = \frac{R^2}{E \cdot I} \cdot \left(F_y \cdot R \cdot \left(\frac{2}{\pi} - \frac{\pi}{4}\right) + \frac{M_0 \cdot \left(4 - \frac{\pi^2}{2}\right)}{\left(8 + \frac{R \cdot \pi}{L} + \frac{2 \cdot L \cdot \pi}{R}\right)} \right) \qquad \text{[A.9]}$$

$$\delta_{yl} = \frac{R^2}{E \cdot I} \cdot \left(F_y \cdot R \cdot \left(\frac{2}{\pi} - \frac{\pi}{4}\right) - \frac{M_0 \cdot \left(4 - \frac{\pi^2}{2}\right)}{\left(8 + \frac{R \cdot \pi}{L} + \frac{2 \cdot L \cdot \pi}{R}\right)} \right) \qquad \text{[A.10]}$$

The deflection in the loading point equals:

$$\delta_y = \frac{R^2}{E \cdot I} \cdot \left(F_y \cdot R \cdot \left(\frac{2}{\pi} - \frac{\pi}{4}\right) \right) \qquad \text{[A.11]}$$

The rotation is equal on the left and right hand side

$$\omega_l = \omega_r \qquad \text{[A.12]}$$

$$\omega_r = \frac{R \cdot M_0}{E \cdot I} \cdot \left(\frac{\frac{R \cdot \pi}{L} \cdot \left(\frac{\pi}{2} - \frac{4}{\pi}\right)}{\left(8 + \frac{R \cdot \pi}{L} + \frac{2 \cdot L \cdot \pi}{R}\right)} \right) \qquad \text{[A.13]}$$

Finally the equation of bending moment lets quantify stress distribution. For that reason it should be checked as the first output because it determines if the load ring holds out the external loads.

The equation of bending moment in the right circular portion of load ring:

for interval $0 < \varphi < \pi$

$$M_\varphi = \frac{F_y \cdot R}{2} \cdot \left(\frac{2}{\pi} - \sin(\varphi)\right) + \frac{F_x \cdot R}{2} \cdot \cos(\varphi) + \frac{M_0 \left[\left(2 + \frac{R \cdot \pi}{2 \cdot L}\right) - \left(\frac{2 \cdot R}{L} + \pi\right) \cdot \sin(\varphi)\right]}{\left(8 + \frac{R \cdot \pi}{L} + \frac{2 \cdot L \cdot \pi}{R}\right)} \qquad \text{[A.14]}$$

The equation of bending moment in the left circular portion of load ring:

for interval $\pi < \varphi < 2 \cdot \pi$

$$M_\varphi = \frac{F_y \cdot R}{2} \cdot \left(\frac{2}{\pi} - \sin(\varphi)\right) - \frac{F_x \cdot R}{2} \cdot \cos(\varphi) - \frac{M_0 \left[\left(2 + \frac{R \cdot \pi}{2 \cdot L}\right) - \left(\frac{2 \cdot R}{L} + \pi\right) \cdot \sin(\varphi)\right]}{\left(8 + \frac{R \cdot \pi}{L} + \frac{2 \cdot L \cdot \pi}{R}\right)} \qquad \text{[A.15]}$$

A.2 Technical drawing of single load ring
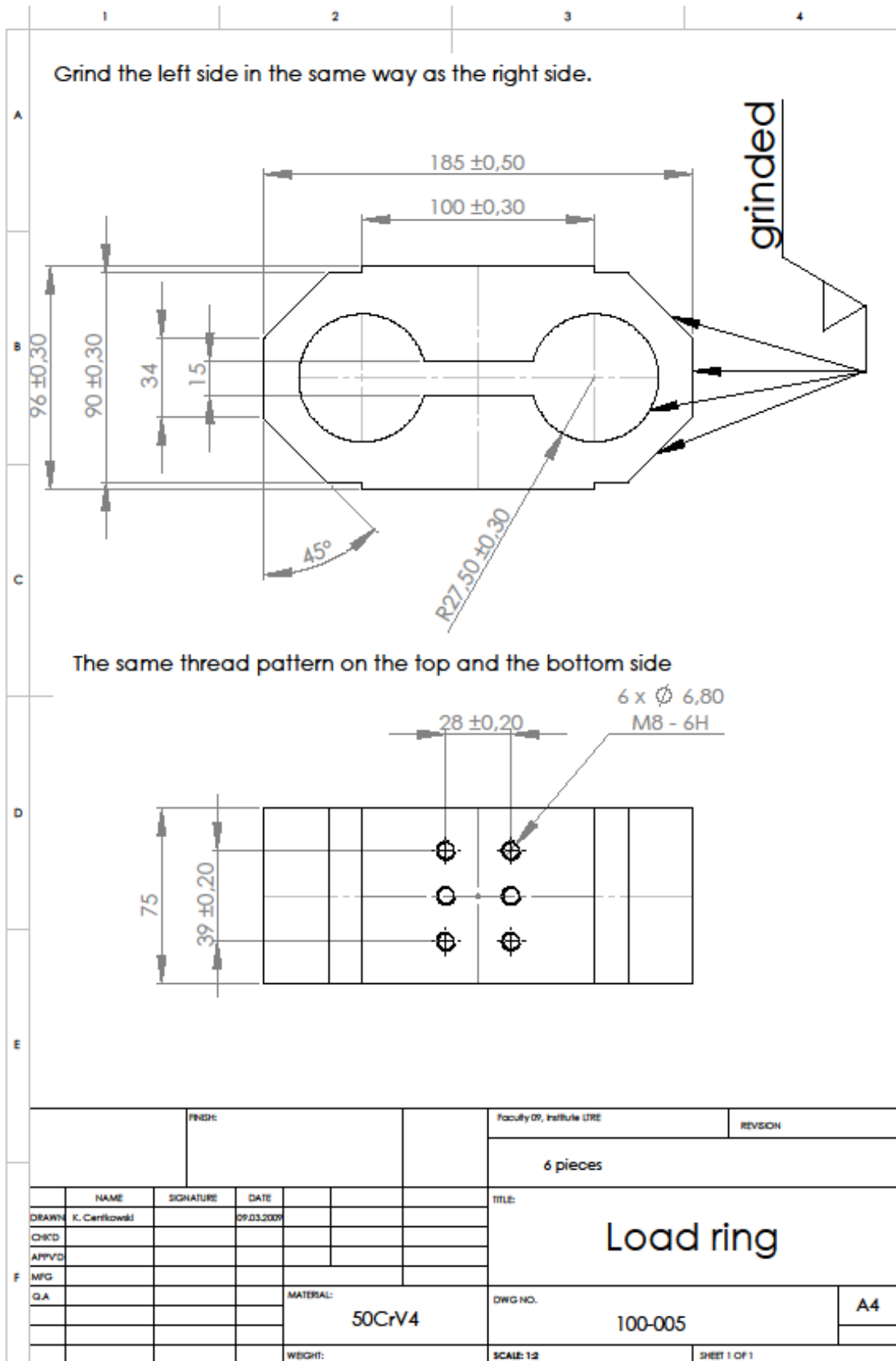
A.3 Technical data of strain gauges

LG 11 - linear strain gage [57]

Temperature response matched to the thermal expansion coefficient for ferritic steel $\alpha = 10.8 \cdot 10^{-6}/K$

Strain gage description			1-LG11-6/350
Nominal resistance		$[\Omega]$	350
Dimmensions [mm]	Measuring grid	a - length	6
		b - width	2.9
	Measuring grid carrier	c - length	13
		d - width	6
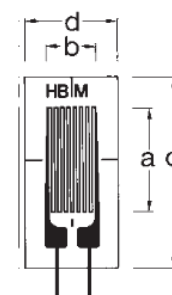
The series G of strain gages with one measuring grid is dedicated for the manufacture of transducers. The result of measurements using strain gages is the mean value of the strains underneath the measuring grid. For that reason the measuring grid length of *6 [mm]* provide good solution. Measuring grid is made of constantan foil. Carrier and cover are made of glass fiber reinforced with phenolic resin. Gage factor equals approx. *2*. The minimum radius of curvature equals *3 [mm]*. The inner surface of load ring has radius of *27.5 [mm]* so the body of transducer is appropriate for this strain gage series.

A.4 Calibration data

Table A.1: Calibration data of transducer *ay*

1	2	3	4	5	6	7
input ay_{ref} [kN]	output ax [mV]	**output ay [mV]**	cross-over talk [%]	ay y=13.584x [kN]	difference [kg]	linearity [%]
-7,9	-0,01	**-0,62**	1,8%	-8,4	**-50,8**	-5,9%
-7,1	0,01	**-0,55**	-1,6%	-7,5	**-44,0**	-5,8%
-6,1	-0,01	**-0,47**	1,7%	-6,4	**-36,6**	-5,6%
-5,0	-0,01	**-0,39**	1,5%	-5,3	**-28,8**	-5,3%
-4,0	0,00	**-0,31**	1,3%	-4,2	**-23,2**	-5,4%
-3,0	0,00	**-0,23**	1,3%	-3,2	**-15,9**	-4,9%
-2,0	0,00	**-0,16**	0,6%	-2,1	**-10,6**	-4,9%
-1,0	0,00	**-0,08**	1,3%	-1,1	**-5,3**	-4,8%
0,0	0,00	**0,00**	0,0%	0,0	**0,7**	-
1,0	0,00	**0,08**	2,5%	1,1	**5,8**	-5,2%
2,0	0,00	**0,16**	1,9%	2,1	**7,9**	-3,6%
3,0	0,01	**0,23**	2,2%	3,1	**7,0**	-2,2%
4,1	0,01	**0,31**	2,3%	4,1	**6,3**	-1,5%

5,0	0,01	**0,37**	2,4%	5,1	**5,4**	-1,1%
6,1	0,01	**0,45**	2,4%	6,2	**6,5**	-1,0%
7,1	0,01	**0,52**	2,3%	7,1	**5,0**	-0,7%
8,1	0,01	**0,60**	2,2%	8,1	**1,9**	-0,2%
9,1	0,01	**0,67**	2,1%	9,1	**0,3**	0,0%
10,2	0,02	**0,75**	2,0%	10,1	**-1,8**	0,2%
12,1	0,02	**0,89**	1,8%	12,0	**-6,4**	0,5%
14,1	0,02	**1,03**	1,8%	14,0	**-11,1**	0,8%
16,1	0,02	**1,17**	1,8%	15,9	**-17,8**	1,1%
18,1	0,02	**1,31**	1,8%	17,8	**-23,3**	1,3%
20,1	0,03	**1,46**	1,8%	19,8	**-28,6**	1,4%

Table A.2: Calibration data of transducer cx

1	2	3	4	5	6	7
input	**output**	output	cross-over	cx	difference	linearity
cx_{ref}	**cx**	cy	talk	y=10.646x		
[kN]	**[mV]**	[mV]	[%]	[kN]	[kg]	[%]
-19,9	**-1,9**	-0,1	6,0%	-20,1	**-25,4**	-1,2%
-18,0	**-1,7**	-0,1	6,4%	-18,3	**-26,6**	-1,4%
-16,1	**-1,5**	-0,1	6,8%	-16,3	**-26,7**	-1,6%
-14,1	**-1,3**	-0,1	7,4%	-14,3	**-26,8**	-1,8%
-12,0	**-1,2**	-0,1	7,9%	-12,3	**-27,8**	-2,2%
-10,0	**-1,0**	-0,1	8,0%	-10,7	**-64,0**	-5,9%
-9,1	**-0,9**	0,0	5,6%	-9,4	**-31,0**	-3,3%
-8,0	**-0,8**	0,0	6,0%	-8,3	**-32,1**	-3,8%
-7,0	**-0,7**	0,0	6,2%	-7,4	**-38,3**	-5,1%
-6,1	**-0,6**	0,0	6,0%	-6,4	**-32,7**	-5,0%
-5,0	**-0,5**	0,0	4,6%	-5,3	**-33,4**	-6,1%
-4,0	**-0,4**	0,0	1,7%	-4,4	**-34,9**	-7,8%
-3,1	**-0,3**	0,0	-2,5%	-3,4	**-34,7**	-10,0%
-2,0	**-0,2**	0,0	-9,8%	-2,4	**-36,2**	-14,8%
-0,8	**-0,1**	0,0	-35,1%	-1,2	**-34,8**	-28,9%
0,1	**0,0**	0,0	-167,9%	-0,3	**-35,5**	-
1,0	**0,1**	0,0	60,9%	0,7	**-33,3**	47,9%
2,0	**0,2**	0,0	18,8%	1,7	**-34,8**	20,1%
3,1	**0,3**	0,0	7,5%	2,7	**-35,4**	12,8%
4,1	**0,3**	0,0	2,3%	3,7	**-35,2**	9,3%
5,0	**0,4**	0,0	-0,7%	4,6	**-34,5**	7,3%
6,0	**0,5**	0,0	-2,8%	5,7	**-33,6**	5,8%
7,0	**0,6**	0,0	-4,3%	6,7	**-34,2**	5,0%
8,0	**0,7**	0,0	-5,1%	7,7	**-33,5**	4,3%
9,0	**0,8**	0,0	-5,9%	8,6	**-36,2**	4,1%
10,1	**0,9**	-0,1	-6,5%	9,7	**-32,6**	3,3%
11,9	**1,1**	-0,1	-7,2%	11,5	**-35,2**	3,0%
14,2	**1,3**	-0,1	-7,8%	13,9	**-33,5**	2,4%
16,2	**1,5**	-0,1	-8,3%	15,9	**-33,4**	2,1%
18,2	**1,7**	-0,1	-8,5%	17,9	**-34,3**	1,9%
20,1	**1,9**	-0,2	-8,8%	19,8	**-34,8**	1,7%

Table A.3: Calibration data of transducer *cy*

1	2	3	4	5	6	7
input	output	output	cross-over	*cy*	difference	linearity
cy_{ref}	*cx*	*cy*	talk	y=13.256x		
[kN]	[mV]	[mV]	[%]	[kN]	[kg]	[%]
-6,0	-0,03	-0,42	7,4%	-5,6	47,5	8,4%
-5,0	-0,03	-0,34	8,8%	-4,5	51,1	11,1%
-4,0	-0,03	-0,26	10,7%	-3,5	55,5	15,7%
-3,1	-0,03	-0,19	14,4%	-2,5	58,2	23,0%
-2,0	-0,03	-0,11	23,1%	-1,4	62,0	42,5%
-1,0	-0,02	-0,03	82,8%	-0,4	64,0	163,3%
0,0	-0,02	0,05	-46,0%	0,7	66,7	-
1,2	-0,02	0,14	-15,4%	1,8	64,8	-35,3%
2,1	-0,02	0,20	-10,0%	2,7	62,6	-23,1%
3,1	-0,02	0,27	-6,9%	3,6	59,3	-16,0%
4,1	-0,02	0,35	-5,2%	4,6	54,7	-11,7%
5,1	-0,02	0,42	-4,1%	5,6	48,8	-8,6%
6,1	-0,02	0,50	-3,2%	6,6	42,8	-6,4%
7,1	-0,02	0,56	-2,9%	7,4	38,0	-5,0%
8,0	-0,02	0,63	-2,4%	8,4	31,2	-3,7%
9,2	-0,01	0,71	-2,0%	9,4	24,0	-2,5%
10,1	-0,01	0,77	-1,6%	10,2	18,1	-1,7%
12,0	-0,01	0,91	-1,1%	12,1	8,6	-0,7%
14,0	-0,01	1,06	-0,7%	14,0	-4,2	0,3%
16,0	0,00	1,20	-0,3%	15,9	-14,9	0,9%
18,1	0,00	1,35	-0,1%	17,8	-28,8	1,6%
19,1	0,00	1,42	0,0%	18,8	-34,4	1,8%

Table A.4: Calibration data of transducer *ex*

1	2	3	4	5	6	7
input	**output**	output	cross-over	*ex*	difference	linearity
ex_{ref}	**ex**	*ey*	talk	y=10.516x		
[kN]	**[mV]**	[mV]	[%]	[kN]	[kg]	[%]
-20,0	**-1,94**	-0,12	6,4%	-20,42	**-42,5**	-2,0%
-18,1	**-1,76**	-0,12	6,7%	-18,51	**-42,6**	-2,3%
-16,0	**-1,56**	-0,11	7,2%	-16,45	**-43,0**	-2,6%
-14,1	**-1,38**	-0,11	7,6%	-14,47	**-42,8**	-2,9%
-12,1	**-1,19**	-0,10	8,0%	-12,51	**-43,0**	-3,4%
-10,0	**-1,00**	-0,08	7,9%	-10,46	**-43,4**	-4,1%
-9,1	**-0,90**	-0,07	7,9%	-9,49	**-44,4**	-4,6%
-8,0	**-0,80**	-0,06	7,5%	-8,43	**-42,4**	-4,9%
-7,0	**-0,71**	-0,05	6,9%	-7,45	**-44,9**	-5,9%
-6,1	**-0,62**	-0,04	6,0%	-6,49	**-44,7**	-6,8%
-5,0	**-0,52**	-0,03	5,0%	-5,48	**-45,8**	-8,2%
-4,1	**-0,43**	-0,02	3,5%	-4,54	**-45,9**	-9,9%
-3,1	**-0,34**	-0,01	1,5%	-3,52	**-46,2**	-12,9%
-2,1	**-0,24**	0,00	1,3%	-2,52	**-46,3**	-18,0%
-1,1	**-0,15**	0,01	-9,6%	-1,54	**-46,9**	-30,0%

0,0	**-0,05**	*0,02*	*-35,4%*	-0,50	**-46,7**	-
1,0	**0,05**	*0,01*	*25,9%*	0,57	**-47,1**	81,4%
2,0	**0,15**	*0,01*	*5,4%*	1,57	**-47,2**	29,6%
3,0	**0,25**	*0,00*	*-1,6%*	2,59	**-46,9**	17,8%
4,0	**0,34**	*-0,02*	*-4,4%*	3,58	**-47,4**	13,0%
5,1	**0,44**	*-0,03*	*-6,2%*	4,62	**-47,2**	10,0%
6,0	**0,53**	*-0,04*	*-7,0%*	5,56	**-47,6**	8,4%
7,0	**0,63**	*-0,05*	*-7,8%*	6,58	**-46,6**	6,9%
8,1	**0,72**	*-0,07*	*-9,7%*	7,60	**-48,3**	6,2%
9,0	**0,81**	*-0,07*	*-9,1%*	8,52	**-49,1**	5,7%
10,1	**0,91**	*-0,08*	*-9,2%*	9,59	**-47,3**	4,8%
12,0	**1,10**	*-0,11*	*-9,7%*	11,52	**-49,4**	4,2%
14,1	**1,30**	*-0,13*	*-9,9%*	13,64	**-49,0**	3,5%
16,1	**1,48**	*-0,15*	*-10,2%*	15,60	**-46,4**	2,9%
18,1	**1,68**	*-0,17*	*-10,3%*	17,61	**-45,4**	2,5%
20,2	**1,87**	*-0,20*	*-10,5%*	19,68	**-52,5**	2,6%

Table A.5: Calibration data of transducer *ey*

1	2	3	4	5	6	7
input ey_{ref} [kN]	output ex [mV]	**output ey [mV]**	cross-over talk [%]	ey $y=13.653x$ [kN]	difference [kg]	linearity [%]
-6,1	-0,04	**-0,46**	8,2%	-6,3	**-24,6**	3,8%
-5,0	-0,04	**-0,38**	9,7%	-5,2	**-19,6**	3,7%
-4,0	-0,04	**-0,30**	11,8%	-4,2	**-13,3**	3,1%
-3,0	0,04	**-0,23**	-15,9%	-3,1	**-8,1**	2,6%
-2,0	-0,04	**-0,15**	23,5%	-2,0	**-3,0**	1,4%
-1,0	-0,04	**-0,07**	47,3%	-1,0	**3,0**	-2,9%
0,2	-0,04	**0,02**	-194,4%	0,2	**9,6**	-
1,2	-0,04	**0,10**	-37,1%	1,3	**16,4**	12,2%
2,0	-0,04	**0,16**	-21,6%	2,2	**17,2**	7,6%
3,0	-0,03	**0,24**	-14,5%	3,2	**17,2**	5,3%
4,0	-0,03	**0,31**	-11,1%	4,2	**16,8**	3,9%
5,0	-0,03	**0,38**	-8,9%	5,2	**14,6**	2,8%
6,0	-0,04	**0,45**	-7,7%	6,2	**14,8**	2,3%
7,0	-0,04	**0,52**	-6,7%	7,1	**11,3**	1,5%
8,0	-0,04	**0,60**	-5,9%	8,1	**9,9**	1,2%
9,0	-0,04	**0,67**	-5,6%	9,1	**7,4**	0,8%
10,0	-0,04	**0,74**	-5,0%	10,0	**4,3**	0,4%
12,0	-0,04	**0,88**	-4,2%	12,1	**5,0**	0,4%
14,1	-0,04	**1,03**	-3,5%	14,1	**-5,0**	-0,3%
16,0	-0,04	**1,17**	-3,1%	15,9	**-10,9**	-0,7%
18,1	-0,04	**1,31**	-2,7%	17,9	**-18,4**	-1,0%
20,0	-0,04	**1,45**	-2,4%	19,8	**-22,8**	-1,1%

Table A.6: Calibration data of transducer *fx*

1	2	3	4	5	6	7
input fx_{ref} [kN]	**output fx [mV]**	output fy [mV]	cross-over talk [%]	fx y=10.506x [kN]	difference [kg]	linearity [%]
-18,1	**-1,71**	-0,15	8,9%	-18,0	**6,5**	0,4%
-15,4	**-1,46**	-0,13	8,8%	-15,3	**3,9**	0,2%
-12,8	**-1,23**	-0,11	8,6%	-12,9	**-5,8**	-0,4%
-10,2	**-0,97**	-0,08	8,7%	-10,2	**-0,7**	-0,1%
-7,5	**-0,71**	-0,05	7,6%	-7,5	**-5,2**	-0,7%
-5,2	**-0,50**	-0,04	7,6%	-5,2	**-1,5**	-0,3%
-2,4	**-0,23**	0,00	0,3%	-2,4	**-3,9**	-1,6%
-1,3	**-0,13**	0,00	2,4%	-1,3	**-1,6**	-1,1%
1,7	**0,17**	-0,01	-4,2%	1,8	**2,0**	-1,1%
2,9	**0,28**	-0,01	-3,6%	2,9	**2,0**	-0,7%
6,0	**0,57**	-0,05	-8,2%	6,0	**2,2**	-0,4%
9,5	**0,90**	-0,08	-8,5%	9,5	**4,4**	-0,5%
12,3	**1,16**	-0,10	-9,0%	12,2	**-8,6**	0,7%
15,9	**1,52**	-0,16	-10,2%	15,9	**2,8**	-0,2%
18,6	**1,78**	-0,17	-9,7%	18,7	**8,2**	-0,4%
21,7	**2,06**	-0,20	-9,9%	21,6	**-6,0**	0,3%

Table A.7: Calibration data of transducer *fy*

1	2	3	4	5	6	7
input fx_{ref} [kN]	output fx [mV]	**output fy [mV]**	cross-over talk [%]	fy y=13.747x [kN]	difference [kg]	linearity [%]
-6,5	-0,03	**-0,51**	6,1%	-6,9	**-46,1**	-6,5%
-5,5	-0,01	**-0,42**	1,9%	-5,8	**-25,9**	-4,4%
-4,5	-0,01	**-0,34**	1,7%	-4,7	**-20,1**	-4,2%
-3,7	-0,01	**-0,28**	1,8%	-3,8	**-13,6**	-3,5%
-2,7	0,00	**-0,20**	2,0%	-2,8	**-6,9**	-2,5%
-1,8	0,00	**-0,13**	2,3%	-1,8	**-1,2**	-0,7%
-0,8	0,00	**-0,06**	3,4%	-0,8	**3,6**	4,4%
-0,5	0,00	**-0,03**	3,0%	-0,5	**2,5**	5,4%
0,1	0,00	**0,01**	0,0%	0,1	**-2,0**	-
1,2	0,00	**0,08**	4,8%	1,2	**-0,9**	0,8%
3,3	0,01	**0,24**	3,4%	3,3	**-0,3**	0,1%
5,5	0,01	**0,40**	2,5%	5,4	**-2,8**	0,5%
7,6	0,01	**0,55**	2,2%	7,6	**-3,4**	0,4%
9,7	0,01	**0,70**	1,6%	9,7	**-6,2**	0,6%
11,6	0,01	**0,84**	1,6%	11,5	**-12,6**	1,1%
13,5	0,02	**0,97**	1,5%	13,4	**-13,4**	1,0%
15,3	0,02	**1,10**	1,6%	15,1	**-13,9**	0,9%

A.5 Scheme of signal transmission

Appendix B

B.1 Statistical properties of random vibrations

The basic subject in random vibration analysis is an acceleration signal sampled with *200 [Hz]* and filtered by Bessel Anti-Aliassing Filter with corner frequency *20 [Hz]*.

Table B.1: Statistical properties

Statistical property	Symbols	Units
• *mean value* $$m = \frac{x_1 + x_2 + \cdots x_n}{n}$$	$m;\ \overline{l(t)};\ \mu_x$	$\left[\frac{m}{s^2}\right]$
• *rms* (*root mean square*) $$x_{rms} = \sqrt{\frac{x_1{}^2 + x_2{}^2 + \cdots x_n{}^2}{n}}$$ it provides order of magnitude of the intensity of the random variable	$l_{rms};\ x_{rms}$	$\left[\frac{m}{s^2}\right]$
• *variance / autovariance* $$\sigma_{XX}{}^2 = (x - \mu_x)^2$$	$\sigma_{XX}{}^2;\ C;\ s_l{}^2$	$\left[\left(\frac{m}{s^2}\right)^2\right]$
• *covariance* $$\sigma_{XY} = (x - \mu_x) \cdot (y - \mu_y)$$	C_{lu}	$\left[\left(\frac{m}{s^2}\right)^2\right]$
• *standard deviation* $$s_l = \sqrt{s_l{}^2}$$ characterizes dispersion of the signal around it mean. For centred signal $(\overline{l} = 0)$ the standard deviation is equal to the rms value of the signal because $$x_{rms} = \mu_x + s_l$$	s_l	$\left[\left(\frac{m}{s^2}\right)\right]$

• *correlation / autocorrelation* the **a**uto**c**orrelation **f**unction (ACF) indicates the degree of random fluctuation of a signal. The units of correlation function are squared measured units. For centred signal ($\bar{l} = 0$) the peak at the origin is equal to the square of rms value or variance of the signal. $$R_l(0) = s^2 = {l_{rms}}^2$$	$R_l(\tau);\ R_{xx}(\tau)$	$\left[\left(\dfrac{m}{s^2}\right)^2\right]$
• *cross-correlation*	$R_{lu}(\tau);\ R_{xy}(\tau)$	$\left[\left(\dfrac{m}{s^2}\right)^2\right]$
• *correlation coefficient* $$\rho_l(\tau) = \frac{R(\tau)}{R(0)}\ \text{or}\ \rho_{lu} = \frac{C_{lu}}{s_l \cdot s_u}\ \text{or}\ \rho_{xy} = \frac{\sigma_{xy}}{\sigma_{xx} \cdot \sigma_{yy}}$$ for $-1 \le \rho_{lu} \le 1$ if l and u are linearly related e.g. $l = \pm a \cdot u + b$, the correlation coefficient is equal to -1 or $+1$. If the signals are fully independent equals zero. If the value of correlation coefficient is in range of $-1 \le \rho_{lu} \le 1$ it says nothing about relationship.	ρ_l	$[-]$

B.2 Random vibrations properties in frequency domain

The FFT operation gives so called *Fourier spectrum*. The amplitude of the FFT is related to the number of points in the time-domain signal. Therefore the magnitude of FFT(A) is divided by *N*. For *DC values* (A$_0$ – amplitude at frequency zero) the single sided spectrum G_{xx} equals to two – sided spectrum S_{xx}: $G_{xx} = {A_0}^2 = S_{xx}$.

Beyond DC values $G_{xx} = 2 \cdot S_{xx}$ so $G_{xx} = 2 \cdot S_{xx} = 2 \cdot {A_K}^2/4 = {A_K}^2/2$.

And ${A_K}^2/4 \equiv (A_K/\sqrt{2})^2$ and $A_K/\sqrt{2} = rms$. For this reason units for G_{xx} and S_{xx} are ${V_{rms}}^2$ or V^2.

The main reason why the *PSD* is often used in practice is the fact that input – output relationship for LTI systems becomes a product in the frequency domain.

The $PSD = \dfrac{Power\ Spectrum\ in\ {V_{rms}}^2}{\Delta f \cdot Noise\ Power\ Bandwidth\ of\ Window}$ $\left[\dfrac{\left(\frac{m}{s^2}\right)^2}{Hz}\right]$ or $\left[\dfrac{\left(\frac{m}{s^2}\right)_{rms}^2}{Hz}\right]$. The power spectrum density or amplitude spectrum density is normalized spectrum to the spectrum that

would be measured by *1[Hz]* wide square filter. The PSD strongly depends on sampling rate, record length and type of window.

The frequency resolution depends on sampling rate, length of record, averaging, overlapping. Massive influences have windows applied to the samples. They bring first and last instantaneous values to zero in order to make the sample periodic. Here such characteristic as main lob width, roll-off side lob and final frequency resolution determine about spectral leakage. The spectral leakage, sometimes also called picket-fence effect or spreading effect, distorts the measurement in such a way that energy from a given frequency component is spread over adjacent frequency beans. The scallop loss effect is known also amplitude error. Zero padding does not influence resolution and precise of spectral curve but make it smoother. The coefficients coherent gain *(CG)* and noise gain *(NG)* clear influence of windows. The noise gain is also called *Noise Power Bandwidth of Window*. It defines the increase of effective bandwidth of an FFT bin caused by spectral effect.

There data analysis software that offers calculations of various spectrums or choosing desirable units without mentioning about the physical or mathematical difference between them. Therefore in the **Table B.2** are listed several kinds of spectrum, corresponding formulas and units that they provide.

Table B.2: Different kind of spectrums

Spectrum	Unit
Two-sided amplitude spectrum $$S_{xx} = \frac{abs\big(FFT(A)\big)}{N}$$	$\left[\frac{m}{s^2}\right]$
Amplitude RMS single-sided amplitude *rms* spectrum $$G_{xx} = 2 \cdot \frac{S_{xx}}{\sqrt{2}} = \sqrt{2} \cdot S_{xx} = \sqrt{2} \cdot \frac{abs\big(FFT(A)\big)}{N}$$	$\left[\left(\frac{m}{s^2}\right)_{rms}\right]$

Amplitude square RMS single-sided power spectrum rms $$G_{xx} = 2 \cdot \frac{abs(FFT(A) \cdot FFT^*(A))}{N^2}$$	$$\left[\frac{m}{s^2}\right]$$
Amplitude square peak / single-sided power spectrum $$G_{xx} = 4 \cdot \frac{abs(FFT(A) \cdot FFT^*(A))}{N^2}$$	$$\left[\left(\frac{m}{s^2}\right)^2\right]$$
Amplitude RMS spectral density $$G_{xx} = \sqrt{2} \cdot \frac{abs(FFT(A))}{N \cdot \Delta f}$$	$$\left[\frac{\left(\frac{m}{s^2}\right)_{rms}}{Hz}\right]$$
Amplitude peak spectral density $$G_{xx} = 2 \cdot \frac{abs(FFT(A))}{N \cdot \Delta f}$$	$$\left[\frac{\left(\frac{m}{s^2}\right)}{Hz}\right]$$
Amplitude square RMS spectral density $$G_{xx} = 2 \cdot \frac{abs(FFT(A) \cdot FFT^*(A))}{N^2 \cdot \Delta f}$$	$$\left[\frac{\left(\frac{m}{s^2}\right)^2_{rms}}{Hz}\right]$$
Amplitude square peak spectral density $$G_{xx} = 4 \cdot \frac{abs(FFT(A) \cdot FFT^*(A))}{N^2 \cdot \Delta f}$$	$$\left[\frac{\left(\frac{m}{s^2}\right)^2}{Hz}\right]$$
Amplitude square peak spectral density, including reducing influence of window $$G_{xx} = 4 \cdot \frac{abs(FFT(A) \cdot FFT^*(A))}{N^2 \cdot \Delta f \, NoisePowerBandwidth}$$	$$\left[\frac{\left(\frac{m}{s^2}\right)^2}{Hz}\right]$$

Sampling is chosen according to the highest frequency of real signal or just the highest frequency of interest. This was set for $f_{max} = 25 \, [Hz]$. The **Nyquist law** says that $f_s \geq 2.6 \cdot f_{max}$ because the AA filter has leakage near to f_{ω_0}.

Window is applied because FFT needs the same value at the beginning and at the end of the sample. The window provides the value of zero *"0"*. Appling no window is the same as applying the rectangular or so called *"car box"* window.

Appendix C

C.1 Tests conducted with rear wheel

l_x [mm]	ε +/- [°]	M_T [Nm]	ground
1650	0	0	asphalt road
payload [kg]	**δ [°]**	**M_B [Nm]**	**tire**
2900	0	0	rear

v		R{vv}RandVibr{no.}		
5	test01	test02	test03	test04	test05
10	test06	test07	test08	test09	test10
15	test11	test12	test13	tes14	test15
20	test16	test17	test18	tes19	test20
25	test21	test22	test23	tes24	test25
	test26	test27	test28	test29	test30

v		R{vv}RandVibrBrake{no.}		
5	test31	test32	test33	test34	
10	test36	test37	test38	tes39	
15	test41	test42	test43	tes44	test45
20	test46	test47	test48	tes49	test50

v		R{vv}StepResp{no.}	
5	test91	test92	test93
10	test96	test97	test98
15	test101	test102	test103
20	test106	test107	test108

v		R{vv}BrakeStepSteer{no.}	
5	test131	test132	test133
10	test136	test137	test138
15	test141	test142	test143

C.2 Tests conducted with front wheel

l_x [mm]	ε +/- [°]	M_T [Nm]	ground
1650	0	0	asphalt road
payload [kg]	**δ [°]**	**M_B [Nm]**	**tire**
2710	0	0	front

v	F{vv}RandVibr{no.}				
5	test01	test02	test03		
10	test06	test07	test08		
15	test11	test12	test13	tes14	test15
20	test16	test17	test18	tes19	test20
25	test21	test22	test23	tes24	test25

v	F{vv}RandVibrBrake{no.}				
5	test31	test32	test33		
10	test36	test37	test38		
15	test41	test42	test43	tes44	test45
20	test46	test47	test48	tes49	test50

v	F{vv}StepResp{no.}		
5	test91	test92	test93
10	test96	test97	test98
15	test101	test102	test103
20	test106	test107	test108

v	F{vv}BrakeStepSteer{no.}		
5	test131	test132	test133
10	test136	test137	test138
15	test141	test142	test143